Carrier LO Phonon Interactions in InAs/GaAs Quantum Dots:Electronic Polarons and Excitonic Polarons

Vanessa Preisler

Carrier Phonon Interaction in InAs/GaAs Quantum Dots: Electronic Polarons and Excitonic Polarons

by

Vanessa Preisler

A Thesis Presented to

L'Université Pierre et Marie Curie (Paris VI)

In Partial Fulfillment of the Requirements

for the Degree of

Doctor of Philosophy

ÉCOLE NORMALE SUPÉRIEURE
DÉPARTEMENT DE PHYSIQUE
Paris, France

2006
(Defended July 10, 2006)

Abstract

This thesis presents a study of electrons, holes and excitons confined in self-assembled InAs/GaAs quantum dots. The interaction of these confined carriers with the longitudinal optical (LO) phonons of the surrounding crystal lattice is investigated. It is found that this interaction leads to the formation of the so-called quantum dot polarons; hybrid carrier phonon states which are the true excitations of a charged dot.

The first part of this thesis describes the results of far infrared (50 - 700 cm^{-1}) magnetospectroscopy experiments performed on n- and p-doped samples. The intraband energy levels of these systems are probed. The magnetic field is an important experimental parameter, as it allows for the evolution of the energy levels, necessary for the observation of electronic and hole polaron levels. Using the Fröhlich Hamiltonian, which couples the phonon and purely electronic states, the energy levels and oscillator strengths of the system are determined. For both the investigation of electrons and holes confined in dots, a good agreement is found between the calculations and the experimental results.

The second part of this thesis is dedicated to the study of the interaction between electron-hole pairs or excitons and the phonons of the lattice. The interband energy transitions of the dots are investigated using photoluminescence excitation and resonant photoluminescence spectroscopy under strong magnetic fields up to 28 T. These techniques allow for the circumvention of the inhomogeneous broadening of the resonances that arise from size and composition fluctuations in the quantum dot ensembles. The magnetic field dependence of the resonance energies allows for an unambiguous assignment of the interband transitions. The excitonic polaron energies as well as the oscillator strengths of the interband transitions are determined. The calculations account well for the experimental data.

Acknowledgements

No matter how hard I tried, it was impossible to be a stressed out Ph.D. student with a thesis advisor like Yves Guldner. Any problem, fear or doubt I could come up with, Yves was always there to reassure me and find a solution. Along with making sure that every aspect of my graduate school experience in France went smoothly, he, being the ultimate source on semiconductor physics, has been a wonderful teacher for me throughout these past three years.

Most Ph.D. students count themselves lucky if they have one capable theorist with whom they can work. With Robson Ferreira and Gerald Bastard across the hall from me during these past three years, I had two gifted theorist at my disposal. It really wasn't fair. I would especially like to thank Robson Ferreira who challenged me and forced me to reflect upon my work. I realize now how lucky I have been to have worked with him and I thank him for all his patience and kindness.

Strong, intelligent and extremely capable, Sophie Hameau was a role model for me throughout my thesis, and for that matter is a role model for all aspiring women physicists. Being equally comfortable in a lab as she is in front of a physics classroom, Sophie was the perfect mentor for a first year physics graduate student. Working with her in the lab was an enjoyable and educational experience. She contributed enormously to the experimental part of this thesis, and I thank her for this and for her friendship.

Although at times a humbling experience, working with Thomas Grange was a real pleasure. As a first year Ph.D. student, his comprehension of the subtleties of the physics of quantum dots along with his problem solving abilities truly amazed me. A large part of the theory presented in this thesis was realized thanks to his hard work and intelligence.

I would like to thank Louis-Anne de Vaulchier, in particular, for helping me in my daily battles against my computer. I would like to thank Aristide Lemaître, who provided all the high quality samples used in this thesis. I thank all the technical staff at ENS for their help with the experimental aspect of my thesis and I thank Anne Matignon for facilitating all administrative aspects of my thesis.

I would equally like to thank Francis Teran, Marek Potemski, Marcin Sadowski and Adam Babinski for being nothing but helpful and welcoming during my stays at the High Magnetic Field Laboratory in Grenoble. I would in particular like to thank Francis Teran. The quality and quantity of PL data presented in this thesis is a testament to the great experimental physicist he is.

I would like thank my family back in California, who didn't let an ocean of separation stop them from being an enormous support and my husbands family in Grenoble for helping make France a second home for me.

Finally I would like to thank my husband, who, after three years of listening to me babble on about my thesis, is now capable of explaining the physics of holes in quantum dot semiconductor systems. His support and humor was indispensable for me throughout my graduate studies and I thank him for this.

Table of Contents

List of Figures

List of Tables

Introduction

This thesis is a report on the carrier phonon interaction in semiconductor quantum dots. A quantum dot is a nanoscale object that, similar to an atom, presents the unique ability to confine electrons in the three dimensions of space. For this reason, quantum dots are commonly known as "artificial atoms." Such systems are interesting as much for the study of their fundamental physical properties as for their possible device applications. Many applications of quantum dots have been predicted, such as single quantum dot transistors or quantum dot lasers [1, 2, 3, 4]. Keeping in mind these possible applications, the work presented in this thesis attempts to investigate and explain some of the fundamental physical properties of these nanostructures. In particular, the coupling between a carrier confined in a dot and the vibrations of the semiconductor lattice in which the quantum dot resides, is studied. Understanding this interaction mechanism is essential for the general understanding of the electronic properties of quantum dot systems. In essence, it is found that electronic and lattice excitations strongly mix to form the so-called polaron states of quantum dots. From the theoretical point of view, the quantum dot polaron state reflects a complex entanglement of electronic and phonon states. This study evidences the existence of polaron states in quantum dots, whether the confined carrier be an electron, hole or exciton.

Chapter 1

The first chapter will be dedicated to both the calculation of the discrete energy levels of a quantum dot structure, as well as to the experimental means of investigating these levels.

The InAs/GaAs quantum dot samples studied in this thesis were grown using the Stranski-Krastanov mode, which, in particular, exploits the lattice mismatch of the two materials to create nanoscale islands. The confining potential in a quantum dot structure, that induces the quantization of the carrier energy levels, depends on the size, shape, and composition of these islands. In addition, for dots grown using this mode, the strain, created as a result of the lattice mismatch between InAs and GaAs, also has a large influence on the confining potential. The calculation of the discrete energy levels of a quantum dot therefore depends on these, for the most part unknown and difficult to control, growth parameters. However, the essential ingredient of the dot potential is its ability to confine carriers in the three directions of space. The remaining parameters (strain, inhomogeneous InAs/GaAs content, piezoelectric effects) are secondary [5]. For this reason, a simple model, that takes the confining potential and effective mass of the carrier as adjustable parameters,

has been used to calculate the energy levels of a quantum dot system. The values of the parameters are chosen to obtain results in good agreement with the experimental results. The energy levels calculated in the first chapter will be of use throughout the thesis.

The intraband energy transitions of a carrier confined in a quantum dot can range from 20 meV for holes to 60 meV for electrons. Far infrared magnetospectroscopy is therefore employed to probe these energy levels. The magnetic field is an important experimental parameter, as it allows for the evolution of the energy levels, necessary for the observation of electronic and hole polaron levels.

The interband ground state energies of the quantum dot samples studied in this thesis are found in the mid infrared energy range. Magnetophotoluminescence experiments are therefore conducted to investigate the interband energy transitions and in turn the excitonic polaron energy levels.

Chapter 2

In Chapter 2, the polaron states of quantum dots systems will be calculated and their existence experimentally evidenced in n-doped samples.

In bulk, quantum well and quantum wire structures, the interaction between a charged carrier and longitudinal optical phonons allows for the rapid relaxation of an excited carrier to its ground state. In these cases, the relaxation process is well described by Fermi's Golden rule. Longitudinal optical phonons play a very different role in quantum dot systems which, unlike the structures alluded to above, possess discrete electronic energy levels. Fermi's Golden rule no longer applicable, it is found that the carrier and phonons in quantum dot structures are strongly coupled to one another. This coupling leads to the formation of polaron states, the true excitations of a charged dot. The calculation of these polaron states, presented in Chapter 2, will be used throughout the thesis as it can be applied to dots containing electrons, holes or excitons.

In order to verify the above polaron model, magnetotransmission results for n-doped samples reported in the thesis of J.N. Isaia [6] and S. Hameau [7] will be presented. In addition, new experimental results in magnet field using polarized light will be presented as complementary support of the polaron model, as applied to n-doped dots.

Chapter 3

Chapter 3 will be dedicated to the investigation of p-doped samples and the hole polaron state.

To date, there have been few investigations of the valence band magneto-optical transitions in quantum dots and therefore no direct evidence for the formation of hole magnetopolarons. The hole excitations of p-doped samples in polarization and in intense magnetic fields will be investigated here. The results will be interpreted using the polaron model for the case of a positively charged hole.

The differences between hole polaron states and their electron counterparts will be highlighted. In particular, as the intraband transitions energies of holes ($\sim$ 20 meV) are found below that of electrons ($\sim$ 60 meV), holes are found to primarily

interact with an InAs-like phonon mode, as compared to the GaAs-like phonon found in interaction with electrons.

Chapter 4

The understanding of the behavior of an electron-hole pair (exciton) confined in a quantum dot, is of utmost importance if these systems are to be used for application purposes (lasers, unique photon sources, ...). Chapter 4 investigates such systems using the technique of photoluminescence excitation under strong magnetic fields.

Effects, such as the Coulomb interaction felt between the two carriers, differentiate the situation of an exciton trapped in a quantum dot from the case of a single charged particle. In addition, as the coupling between a carrier and optical phonons is basically electrical (Fröhlich interaction), one could expect a rather small coupling between phonons and the neutral exciton. The calculation presented in Chapter 4, will reveal that, in spite of their electrical neutrality, exciton and phonons are in a strong coupling regime and the formation of excitonic polaron states is indeed predicted. The simulated magnetoabsorption spectra will be compared to the experimentally obtained magnetophotoluminescence excitation spectra.

Chapter 5

The self-assembled InAs/GaAs samples investigated in this thesis contain not one unique quantum dot, but a large population of dots (dot density per layer $\sim 10^{10}\text{cm}^{-2}$). In Chapter 5, the consequences that arise from the size inhomogeneity among dots of a single sample will be demonstrated through the study of resonant photoluminescence experiments in intense magnetic fields.

The photoluminescence peak of a quantum well structure can be homogeneously broadened due to, e.g., thermal spreading and slight non-uniformity of the interfaces. In self-assembled quantum dot samples, a large number of dots with different sizes, shapes and compositions and therefore electronic levels, are present. The inhomogeneous broadening observed in the photoluminescence spectra of such samples is in part a consequence of the distribution of different dots in a single sample. The effect of this distribution on the behavior of resonant photoluminescence spectra will be studied.

Finally, these same results will be compared to the excitonic polaron energy level and oscillator strength calculations of Chapter 4.

Bibliography

[1] L. Guo, E. Leobandung and S.Y. Chou, *A Silicon Single-Electron Transistor Memory Operating at Room Temperature*, Science **275**, 649 (1997).

[2] N. Kirstaedter, N.N. Ledentsov, M. Grundmann, D. Bimberg, V.M. Ustinov, S.S. Ruvimov, M.V. Maximov, P.S. Kop'ev, Zh.I. Alferov, U. Richter, P. Werner, U. Gösele, and J. Heydenreich, *Low threshold, large T_o injection laser emission from (InGa)As quantum dots*, Electronics Lett. **30**, 1416 (1994).

[3] D. Bimberg, M. Grundmann, and N.D. Ledenstsov, *Quantum Dot Heterostructures*, Wiley (1999).

[4] D. DiVencenzo, *The Physical Implemtation of Quantum Computation*, Fortschr. Phys. **48**, 771 (2000).

[5] A. Vasanelli, Ph.D. thesis, *Transitions optiques interbandes et intrabandes dans les boîtes quantiques simples et couplées verticalement*, Université Paris VI (2002).

[6] J.N. Isaia, Ph.D. thesis, *Niveaux électronique et interaction électron-phonons dans les boîtes quantiques d'InAs/GaAs*, Université Paris VI (2002).

[7] S. Hameau, Ph.D. thesis, *Systèmes d'électrons dans les nanostructures semiconductrices à confinement quantique dans 2 ou 3 directions*, Université Paris VI (2000).

Chapter 1

Presentation of Quantum Dots

In this chapter, a general presentation of quantum dots (QDs) and how they are investigated is given. First, a brief history of these systems along with the motivation behind their study is presented. Then a description of the fabrication of the QD samples used in this thesis is given. Finally, a description of how the energy levels of these systems are calculated is presented followed by the means of investigating these energy levels experimentally.

1.1 History and Motivation

As early as the 1950s, the idea of using ultra-thin layers of certain materials for the study of size quantification existed. This presumption became a working reality a few decades later with the development of new growth methods such as molecular beam epitaxy. In the early 1970s, the first low dimensional heterostructures, known as quantum wells (QWs), were developed. A heterostructure consists of a layered stack of semiconductors with different energy band gaps. The movement of electrons in one of these layers is restricted to only two dimensions. Such structures, that form the basis of most of the optoelectronic devices available today, were rather well understood by the end of the 1980s. This led physicists to investigate the possibility of further reducing the dimensionality to create 1D (quantum wire) and 0D (quantum dot) structures. Figure 1.1 shows schematically the evolution of the energy of an electron and the density of states as the dimensionality of the system is reduced. For QDs, the energy spectrum of an electron is discrete like in atomic physics, hence the adoption of the term "artificial atom." The study of these artificial atoms has proven useful to explore a wide range of physical phenomena. Moreover, these nanostructures have a great potential for technological applications. Many applications in optoelectronics have been predicted, such as lasers, FIR detectors and quantum computing [1, 2, 3].

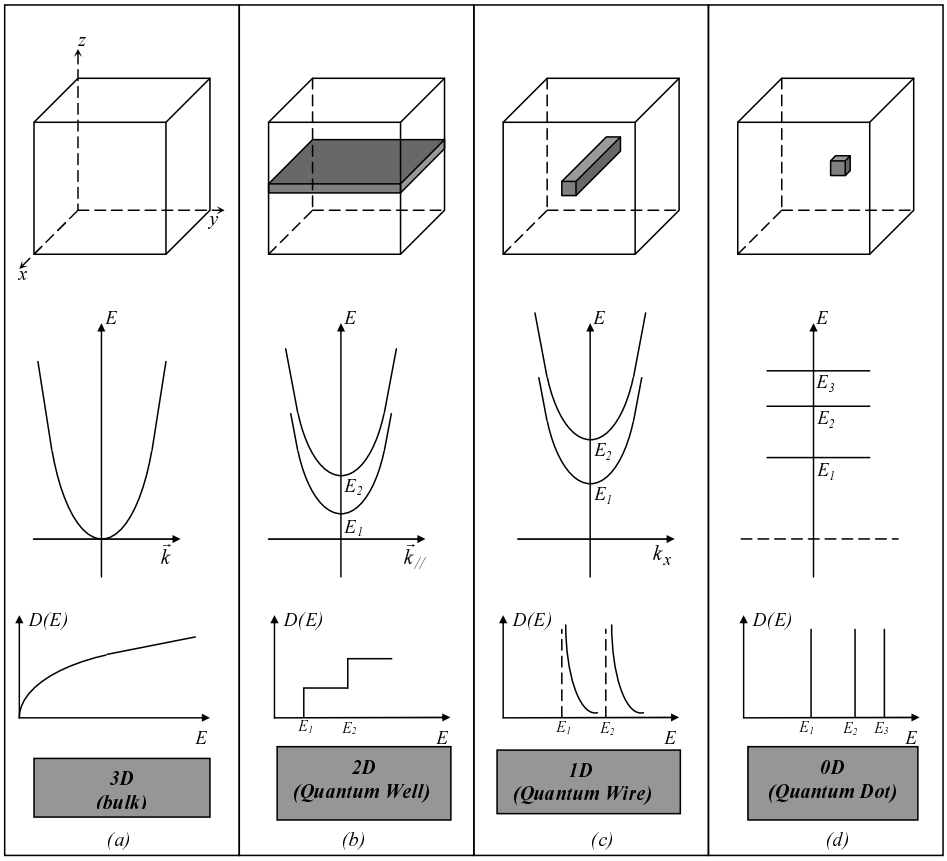

Figure 1.1: Evolution of the energy E of an electron and of the density of states as the dimensionality of the structure is reduced from 3D (bulk) (a) to 0D (quantum dot) (d).

1.2 Fabrication

One popular and practical method to grow QDs is the Stranski-Krastanov (SK) growth mode. This growth process, which consists in utilizing the lattice mismatch between two semiconductor materials to create nanometer-scale islands that can trap carriers, was first proposed by I.N. Stranski and L. Krastanov in 1937. All the samples used in this work (InAs QDs in GaAs) were grown using the SK method. Using molecular beam epitaxy (MBE), InAs is deposited on a GaAs substrate. The lattice mismatch between the two materials (7%*) introduces strain. The first few layers of InAs form a 2D layer which is called the wetting layer (WL) [Fig. 1.2(a)]. After a critical thickness is reached, there is a relaxation of the strain and 3D growth becomes energetically favorable. Subsequently, small islands of InAs are spontaneously formed on the WL [Fig. 1.2(b)] [4]. This transition from 2D to 3D growth, called the SK Transition, occurs in InAs/GaAs systems for a critical thickness of 1.7 to 1.8 monolayers [5]. The islands that form as a result of this transition are called self-organized or self-assembled quantum dots. The island structures are then covered with a GaAs epitaxial layer [Fig. 1.2(c)]. A 3D array of QDs can then be created by repeating the growth process described above. If the distance between successive InAs layers is less than 20-30 nm (depending on the dot size) , the QDs in successive layers tend to be aligned in order to minimize the elastic strain energy of the InAs layers. For thicker GaAs spacer layers, no vertical coupling is observed [6]. The size and density of the islands strongly depend on the growth parameters: temperature during growth, growth rate, thickness of the epitaxy layers [7, 8]. The typical dimensions of QD islands range from 12 to 25 nm laterally and from 2 to 5 nm in height. An InAs island therefore is made up of about 10^4 atoms. The size dispersion of the dots in a given sample can range from 10 to 15%. The average density of dots per layer can range between 10^8 and 10^{11} cm^{-2} [9]. Images taken using AFM (atomic force microscopy) help one to visualize the form and organization of the islands in a layer, as shown in Fig. 1.3.

*a(InAs) = 6.0583 Å, a(GaAs) = 5.6532 Å for T = 300 K

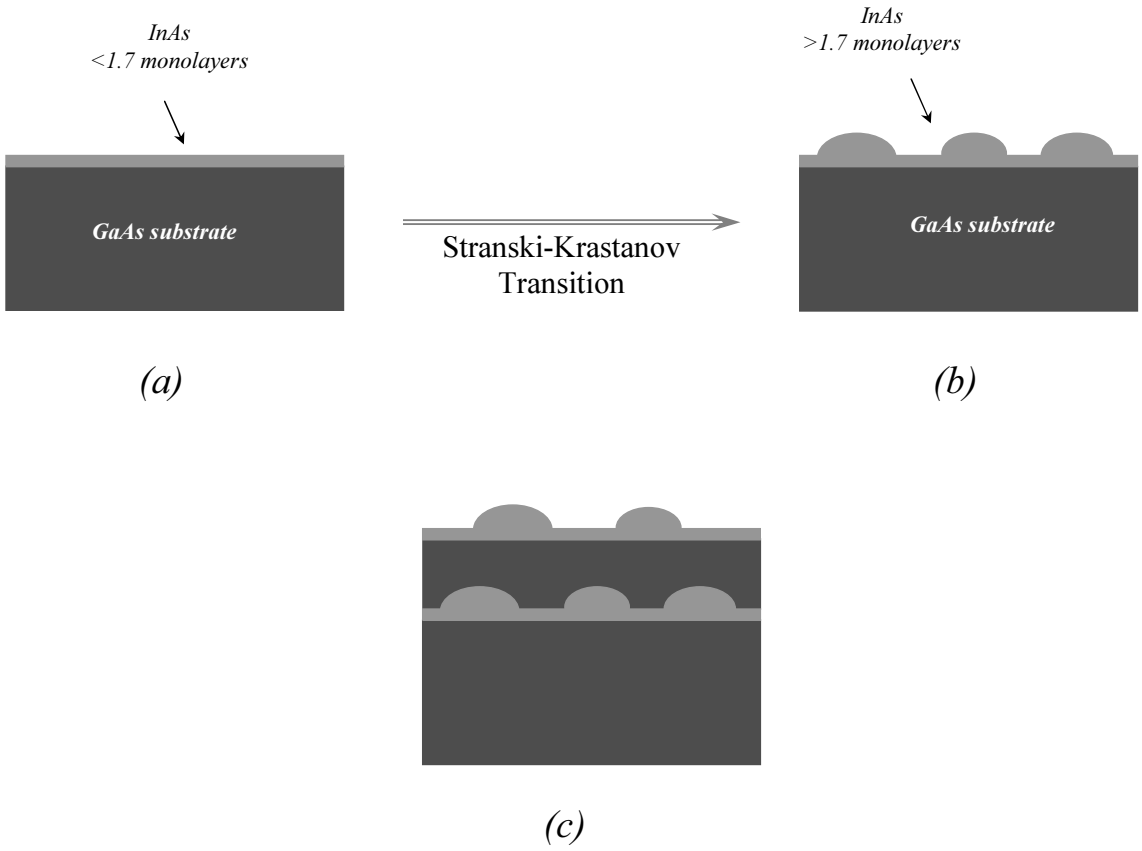

Figure 1.2: Different stages of the SK growth process of InAs dots on a GaAs substrate.

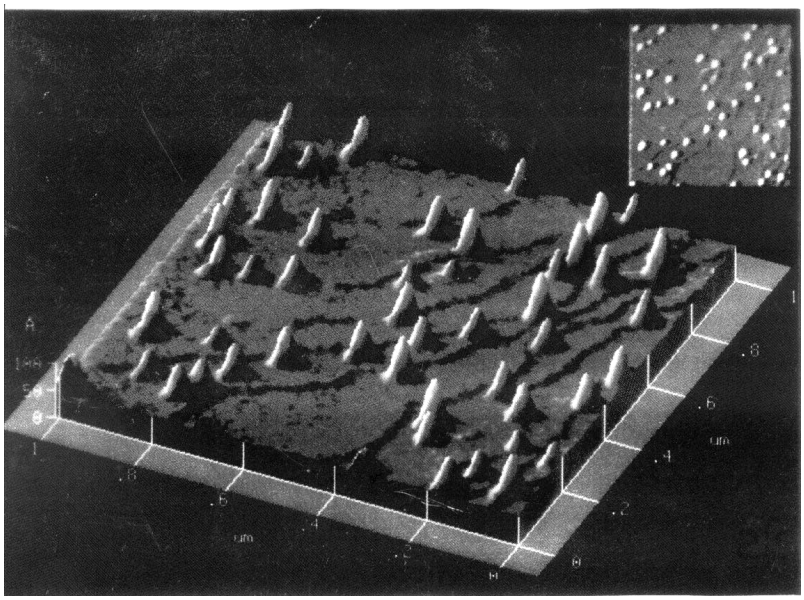

Figure 1.3: AFM image of a layer of InAs/GaAs self-assembled quantum dots (J.M. Moison CNET-Bagneux).

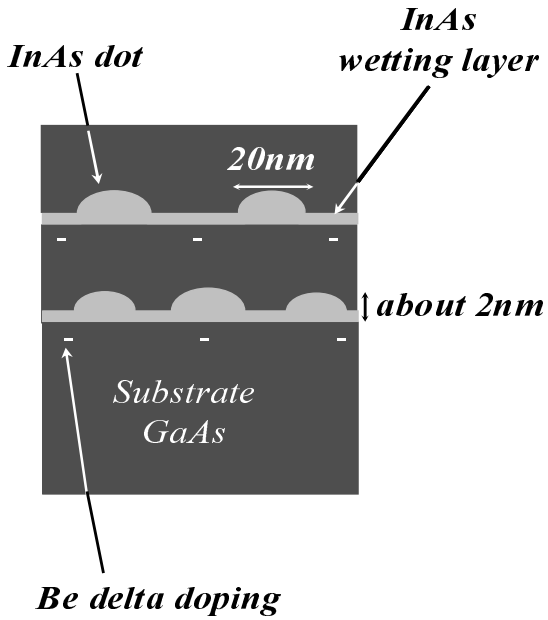

Figure 1.4: Representation of the placement of Be layers 2 nm under each dot layer (δ-doping).

1.3 Characteristics of Samples

The samples investigated in this thesis were made at the Laboratoire de Photonique et Nanostructures by Aristide Lemaître. Samples containing a multistack of 20 layers of InAs QDs were prepared using MBE. The presence of a multistack of layers, as a opposed to a single layer, is necessary when conducting far infrared (FIR) absorption measurements as a resonant absorption associated with a single dot layer is weak (a few 0.1%) [10]. It is therefore important to point out that we present a study of QD ensembles and not single dots. This has for consequence, for example, the broadening of a PL peak due to size dispersion of the dots in a sample.[†] However, as each dot layer is separated by a 50-nm-thick GaAs barrier and has a density of dots per layer of $\sim 4 \times 10^{10}$ cm^{-2} (interdot distance of $\sim$ 50 nm), no coupling between dots is expected and the QDs can be considered as isolated [6]. Cross sectional transmission electron spectroscopy in samples grown in similar conditions have shown that the QDs resemble flat truncated cones with an $\sim$ 20 nm basis diameter and an $\sim$ 3 nm height [11]. This thesis presents experiments performed on n-doped, p-doped and undoped samples. For the n-doped (p-doped) samples the dot filling was realized by a Si (Be) δ-doping of each GaAs barrier at 2 nm under each dot layer (see Fig. 1.4). The doping concentration was adjusted to transfer on average one to two carriers per dot. The characteristics of each sample used in this work is presented in Table 1.1.

[†]see section 4.1.1

Sample Name	δ-doping	Doping concentration (cm^{-2})
N1	Si	$6 \cdot 10^{10}$
P1	Be	$5 \cdot 10^{10}$
P2	Be	$10 \cdot 10^{10}$
U1	undoped	-
N2	Si	$4 \cdot 10^{10}$
P3	Be	$4 \cdot 10^{10}$

Table 1.1: Names and doping concentrations of samples presented in thesis. Samples P1 and P2 were grown during the same MBE run. Samples U1, N2 and P3 were grown during the same MBE run.

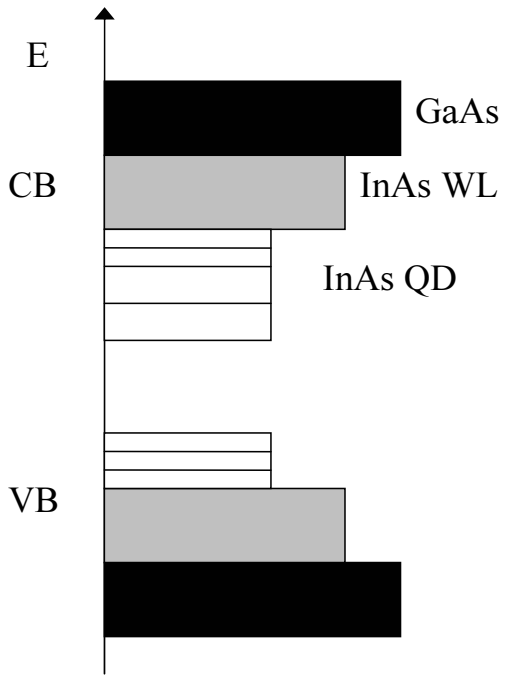

Figure 1.5: Schematic of conduction band (CB) and valence band (VB) states of an InAs/GaAs system: 3D continuum states of the GaAs substrate in black, 2D continuum states of the InAs WL in grey and the discrete energy levels of the InAs QD in solid lines.

1.4 Electronic States

1.4.1 Electronic Structure of an InAs/GaAs System

A sample of InAs/GaAs self-assembled QDs possesses three different kinds of electronic states: the 3D continuum states of the thick GaAs layers, the 2D continuum states of the InAs WL, and finally the 0D discrete states of the InAs QD. Figure 1.5 represents schematically the density of states of the conduction and valence bands of an InAs/GaAs structure.

In order to calculate the energy levels in QDs, one needs to consider the size, shape and composition of the dot, as well as the strain effects. This is a difficult task since all these parameters can not be controlled during the growth process and most of the time are not known with great precision. Different methods have been proposed to model QDs: the 8-band $k \cdot p$ method [12], the empirical pseudo-potential method [13], the tight binding method [14], the effective mass method [15]. We have chosen a one band (parabolic) effective mass method to calculate the QD energy levels. The results found using this method are consistent with those obtained using the more complex methods mentioned above [16]. Such a model also gives an accurate description of the coupling between electrons and phonon modes in n-doped samples [17, 18].

However, a large focus of this thesis also concerns valence states and the use of such

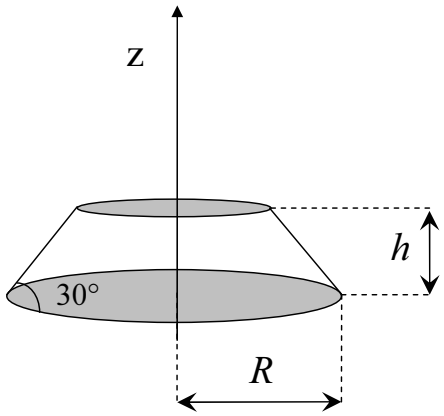

Figure 1.6: Truncated cone of height h and radius R used to model the QD. The z-axis is the growth direction of the sample.

a simple model is less evident for the valence levels of semiconductor nanostructures, as discussed in many works (see e.g. Ref. [12] and [19] and references there in). For instance, non-parabolicity and mass anisotropy should play an important role in the description of the hole states. In order to account for these effects in a simplified and efficient way, we consider an anisotropic dispersion for heavy holes, with an in-plane mass chosen to best fit the experimental results. The light hole is left out of our calculations as its confinement energy is close to the top of the GaAs valence band [15, 16].‡ This model suffices to provide a good description of our experimental results using reasonable fitting parameters [20].

1.4.2 Calculation of Energy Levels

Here we will summarize the calculation developed in the thesis of O. Verzelen [21]. In order to calculate the energy levels of a carrier (hole or electron) in a QD, the shape of the dot is modeled by a truncated cone of height h and with a circular basis of radius R and basis angle of 30°, as shown in Fig. 1.6. Using the envelope function approximation, the wave function of a carrier in such a dot can be described by the product of a Bloch function and a function that varies slowly (called the envelope function) over a distance on the scale of an elementary unit cell of the lattice. The Hamiltonian for the envelope function is written:

$$\mathbf{H} = \mathbf{E}_z + \mathbf{E}_{\rho,\theta} + \mathbf{V}(\rho, z), \tag{1.1}$$

where $\mathbf{E}_z$ and $\mathbf{E}_{\rho,\theta}$ are the z-direction (growth direction) and in-plane kinetic energies respectively and $\mathbf{V}(\rho, z)$ corresponds to the confinement potential that is equal to 0 outside the dot and $-V_0$ inside the dot. V_0^e (V_0^h) is defined as the conduction (valence) band offset between InAs and GaAs. The band gap of strained (due to the

‡See Appendix A

surrounding GaAs) InAs is ~ 0.53 eV at $T = 4$ K as compared to 0.41 eV for bulk InAs at the same temperature [22]. For pure InAs islands, taking into account that the energy band gap of GaAs at 4 K is 1.52 eV, $V_0^e = 572$ meV for an electron and $V_0^h = 418$ meV for a hole [23]. During the growth process, GaAs interfuses into the QDs so that the islands are not pure InAs, but contain a certain percentage ($\sim 30 - 50\%$) of GaAs [24]. The conduction and valence band offsets depend on this percentage, which in turn depends on the growth parameters. As the growth parameters can change from sample to sample, we choose the interdiffusion percentage (and therefore offsets) to best fit the data of a sample.

Given that the confinement potential has a cylindrical symmetry, the eigenstates of the QD system are also eigenstates of $\mathbf{L}_z$, the projection of the angular momentum in the z-direction. Using the same nomenclature as in atomic physics the QD states can be denoted as follows:

$$\begin{array}{lcl} L_z = 0 & \leftrightarrow & |s\rangle, \text{ ground state} \\ L_z = \pm 1 & \leftrightarrow & |p\rangle, \text{ first excited state} \\ L_z = \pm 2 & \leftrightarrow & |d\rangle, \text{ second excited state} \\ \ldots\ldots\ldots & \leftrightarrow & \ldots\ldots\ldots\ldots\ldots\ldots \end{array}$$

The ground state possesses an s-like symmetry and therefore has a wavefunction that is independent of θ. The first excited state is p-like and has a 2-fold degeneracy.[§] The number of excited states in the dot depends on its size.

To calculate the s and p states of the system, a variational method has been employed [21]. Gaussian functions that respect the symmetry of the s and p states are taken as trial wavefunctions:

$$\psi_s(\vec{\mathbf{r}}) = \psi_s(\rho, \theta, z) = \frac{1}{\sqrt{\sigma_s \beta_s^2 \pi^{3/2}}} \exp\left(-\frac{\rho^2}{2\beta_s^2} - \frac{(z - z_{0s})^2}{2\sigma_s^2}\right) \tag{1.2}$$

$$\psi_{p_\pm}(\vec{\mathbf{r}}) = \psi_p(\rho, \theta, z) = \frac{\rho}{\sqrt{\sigma_p \beta_p^4 \pi^{3/2}}} \exp\left(-\frac{\rho^2}{2\beta_p^2} - \frac{(z - z_{0p})^2}{2\sigma_p^2} \pm i\theta\right) \tag{1.3}$$

For each wavefunction we have three adjustable parameters: β the in-plane width of the wavefunction, σ the z-direction width, and z_0 the center of the gaussian along the z-axis. By minimizing the energy associated with these functions, the energy eigenvalues of the s and p states can be found. In Fig. 1.7, these energies are presented as a function of the height h of the QD and its radius R. An in-plane electron (heavy hole) mass of $m_e = 0.07 m_o$ ($m_h = 0.22 m_o$) was used in this calculation as well as a conduction (valence) band offset of $V_0^e = 290$ meV ($V_0^h = 212$ meV) which corresponds to an average homogeneous gallium content of $\sim 50\%$.

We find that the height has more of an influence on the confinement of the carrier in the dot, whereas the radius more affects the intraband energy differences ($E_p - E_s$). For a dot size typical of our samples, i.e. $R = 115$ Å, $h = 28$ Å, an $s - p$ intraband energy difference of 47 meV for electrons and 19 meV for holes is found.

[§]See Appendix A

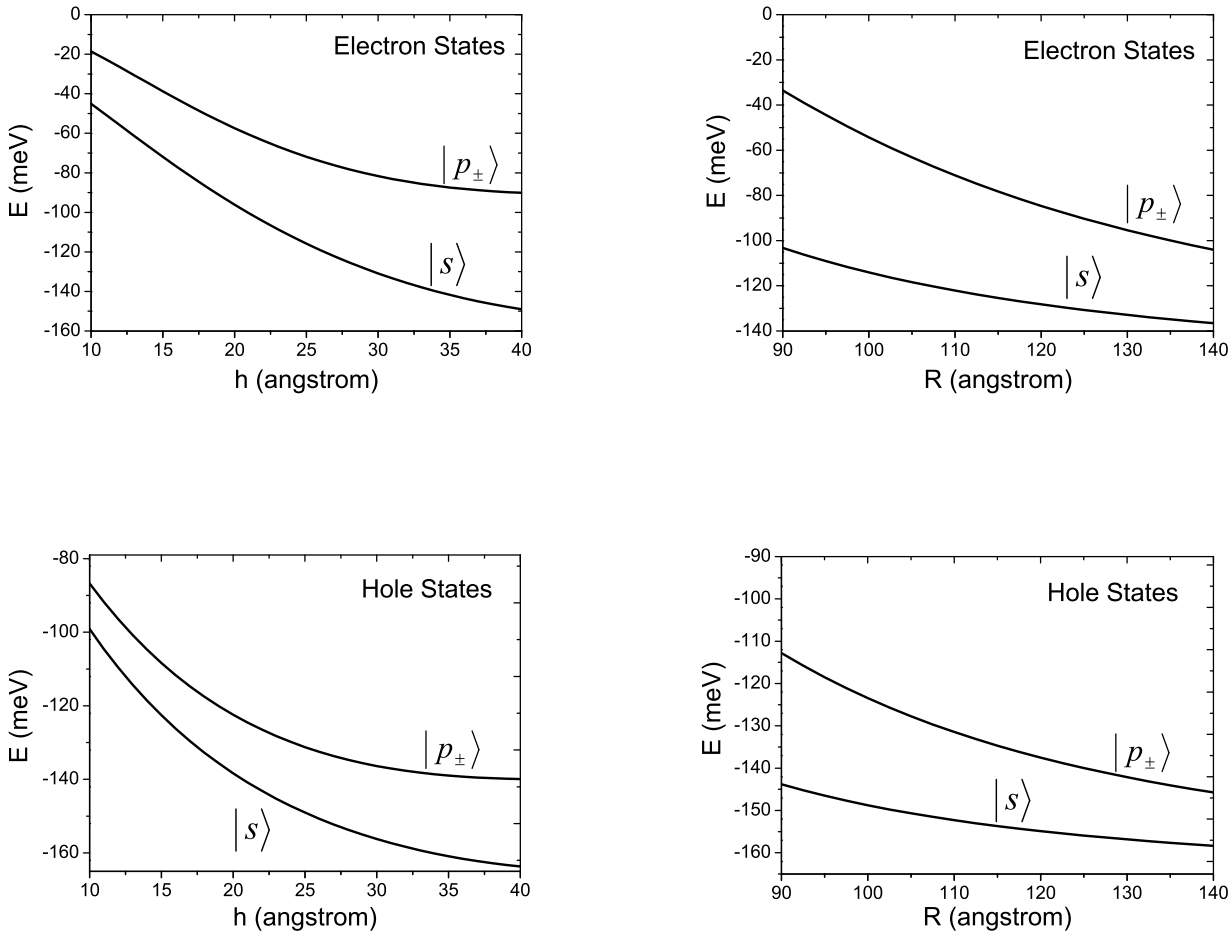

Figure 1.7: The energies of the s and p states for an electron (top) and a hole (bottom) confined in a quantum dot as a function of the height h of the dot (left, with a fixed radius $R = 115$ Å) and as a function of the radius R (right, with a fixed height $h = 28$ Å). The zero energy is taken at the bottom of the GaAs conduction for the electrons and the top of the GaAs valence band for the holes.

Anisotropy of Dots

In the above model, a 2-fold degeneracy is found in the p states. Experimentally, we find that this degeneracy is lifted. This is due to the fact that self-assembled quantum dots display a slight in-plane anisotropy, along the [110] and [1$\bar{1}$0] directions of the sample. Different effects have been considered in literature to explain this anisotropy. In the pseudopotential model this anisotropy arises from the C_{2v} atomistic symmetry of zinc blende crystals which distinguishes between these two directions [19]. In the framework of the one-band envelope function formalism the anisotropy has been attributed to the phenomenological shape anisotropy of the dots [10, 25]. In any case, the main effect of the anisotropy is to split the two degenerate $l_z = \pm 1$ levels of the QDs. The splitting of the two levels at $B = 0$ T is clearly observed in the FIR absorption spectra of doped dots, as seen in Figure 1.8. The absorptions correspond to the intraband transitions between the s and p states. The spectra for light linearly polarized along the [110] and [1$\bar{1}$0] directions of sample N1 [Fig. 1.8(a)] and P1 sample [Fig. 1.8(b)] are presented. The anisotropy related energy splitting is found to be $\sim$ 10 meV for the n-doped sample and $\sim$ 1 meV for the p-doped. To account for this splitting in our cylindrical basis, we have treated the in-plane anisotropy in perturbation by introducing a coupling term, $\mathbf{V}_a$, whose matrix element, between the p_+ and p_- states, is equal to half of the observed splitting:

$$\begin{aligned} 2\langle p_e^+|\mathbf{V}_a^e|p_e^-\rangle &= 2\delta_a^e = 10 \text{ meV} \\ 2\langle p_h^+|\mathbf{V}_a^h|p_h^-\rangle &= 2\delta_a^h = 1 \text{ meV} \end{aligned} \tag{1.4}$$

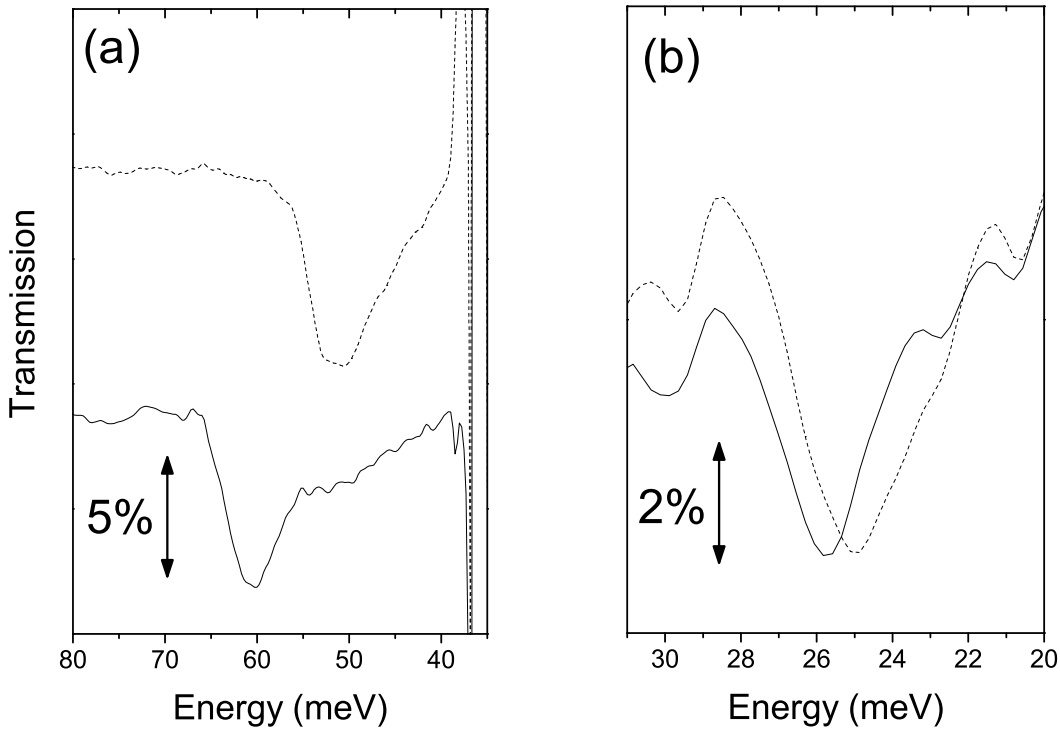

Figure 1.8: FIR transmission spectra at B = 0 T for radiation linearly polarized along the [110] (solid curve) and the [1$\bar{1}$0] (dashed curve) directions for sample N1 (a) and sample P1 (b). The observed absorptions correspond to the *s*-*p* intraband transitions. The curves in (a) have been vertically offset for clarity.

1.5 Investigation of Energy Levels

In order to investigate the energy levels of a carrier in a QD, the system needs to be excited. As shown in the preceding section, the intraband energy differences of holes (electrons) are $\sim$ 20 meV (50 meV), which are found in the the far infrared energy range. A magnetic field is applied in order to further the investigation, as it can be used to tune the energy separation between different states in the dots. FIR magnetospectroscopy experiments have been performed to investigate the intraband energy transitions of the systems. In addition, magneto-photoluminescence experiments were conducted in order to study the interband transitions of the dots. In this section, a detailed description of these two experimental methods is given, followed by a discussion of the coupling between a charged carrier with light and a magnetic field.

1.5.1 FIR Magnetospectroscopy: Intraband Transitions

A schematic for the setup of a FIR magnetospectroscopy experiment is shown in Fig. 1.9. The light source is a mercury vapor lamp. The FIR light is directed through a Michelson interferometer, which consists of a mylar beamsplitter and two mirrors. The light first hits the beamsplitter where half the beam is reflected to a stationary mirror and the other half passes through to a moving mirror. When the two halves of the beam recombine again on the beamsplitter they exhibit a path length difference x due to the mobile mirror. The recombined beam leaves the interferometer and is directed into the cryostat through the sample and is finally focused on the detector. The detector measures the intensity $I_{tr}(x)$ of the combined FIR beams as a function of the moving mirror displacement x, the so-called interferogram. Finally, the computer calculates the Fourier transform of the interferogram to obtain a transmittance spectrum, $I_{tr}(\sigma)$, where σ is the wavenumber [26].

A particular beamsplitter can have a thickness ranging from 3.5 to 12 μm. The 3.5 and 6 μm beamsplitters are both good candidates to use for investigating the intraband transitions for p- or n-doped samples, as they both possess good intensity spectrum in the range of 100-700 cm^{-1} ($\sim$10-90 meV).

The experimental setup at ENS in Paris uses a superconducting magnet, found inside the cryostat, which can produce magnetic fields up to 17 T. For the FIR experiments conducted at the High Magnetic Field Laboratory in Grenoble, in collaboration with Marcin Sadowski and Marek Potemski, a resistive magnet, which can reach 28 T, is used.

The applied magnetic field, as well as the propagation direction of the light are parallel to the growth axis of the sample. The sample is placed in a cryostat in a liquid helium bath that is pumped to a temperature of 2 K. Finally, the detector is a Si-composite bolometer that works at liquid helium temperatures.

It is possible, in the experimental set-up in Paris, for a linear polarizer to be placed directly underneath the sample in the cryostat. The linear polarizer can be rotated to polarize the EM field in a certain direction in the plane perpendicular to the growth direction. In this way, we are able to measure the transmission spectra of different polarizations of light with an applied magnetic field.

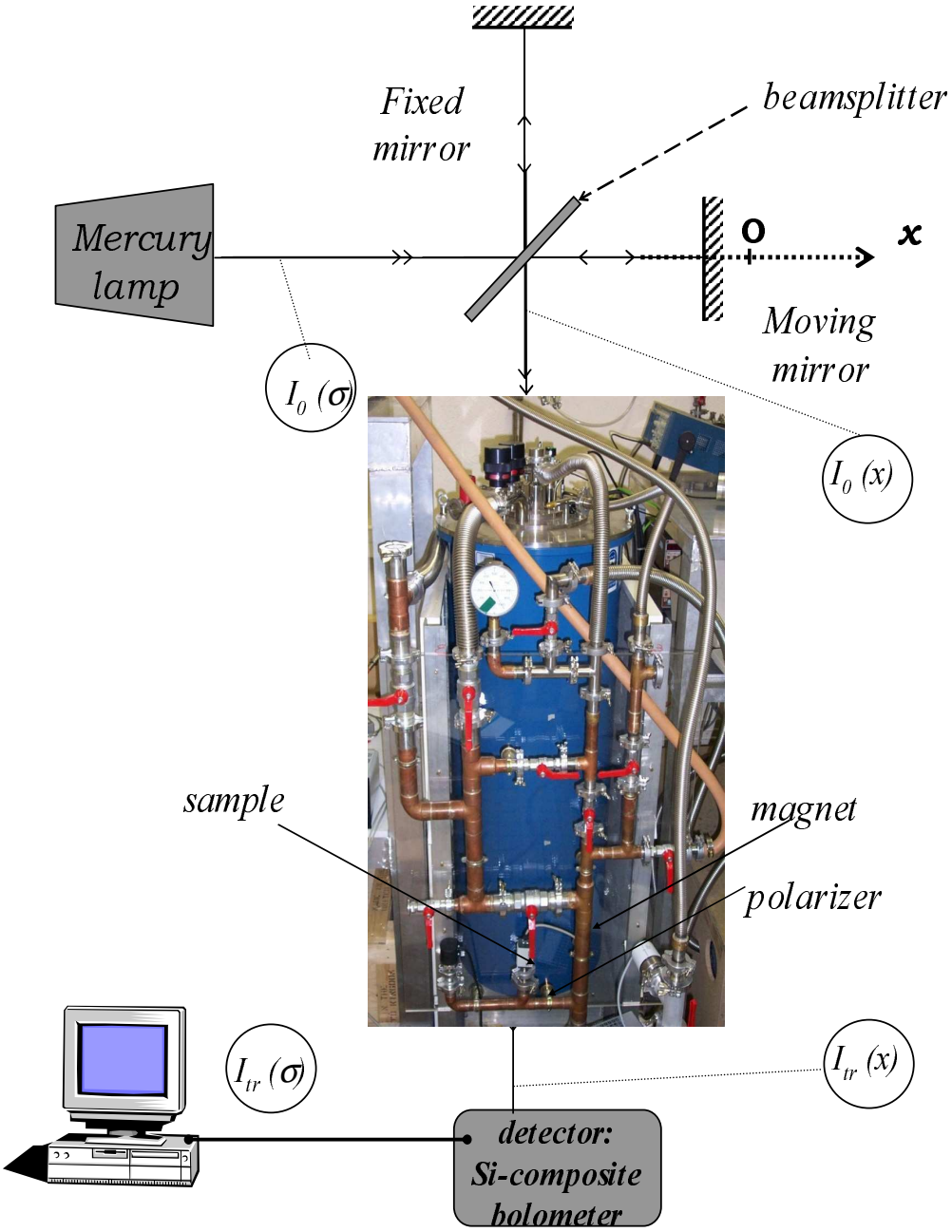

Figure 1.9: Schematic of the experimental setup, found at ENS in Paris, which measures the FIR transmission of a sample in polarized light and an applied magnetic field.

In order to obtain a transmission spectra containing only the features interesting to our study, we divide the transmission spectra of a sample by that of its substrate [$T(\sigma) = I_{sample}(\sigma)/I_{substrate}(\sigma)$]. The substrate is obtained by cutting a small rectangle from the sample wafer and sanding off the QD layers until we are left with just the GaAs substrate. The sample and substrate are mounted to the end of a pivoting rod. The rod can be rotated from outside the cryostat and therefore two spectra, $I_{sample}(\sigma)$ and $I_{substrate}(\sigma)$, can be measured in the same conditions, i.e. temperature, polarization, and incident light.

1.5.2 Magneto-Photoluminescence: Interband Transitions

During a photoluminescence (PL) experiment, electron-hole pairs are created by shining a laser on a sample. In the case of our QD samples, the pairs are trapped in the InAs islands and will relax to the ground state of the system ($s_e - s_h$). Finally, the pair recombines by emitting a photon, which we are able to detect with either a photomultiplier or a CCD (charge coupled device) camera.

In this thesis, three different types of PL measurements are used: non-resonant photoluminescence (NRPL), resonant photoluminescence (RPL) and photoluminescence excitation (PLE).

In both NRPL and RPL measurements, the excitation energy of the laser is fixed, while detection is possible in a certain energy range. For NRPL, the excitation energy is fixed to be superior or equal to the GaAs energy gap. Initially, electron hole pairs are created in the GaAs lattice which eventually relax down into the quantum dot states. In this way, we are assured the creation of an electron hole pair in all the dots. The resulting NRPL spectrum is therefore the sum of the contribution of all the dots. In the case of RPL, the excitation energy is lower than the GaAs gap and the InAs WL (see Fig. 1.5). As a result, electron hole pairs will only be created in QDs with discrete excited energy transitions that correspond to the given excitation energy.

Finally, unlike the two methods described above, in a PLE measurement the detection energy is fixed while the excitation energy is varied. The detection energy is chosen to correspond to the luminescence of certain dots in the sample. The excitation energy is then varied through a certain energy range. When an excitation energy coincides with an excited state transition in a QD, an electron hole pair is created. The pair relaxes to the ground state and finally the electron and hole recombine and emit a photon. A signal is detected, at the chosen fixed detection energy, each time the excitation energy corresponds to an excited state transition of a dot. PLE, therefore, measures a signal from a subensemble of dots in the sample whose ground state energy corresponds to the chosen detection energy. A summary of the three PL methods is presented in Table 1.2.

All the PL data presented in this thesis was collected at the High Magnetic Field Laboratory in Grenoble, in collaboration with Francis Teran and Marek Potemski. A schematic of the setup for a magneto-RPL or NRPL experiment is shown in Fig. 1.10. An Ar+ laser is used for non-resonant excitation and a Ti:sapphire laser for resonant excitation. A chopper coupled to a lock-in amplifier allows the elimination of any optical noise. A system of optical fibers is used for the sample excitation and the collection of the PL signal. The sample is immersed in a liquid helium bath which

is pumped to 4 K. A resistive magnet surrounds the cryostat such that a magnetic field up to 28 T can be applied along the sample growth axis. The emitted light from the sample is dispersed through a Jobin Yvon spectrometer and detected by a photomultiplier.

The PLE experiment has the same set-up described above but uses a Ti:sapphire laser and a CCD camera for the detection.

Method	Detection Energy	Excitation Energy	Select
Resonant Photoluminescence (RPL)	Varies	Fixed	QDs with excited energy transitions=$E_{excitation}$
Non-Resonant Photoluminescence (NRPL)	Varies	Fixed	All QDs
Photoluminescence Excitation (PLE)	Fixed	Varies	QDs with ground state energy =$E_{detection}$

Table 1.2: Summary of different PL methods used in this thesis.

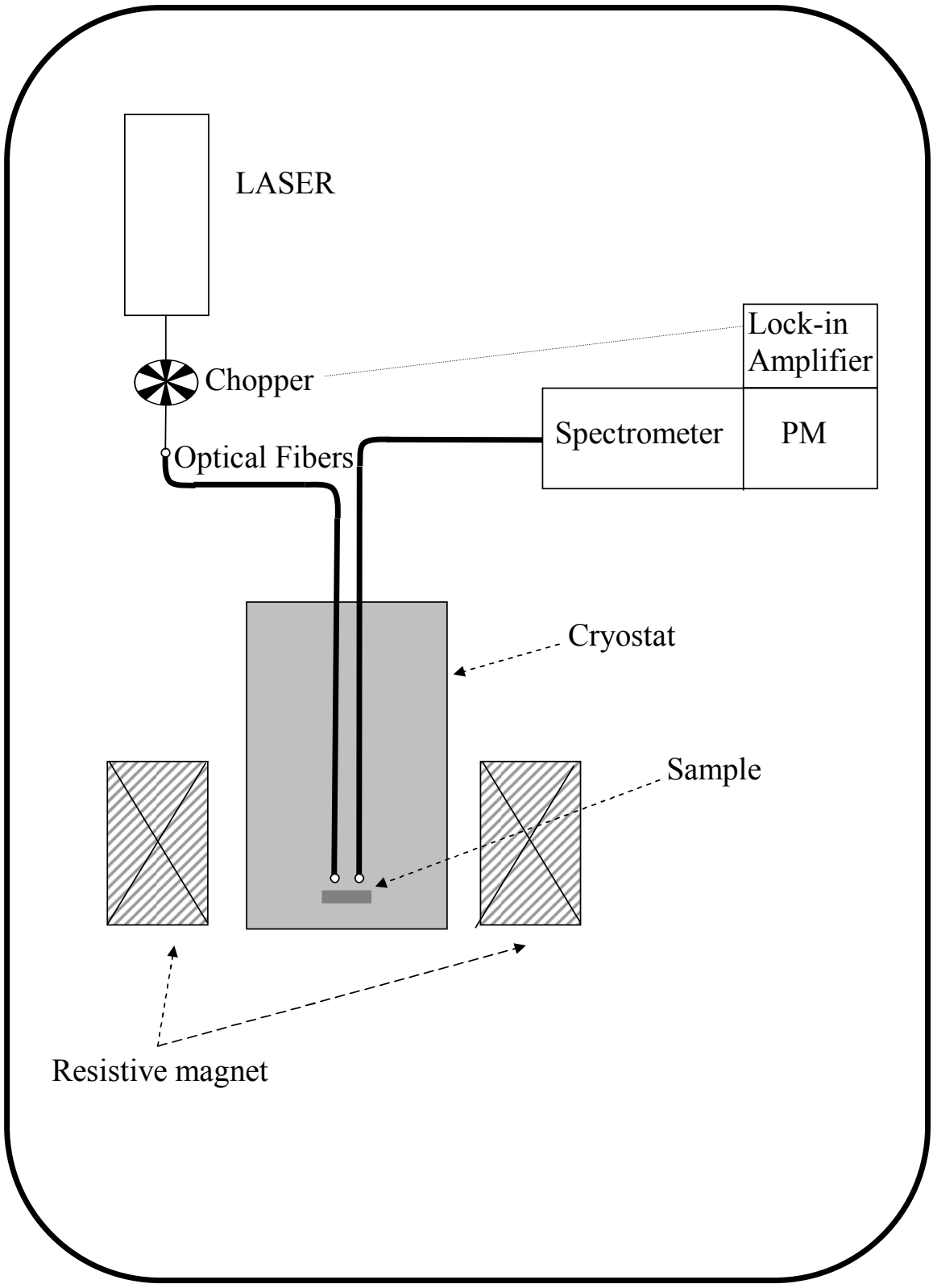

Figure 1.10: Schematic of the experimental setup, found at the High Magnetic Field Laboratory in Grenoble, which measures the RPL or NRPL signal in a high magnetic field.

1.5.3 Coupling to Light

The processes of both FIR spectroscopy and photoluminescence involve the interaction between electrons and light. It is therefore necessary to study the coupling between a charged carrier and an electromagnetic field in a QD.

In the general case, the Hamiltonian of an electron of charge $-e$ in the presence of an electric or magnetic field is written:

$$\mathbf{H} = \frac{1}{2m_0}\left(\vec{\mathbf{p}} - e\vec{\mathbf{A}}(\vec{\mathbf{r}},t)\right)^2 - e\phi(\vec{\mathbf{r}},t) + V(\vec{\mathbf{r}}) \tag{1.5}$$

where $\vec{\mathbf{A}}$ is the potential vector and ϕ the electrostatic potential. V represents the potential of the crystal lattice. The Hamiltonian $\mathbf{H} = \mathbf{H}_0 + \mathbf{H}_i$ can be written in the the Coulomb gauge ($\vec{\nabla}\cdot\vec{\mathbf{A}} = 0$, ϕ=0) as follows:

$$\mathbf{H}_0 = \frac{\mathbf{p}^2}{2m^*}; \quad \mathbf{H}_i = -\frac{e\vec{\mathbf{A}}\cdot\vec{\mathbf{p}}}{m^*} + \frac{e^2\mathbf{A}^2}{2m^*} \tag{1.6}$$

Neglecting the term in $\mathbf{A}^2$ and applying the electric dipole approximation the interaction Hamiltonian becomes [27, 28]:

$$\mathbf{H}_i = \vec{\varepsilon}\cdot\vec{\mathbf{p}}\frac{eE}{m^*\omega}\sin\omega t \tag{1.7}$$

where E is the amplitude of the electric field, $\vec{\varepsilon}$ the polarization of the EM wave, and ω its angular frequency. This term of the Hamiltonian is responsible for the provocation of the inter and intraband transitions of electrons. Indeed, the transition probability of an electron initially in the state $|\phi_i\rangle$ being excited to a final state $|\phi_f\rangle$ is proportional to:

$$P_{i\to f} \propto |\langle\phi_f|\vec{\varepsilon}\cdot\vec{\mathbf{p}}|\phi_i\rangle|^2 \tag{1.8}$$

The wavefunction of a carrier in a quantum dot can be separated into two parts: the envelope function times a plane wave, which we will label f_l (with $l = s$ or p), on the one hand and the periodic part of the Bloch function u_n on the other, where n is either the conduction or valence band. We therefore have the initial and final wavefunctions: $\phi_f = f_{l_f}u_{n_f}$ and $\phi_i = f_{l_i}u_{n_i}$. Expressing the wavefunctions as such, allows for the separation of the matrix element in Eq. 1.8 into two terms: one responsible for intraband transitions and one for interband transitions [29].

Intraband Transitions

We first examine the intraband term. This term is important when interpreting FIR measurements, where intraband transitions of a QD system are directly probed. The oscillator strength (OS) of these transitions is proportional to:

$$OS_{i\to f} \propto |\langle f_{l_i}|\vec{\varepsilon}\cdot\vec{\mathbf{p}}|f_{l_f}\rangle|^2 \tag{1.9}$$

We notice that only the envelope part of the wavefunction plays a role in the OS of intraband transitions. Since the initial and final Bloch states are identical for intraband transitions ($n_i = n_f$ = conduction or valence band), and these functions

oscillate rapidly compared to the envelope functions, their contribution to the OS can be neglected [29].

As a result of the symmetry of the states, for an EM wave polarized in the xy plane, only transitions between states whose orbital angular momentum differ by one ($\Delta l = \pm 1$) are permitted. For our QD systems, in which only the ground state $|s\rangle$ is populated, we find two allowed optical transitions, $|s\rangle \leftrightarrow |p_+\rangle$ and $|s\rangle \leftrightarrow |p_-\rangle$.

Interband Transitions

We now look at the interband term, important for interpreting PL results. The polarization selection rules depend on the Bloch function part of this term, $\langle u_{n_i}|\vec{\varepsilon}\cdot\vec{\mathbf{p}}|u_{n_f}\rangle$. We notice that the rules are the same as those of the bulk material. However, because of the broadening of the PL peak due to size inhomogeneity in self-assembled dot samples, our experiments are not sensitive to the effects of the above term.[¶] We are therefore only concerned by the envelope function contribution:

$$OS_{i\to f} \propto |\langle f_{l_i}|f_{l_f}\rangle|^2 \tag{1.10}$$

This term is non-zero only when the initial and final states have the same l. The allowed optical interband transitions are therefore of the type: $s \to s$, $p \to p \ldots$

1.5.4 Coupling to a Constant Magnetic Field

The applied magnetic field is an important parameter in our experiments. Here, we will study the effect of a constant magnetic field on the electronic states of a QD. We consider the situation of our experiments, i.e. a magnetic field B applied along the growth axis of the sample. The potential vector $\vec{\mathbf{A}}$ can therefore be written in the Coulomb gauge:

$$\vec{\mathbf{A}} = \frac{1}{2}(-By, Bx, 0) \tag{1.11}$$

In these conditions and neglecting the term in $\mathbf{A}^2$, Eq. 1.6 becomes

$$\mathbf{H} = \mathbf{H}_0 + \frac{eB}{2m^*}\mathbf{L}_z \tag{1.12}$$

The presence of a magnetic field introduces a term in the Hamiltonian proportional to the z-component of the angular momentum; the Zeemen effect.

Let us now look at the effect this new term has on the quantum dot energy states calculated in the previous section; s and p. As mentioned before, due to the cylindrical symmetry of the confinement potential, these states are eigenstates of $\mathbf{L}_z$. Therefore, the magnetic field does not couple the states between themselves. On the other hand, the magnetic field will affect the energies of these states:

$$\begin{aligned} E_s(B) &= E_s(0) \\ E_{p_+}(B) &= E_p(0) + \frac{\hbar eB}{2m^*} \\ E_{p_-}(B) &= E_p(0) - \frac{\hbar eB}{2m^*} \end{aligned} \tag{1.13}$$

[¶]see section 4.1.1 and Appendix A

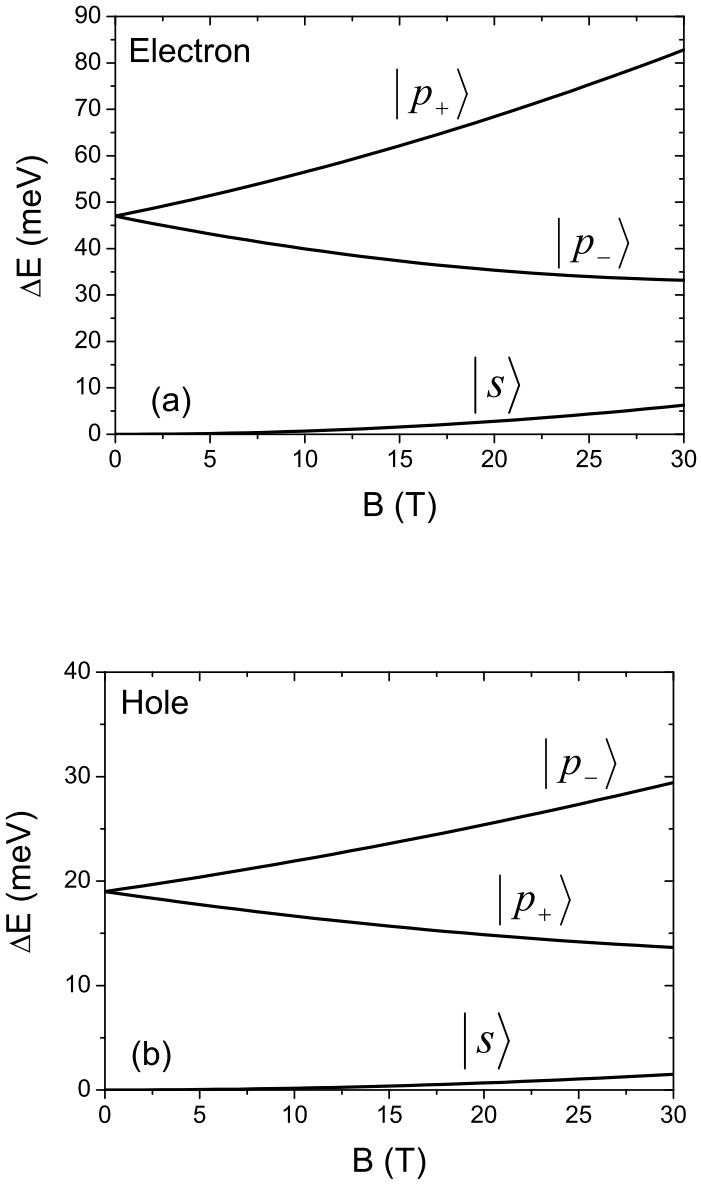

Figure 1.11: s and p state energies as a function of the B field, for an electron (a) of mass $m_e = 0.07m_o$ and a hole (b) of mass $m_h = 0.22m_o$, confined in a QD with R= 115 Å and h = 28 Å.

These equations suffice when dealing with small magnetic fields. However, for stronger magnetic fields (≈20 T), the term in A^2 of Eq. 1.6 can no longer be neglected. Taking this into account, we find the diamagnetic term:

$$\mathbf{H}_{dia} = \frac{e^2A^2}{2m^*} = \frac{e^2\rho^2}{8m^*}B^2 \tag{1.14}$$

The total effect of the magnetic field on the QD energy states is therefore the addition of a Zeeman term and a diamagnetic term:

$$\begin{aligned} E_s(B) &= E_s(0) + \frac{e^2\beta_s^2B^2}{8m^*} \\ E_{p_+}(B) &= E_p(0) + \frac{\hbar eB}{2m^*} + \frac{e^2\beta_p^2B^2}{4m^*} \\ E_{p_-}(B) &= E_p(0) - \frac{\hbar eB}{2m^*} + \frac{e^2\beta_p^2B^2}{4m^*} \end{aligned} \tag{1.15}$$

Figure 1.11 shows the evolution of the ground state, s, and two excited states, p_+ and p_-, of an electron (a) and a hole (b) confined in a QD as a function of the magnetic field. The zero energy is taken at the ground state energy at 0T, $E_s(0)$. The m^*s in Eq. 1.15 are replaced by m_e for an electron and m_h for a hole. In the calculation leading up to Eq. 1.15, we considered an electron in the presence of an EM field. With a simple change of charge sign ($-e \rightarrow +e$), this same calculation can be applied to a hole. As a result, for a hole, the p_+ ($l = +1$) energy level decreases in energy with the magnetic field while the p_- ($l = -1$) energy level increases, contrary to the case of an electron. The mass of a hole being heavier than that of an electron ($m_h = 0.22m_o$ compared to $m_e = 0.07m_o$), we find that the energy dispersion for an electron in a magnetic field is greater than that of a hole. Indeed, as shown in Fig. 1.11, the higher energy branch increases by 36 meV in 30 T for an electron compared to a 10 meV energy increase for the same variation in magnetic field for a hole. For both carriers, the diamagnetic effect becomes apparent for intense magnetic fields.

If we take into account the anisotropy discussed in the previous section, the p-state energies are now written:

$$\begin{aligned} E_{p_+}(B) &= E_p(0) + \sqrt{\left(\frac{\hbar\omega_c}{2}\right)^2 + (\delta_a)^2} + \frac{e^2\beta_p^2B^2}{4m^*} \\ E_{p_-}(B) &= E_p(0) - \sqrt{\left(\frac{\hbar\omega_c}{2}\right)^2 + (\delta_a)^2} + \frac{e^2\beta_p^2B^2}{4m^*} \end{aligned} \tag{1.16}$$

with $\omega_c = \frac{eB}{m^*}$. These energies, for a hole and for an electron, are shown in Fig. 1.12. We find that the p_+ and p_- energy levels are no longer degenerate at 0 T, but are separated by an energy equal to $2\delta_a$. The effect of the anisotropy on the p-states is most noticeable for low magnetic fields. For more intense B fields, the p-states with anisotropy (in solid lines in Fig. 1.12) are very close to those without anisotropy (in dashed lines in Fig. 1.12). In what follows $\tilde{p}_\pm$ will denote the two electronic levels that result from the excited states admixed by the anisotropy term, i.e. the solid lines in Fig. 1.12.

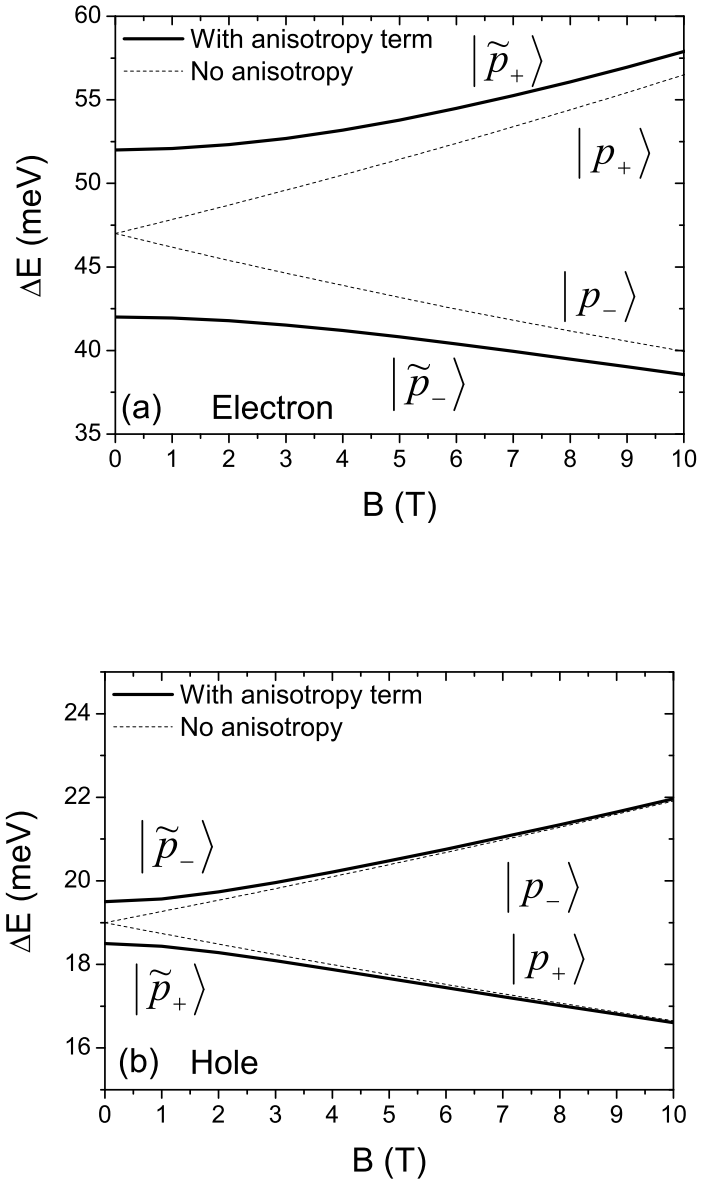

Figure 1.12: Energies of the p-states for an electron (a) and for a hole (b) as a function of magnetic field with anisotropy term included in the calculation (in solid lines) and without this term (dashed lines).The anisotropy term is $2\delta_a^e = 10$ meV for electrons and $2\delta_a^e = 1$ meV for holes. The other parameters can be found in Fig. 1.11.

1.6 Conclusion

A general background of QDs was presented in this chapter. It was shown that, using the Stranski Krastanov growth mode, it is possible to grow samples containing an ensemble of QDs in which carriers can be confined in all three directions of space. All the samples studied in this thesis were fabricated using this method.

A presentation of the calculation of the confined states was then given, where we found that a carrier possesses discrete energy levels labeled by its z-direction angular momentum.

We have given a detailed description of the two experimental methods used to study these QD states. Far-infrared magnetospectroscopy and near-infrared magnetophotoluminescence are employed to probe respectively the intraband and interband transitions of the system.

Finally, we have examined the interaction between a carrier trapped in a QD with light as well as with a magnetic field: situation which arises in the experiments. The QD intra and interband selection rules were established along with the evolution of the QD energy levels as a function of magnetic field.

Although we have found that QDs present many of the same attributes as atoms, we have already begun to discover the deficiency of the artificial atom model i.e. dots display an in-plane anisotropy. In the following chapters, we will further show that, because QDs are embedded in a semiconductor lattice, this simple image does not hold true. Indeed, the interaction between a charged carrier in a dot and its semiconductor environment, in particular the crystal lattice vibrations, differentiates dots from the isolated atom.

Bibliography

[1] N. Kirstaedter, N.N. Ledentsov, M. Grundmann, D. Bimberg, V.M. Ustinov, S.S. Ruvimov, M.V. Maximov, P.S. Kop'ev, Zh.I. Alferov, U. Richter, P. Werner, U. Gösele, and J. Heydenreich, *Low threshold, large T_o injection laser emission from (InGa)As quantum dots*, Electronics Lett. **30**, 1416 (1994).

[2] Y. Arakawa and H. Sakaki, *Multidimensional quantum well laser and temperature dependence of its threshold current*, Appl. Phys. Lett. **40**, 939 (1982).

[3] D. DiVencenzo, *The Physical Implementation of Quantum Computation*, Fortschr. Phys. **48**, 771 (2000).

[4] L.Goldstein, F. Glas, J.Y. Marzin, M.N. Charasse, and G. Leroux, *Growth by molecular beam epitaxy and characterization of InAs/GaAs strained-layer superlattices*, Appl. Phys. Lett. **47**, 1099 (1985).

[5] J. M. Gérard, J. B. Génin, J. Lefebvre, J. M. Moison, N. Lebouché and F. Barthe, *Optical investigation of the self-organized growth of InAs/GaAs quantum boxes*, J. Crystal Growth **150**, 351 (1995).

[6] B. Legrand, J.P. Nys, B. Grandidier, D. Stiévenard, A. Lemaître, J.M. Gérard, and V. Thierry-Mieg, *Quantum box size effect on vertical self-alignment studied using cross-sectional scanning tunneling microscopy*, Appl. Phys. Lett. **74**, 2608, (1999).

[7] G. S. Solomon, J. A. Trezza, and J. S. Harris, *Effects of monolayer coverage, flux ratio, and growth rate on the island density of InAs islands on GaAs*, Appl. Phys. Lett. **66**, 3161 (1995).

[8] G. S. Solomon, J. A. Trezza, and J. S. Harris, *Substrate temperature and monolayer coverage effects on epitaxial ordering of InAs and InGaAs islands on GaAs*, Appl. Phys. Lett. **66**, 991(1995).

[9] J. M. Moison, F. Houzay, F. Barthe, L. Leprince, E. André, and O. Vatel, *Self-organized growth of regular nanometer-scale InAs dots on GaAs*, Appl. Phys. Lett. **64**, 196 (1994).

[10] M. Fricke, A. Lorke, J.P. Kotthaus, G. Medeiros-Ribeiro, and P.M. Petroff, *Shell structure and electron-electron interaction in self-assembled InAs quantum dots*, Europhys. Lett. **36**, 197 (1996).

[11] B. Grandidier, Y. M. Niquet, B. Legrand, J. P. Nys, C. Priester, D. Stiévenard, J. M. Gérard and V. Thierry-Mieg, *Imaging the Wave-Function Amplitudes in Cleaved Semiconductor Quantum Boxes*, Phys. Rev. Lett., 85, 1068 (2000).

[12] O. Stier, *Electronic and Optical Properties of Quantum Dots and Wires*, Wissenschaft und Technik Verlag, (2001).

[13] L.-W. Wang, J. Kim, and A. Zunger, *Electronic structures of [110]-faceted self-assembled pyramidal InAs/GaAs quantum dots*, Phys. Rev. B **59**, 5678 (1999).

[14] S. Lee, L. Jönsson, J.W. Wilkins, G.W. Bryant, and G. Klimeck, *Electron-hole correlations in semiconductor quantum dots with tight-binding wave functions* Phys. Rev. B **63**, 195318 (2001).

[15] J.-Y. Marzin and G. Bastard, *Calculation of the energy levels in InAs/GaAs Quantum Dots*, Solid State Commun. **92** 437, (1994).

[16] A. Vasanelli, Ph.D. thesis, *Transitions optiques interbandes et intrabandes dans les boîtes quantiques simples et couplées verticalement*, Université Paris VI (2002).

[17] S. Hameau, J.N. Isaia, Y. Guldner, E. Deleporte, O. Verzelen, R. Ferreira, G. Bastard, J. Zeman, and J.M. Gérard, *Far-infrared magnetospectroscopy of polaron states in self-assembled InAs/GaAs quantum dots*, Phys. Rev. B **65**, 085316 (2002).

[18] S. Hameau, Y. Guldner, O. Verzelen, R. Ferreira, G. Bastard, J. Zeman, A. Lemaître, and J.M. Gérard, *Strong Electron-Phonon Coupling Regime in Quantum Dots: Evidence for Everlasting Resonant Polarons*, Phys. Rev. Lett. **83**, 4152 (1999).

[19] G. Bester, S. Nair, and A. Zunger, *Pseudopotential calculation of the excitonic fine structure of million-atom self-assembled $In_{1-x}Ga_xAs/GaAs$ quantum dots*, Phys. Rev. B **67**, 161306 (2003).

[20] V. Preisler, R. Ferreira, S. Hameau, L. A. de Vaulchier, Y. Guldner, M. L. Sadowski, and A. Lemaître, *Hole-LO phonon interaction in InAs/GaAs quantum dots*, Phys. Rev. B **72**, 115309 (2005).

[21] O. Verzelen, Ph.D. thesis, *Interaction électron-phonon LO dans les boîtes quantiques d'InAs/GaAs*, Université Paris VI (2002).

[22] M. Levinshtein, S. Rumyantsev, and M. Shur, ed., *Semiconductor Parameters: Volume 1*, World Scientific (1996).

[23] J.N. Isaia, Ph.D. thesis, *Niveaux électronique et interaction électron-phonons dans les boîtes quantiques d'InAs/GaAs*, Université Paris VI (2002).

[24] P. B. Joyce, T. J. Krzyzewski, G. R. Bell, B. A. Joyce, and T. S. Jones, *Composition of InAs quantum dots on GaAs(001): Direct evidence for (In,Ga)As alloying*, Phys. Rev. B **58**, R15981 (1998).

[25] Y. Hasegawa, H. Kiyama, Q.K. Xue, and T. Sakurai, *Atomic structure of faceted planes of three-dimensional InAs islands on GaAs(001) studied by scanning tunneling microscope*, Appl. Phys. Lett. **72**, 2265 (1998).

[26] R.J. Bell, *Introduction to Fourier Transform Spectroscopy*, Academic Press (1972).

[27] C. Cohen-Tannoudji, B. Diu, and F. Laloë, *Mécanique Quantique*, Hermann (1973).

[28] P. Yu, and M. Cardona, *Fundamentals of Semiconductors*, Springer-Verlag (1999).

[29] G. Bastard, *Wave mechanics applied to semiconductor heterostructures*, Les Editions de Physique (1996).

Chapter 2

Electronic Polarons

Various theoretical and experimental results have demonstrated that carriers confined in QDs are strongly coupled to the longitudinal optical vibrations of the underlying semiconductor lattice [1]-[7]. For conduction electrons, this coupling leads to the formation of the so-called electronic polaron. The electronic polaron has been extensively studied by intraband magneto-optical transitions in n-doped dots, most notably in the thesis of J.N. Isaia and S. Hameau [8, 9]. In this thesis, new results that study these electronic polarons in polarization and a magnetic field simultaneously are presented. The first section will present a description of the calculation of polaron states.* This calculation will be useful throughout the thesis, as it can be applied, with minor adjustments, to hole polaron states (Chapter 3) and excitonic polaron states (Chapters 4 & 5). Next, an overview of the experimental evidence of electron polarons in high magnetic field will be given. Finally, new magnetotransmission results in polarization will be presented. The oscillator strength of the polaron states will be calculated in order to understand these results.

2.1 Calculation of Polaron States

2.1.1 The Fröhlich Hamiltonian

Both GaAs and InAs are crystals that contain two atoms per elementary unit cell. In such crystals, there exists 6 phonon modes for each wave vector $\vec{\mathbf{q}}$: three acoustic modes, which, for $\vec{\mathbf{q}} \rightarrow 0$, correspond to the in phase vibrations of the two atoms in the elementary cell, and three optical modes, which correspond to the out of phase vibrations of the two atoms. The out of phase vibrations of the two atoms in the longitudinal optical (LO) mode create a dipole. A charged carrier in such a material is affected by the electric potential created by this dipole.

In bulk materials, the Fröhlich Hamiltonian describes the Coulomb interaction between a moving charge and these dipole vibrations. This Hamiltonian is expressed [11]

$$\mathbf{V}_F = \sum_{\vec{\mathbf{q}}} \frac{iA_F}{q\sqrt{V}} (e^{i\vec{\mathbf{q}}\cdot\vec{\mathbf{r}}} \mathbf{a}^+_{\vec{\mathbf{q}}} - c.c.) \tag{2.1}$$

*A more detailed explanation of this calculation can be found in the thesis of O. Verzelen [10].

where $\mathbf{a}_{\vec{\mathbf{q}}}^{+}$ is the phonon creation operator, $\vec{\mathbf{r}}$ is the position operator of the carrier, V is the volume of the crystal and the coefficient A_F is given by

$$A_F = e\sqrt{\frac{\hbar\omega_{LO}}{2\epsilon_o}\left(\frac{1}{\kappa_\infty} - \frac{1}{\kappa_o}\right)} \tag{2.2}$$

where ϵ_o is the permittivity of free space. We notice that the Fröhlich interaction depends on the high frequency permittivity constant κ_∞ (10.9 for GaAs and 12.3 for InAs) and the static permittivity constant κ_o (12.9 for GaAs and 15.6 for InAs) of the material as well as the energy $\hbar\omega_{LO}$ of the LO phonons ($\approx$ 36 meV for GaAs and $\approx$ 29 meV for InAs)[12].

The strength of this interaction can be gauged by the value of the dimensionless Fröhlich constant α_F of a crystal, which characterizes its ionicity. We have the following relation between α_F and A_F:

$$\alpha_F = \frac{\sqrt{2m^*}}{4\pi\hbar(\hbar\omega_{LO})^{3/2}}A_F^2 \tag{2.3}$$

where m^* is the effective electron mass of the material. For GaAs and InAs, we find $\alpha_F(\text{GaAs}) \approx 0.06$ and $\alpha_F(\text{InAs}) \approx 0.05$.[†]

The above description of the Fröhlich Hamiltonian is valid for bulk materials. In QDs, the phonon spectra are not known accurately as a result of the uncertainties of the shape and composition of the dots. But since an actual InAs island consists of several thousand unit cells, we can expect the dot to have a quasibulk phonon spectra. In addition, as in III-V bulk, each anion is surrounded by four cations with a slightly polar bond between them. The basic ingredients of the Fröhlich Hamiltonian are maintained in actual dots. In our calculations, we will therefore use the Fröhlich Hamiltonian taking the dimensionless Fröhlich constant α_F as an adjustable parameter and use the same phonon energies as in the bulk material.

The states of the QD system, which now include LO phonons, are labeled $|\upsilon, n_{\vec{\mathbf{q}}}\rangle$ where $|\upsilon\rangle = |s\rangle, |p_\pm\rangle$ are the purely electronic states calculated in the previous chapter and $|n_{\vec{\mathbf{q}}}\rangle$ denotes the number n of LO phonons with wavevector $\vec{\mathbf{q}}$. Taking into account this new interaction the Hamiltonian of our QD system can now be written:

$$\mathbf{H} = \mathbf{H}(B) + \mathbf{V}_a + \mathbf{H}_{ph} + \mathbf{V}_F \tag{2.4}$$

where $\mathbf{H}(B) = \mathbf{H}_o + \mathbf{H}_{Zeeman} + \mathbf{H}_{dia}$, $\mathbf{H}_{ph}$ is the LO phonon Hamiltonian and $\mathbf{V}_a$ is the anisotropy term.

2.1.2 Strong or Weak Coupling

In bulk, 2D and 1D systems, the Fröhlich Hamiltonian introduces an interaction between two continuums of states: the broad continuum of the electronic states (several eVs) and the narrow continuum of the phonon states (several meVs). In this case, Fermi's Golden rule can be applied and the irreversible relaxation of a carrier in a particular state, to a state of lower energy accompanied by the emission of one or

[†]See Appendix B

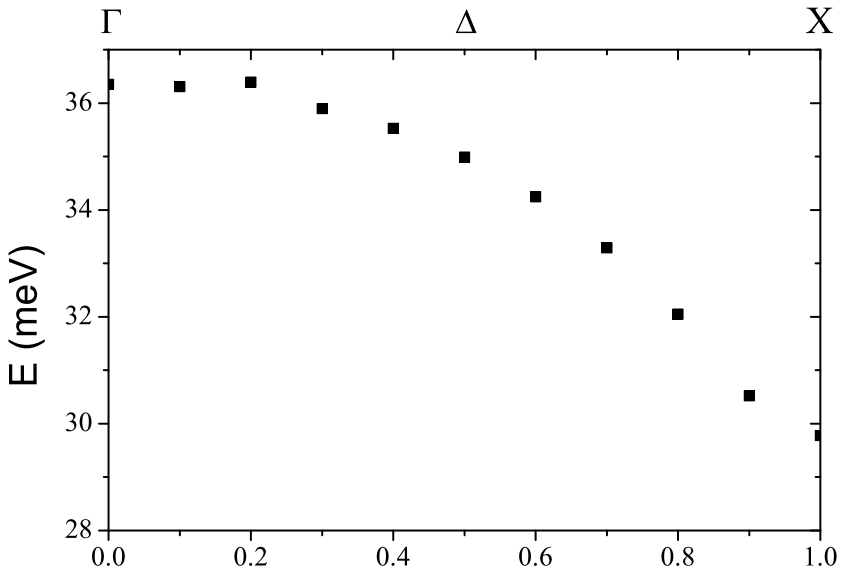

Figure 2.1: Phonon dispersion curve in GaAs along the high symmetry axis $\Gamma - \Delta - X$ found in reference [15].

several LO phonons is expected. The probability of finding the carrier in its initial state decays exponentially over time. This is called a weak coupling [13].

Now let's consider a system of two discrete levels, whose energies without coupling cross. In the presence of a coupling term, the two levels "repel each other" and an anti-crossing is observed. The probability of finding the system, which was initially in the first state, in the second state oscillates over time. This is called a strong coupling [14].

In QD systems, the Fröhlich Hamiltonian provokes an interaction between a discrete state (the electronic state of the QD) and a narrow continuum of phonon states. It can be shown that this interaction can result in either a weak coupling (as in the case of bulk materials) or a strong coupling (as in the case of a two discrete level system) [14, 10]. The type of coupling depends on the relationship between the width of the continuum, δ, and the strength of the coupling term, V_{eff} (to be defined). If $\delta \ll V_{eff}$ a strong coupling takes place and if, on the contrary, $\delta \gg V_{eff}$, a weak coupling is expected.

In the next section it will be demonstrated that for our samples, V_{eff} is on the order of 4 meV. The coupling regime of the QD system can therefore be determined by comparing this V_{eff} with the width of the phonon continuum in interaction with the carrier. The width of the phonon continuum of GaAs (InAs) spanning the first Brillouin zone is approximatively 6 meV (3 meV), as seen in Fig. 2.1. The extension of the continuum in interaction with the electronic states can be approximated by calculating the matrix element of the Fröhlich Hamiltonian between two discrete QD states, $\langle \upsilon_i, n^i_{\vec{\mathbf{q}}} | \mathbf{V}_F | \upsilon_f, n^f_{\vec{\mathbf{q}}} \rangle$. The Fröhlich Hamiltonian only directly couples states

whose phonon occupation number differ by one ($n^f - n^i = \Delta n = \pm 1$). We find[‡]

$$\begin{aligned} |V_{if}(\vec{\mathbf{q}})| &= |\langle \upsilon_i, n^i_{\vec{\mathbf{q}}} | \mathbf{V}_F | \upsilon_f, n^f_{\vec{\mathbf{q}}} \rangle| \\ &= |\frac{\tilde{A}_F}{q} \langle \upsilon_i | e^{\pm i \vec{\mathbf{q}} \cdot \vec{\mathbf{r}}} | \upsilon_f \rangle| \\ &\propto \exp(-\frac{q_\rho^2 \beta_{if}^2}{4} - \frac{q_z^2 \sigma_{if}^2}{4}) \end{aligned} \tag{2.5}$$

where β_{if}^2 and σ_{if}^2 are constants which depend on the parameters of the wavefunctions of the two quantum dot states.[§] For a dot size typical of our samples, $\beta_{if} \approx 45$ Å and $\sigma_{if} \approx 20$ Å. Consequently, the coupling term will go to zero for $q >> \frac{1}{45\text{Å}} \approx 0.022$ Å^{-1}. We find that the coupling is negligible for phonons far from the center of the Brillouin zone. More precisely, it can be demonstrated [10] that the coupling term is significant only for phonons with a wavevector $q < q_{max} \approx 0.2$ Å^{-1}, resulting in an effective width of the phonon continuum of around 0.1 meV. This value being small compared to our V_{eff}, we conclude that the QD system (carrier plus LO phonons) is in a strong coupling regime. In addition, as we have shown that the dispersion of the LO phonons in the concerned region is very small, we will from now on consider the phonons as monochromatic.

2.1.3 The Effective Potential

In the above discussion, we established that a carrier in a dot is strongly coupled to the LO phonons of the surrounding lattice. We are now interested in calculating the resulting eigenstates and energies of this coupling. In essence, the carrier is coupled to all phonons that possess a wavevector close to the center of the Brillouin zone. This means that one would have to calculate, for example in the case where Δn=1, the coupling between the discrete electronic levels of the carrier, $|\upsilon_i, 0\rangle$, and the one phonon states $|\upsilon_j, 1_{\vec{\mathbf{q}}}\rangle$ for every wavevector in the concerned region. To avoid this laborious calculation, we will exploit the fact that the phonons can be treated as dispersionless and therefore all have the same energy, $\hbar\omega_{LO}$. Within this dispersionless phonon approximation, any linear combination of the degenerate one phonon states $|1_{\vec{\mathbf{q}}}\rangle$ will also have the energy, $\hbar\omega_{LO}$. We introduce a particular linear combination

$$|1_\alpha\rangle = \sum_{\vec{\mathbf{q}}} \frac{V_\alpha(\vec{\mathbf{q}})|1_{\vec{\mathbf{q}}}\rangle}{V_{eff}}, \tag{2.6}$$

where we now define V_{eff}, the effective coupling term introduced above,

$$\langle \upsilon_1, 1_\alpha | \mathbf{V}_F | \upsilon_2, 0 \rangle = \sqrt{\sum_{\vec{\mathbf{q}}} |V_\alpha(\vec{\mathbf{q}})|^2} = V_{eff} \tag{2.7}$$

[‡] $\tilde{A}_F = \frac{iA_F}{\sqrt{V}}$

[§] $\beta_{if}^2 = \frac{2\beta_i^2\beta_f^2}{\beta_i^2+\beta_f^2}, \sigma_{if}^2 = \frac{2\sigma_i^2\sigma_f^2}{\sigma_i^2+\sigma_f^2}$

with $V_\alpha(\vec{\mathbf{q}})$ the matrix element of the Fröhlich Hamiltonian defined in Eq. 2.5. We label

$$|1_{\{\beta\}}\rangle = \sum_{\vec{\mathbf{q}}} U_{\{\beta\}}(\vec{\mathbf{q}})|1_{\vec{\mathbf{q}}}\rangle \tag{2.8}$$

the remaining set of one-phonon combinations orthogonal to $|1_\alpha\rangle$. Thus, we have

$$\langle 1_{\{\beta\}}|1_\alpha\rangle = \sum_{\vec{\mathbf{q}},\vec{\mathbf{q}}'} \frac{U^*_{\{\beta\}}(\vec{\mathbf{q}}')V_\alpha(\vec{\mathbf{q}})}{V_{eff}}\langle 1_{\vec{\mathbf{q}}'}|1_{\vec{\mathbf{q}}}\rangle = \sum_{\vec{\mathbf{q}}} \frac{U^*_{\{\beta\}}(\vec{\mathbf{q}})V_\alpha(\vec{\mathbf{q}})}{V_{eff}} = 0 \tag{2.9}$$

It follows that

$$\langle \upsilon_1, 1_{\{\beta\}}|\mathbf{V}_F|\upsilon_2, 0\rangle = \sum_{\vec{\mathbf{q}}} U^*_{\{\beta\}}(\vec{\mathbf{q}})\frac{\tilde{A}_F}{q}\langle \upsilon_1|e^{i\vec{\mathbf{q}}\cdot\vec{\mathbf{r}}}|\upsilon_2\rangle = \sum_{\vec{\mathbf{q}}} U^*_{\{\beta\}}(\vec{\mathbf{q}})V_\alpha(\vec{\mathbf{q}}) = 0 \tag{2.10}$$

We have demonstrated that the remaining orthogonal space $|\upsilon_1, 1_{\{\beta\}}\rangle$ is left uncoupled to the discrete level $|\upsilon_2, 0\rangle$. We now see how creating these linear combinations greatly simplifies the calculation. A discrete energy level coupled to a phonon continuum of N different modes is equivalent to $N-1$ uncoupled modes plus a two level system coupled by a potential V_{eff}.

2.1.4 A Simple Example: one discrete state coupled to one continuum state

To concretize the ideas detailed above, let's take the example of the coupling between the discrete electron state $|p_-, 0\rangle$ and the one phonon continuum $|s, 1_{\{\vec{\mathbf{q}}\}}\rangle$. Using the effective potential method, we find that $|p_-, 0\rangle$ is coupled to one discrete state $|s, 1_{\alpha(sp_-)}\rangle$ where

$$|1_{\alpha(sp_-)}\rangle = \sum_{\vec{\mathbf{q}}} \frac{V_{sp_-}(\vec{\mathbf{q}})|1_{\vec{\mathbf{q}}}\rangle}{V_{eff}(sp_-)}, \tag{2.11}$$

Using Eq. 2.4, we find the Hamiltonian for this two level system

$$H = \begin{pmatrix} E_{p_-}(B) & V_{eff}(sp_-) \\ V_{eff}(sp_-) & E_s(B) + \hbar\omega_{LO} \end{pmatrix} \tag{2.12}$$

By diagonalizing this matrix, the eigenvalues of the Hamiltonian are easily found:

$$E = \frac{E_s(B) + \hbar\omega_{LO} + E_{p_-}(B) \pm \sqrt{[E_s(B) + \hbar\omega_{LO} - E_{p_-}(B)]^2 + 4V^2_{eff}(sp_-)}}{2} \tag{2.13}$$

The new eigenvalues of the coupled system are traced in Fig. 2.2, along with the uncoupled state energies as a function of the magnetic field. The zero energy is taken

at the ground state, $E_s(B)$. We have used the same dot parameters as in Fig. 1.11 and the LO phonon energy of GaAs. With these values, using Eq. 2.7, we find a $V_{eff} = 3.6$ meV.

The coupling of the two states results in two new states, labeled (U) and (L) in Fig. 2.2, that display an anti-crossing of magnitude $2V_{eff}$. These two states, called polaron states, are the result of the strong coupling that takes place between the lattice and electronic excitations. In the general case, we find that for a system of M continuum states and m discrete states, we obtain $m(M+1)$ polaron states.

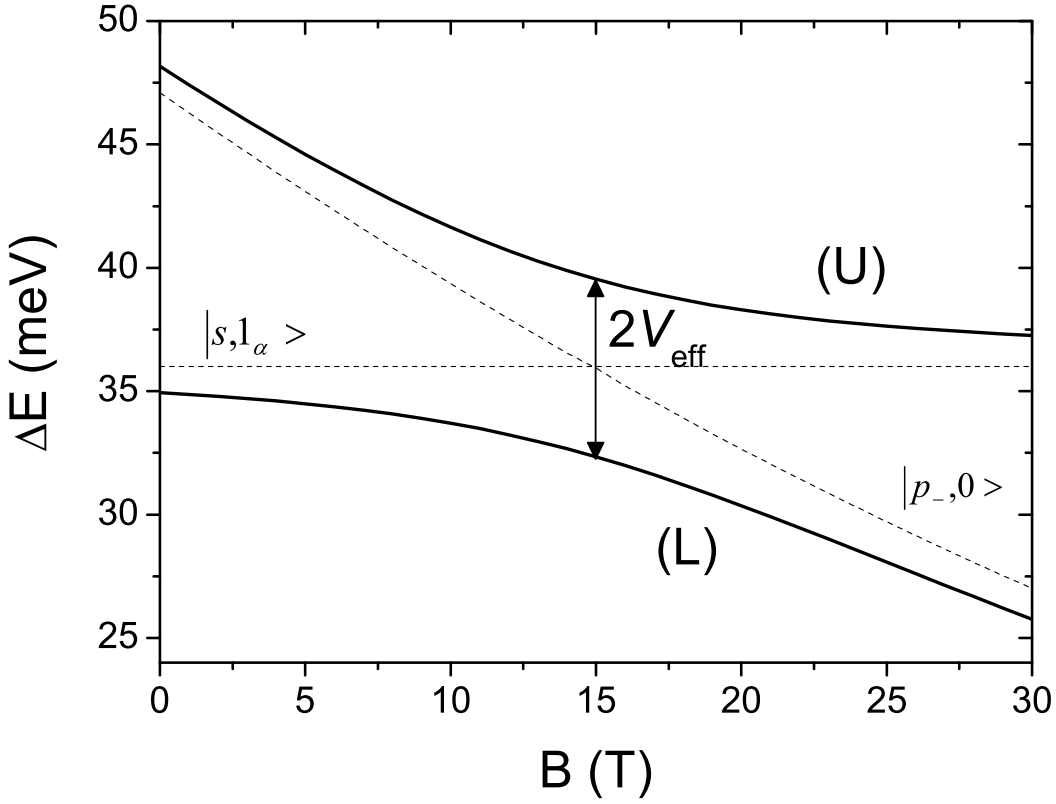

Figure 2.2: Anti-crossing of two polaron states (U) and (L) coupled by a potential $V_{eff} = 3.6$ meV. In dashed lines the uncoupled states for dot parameters $m_e = 0.07m_o$, R= 115 Å, h = 28 Å and phonon energy $\hbar\omega_{LO} = 36$ meV. The origin is taken to be the ground state energy, $E_s(B)$.

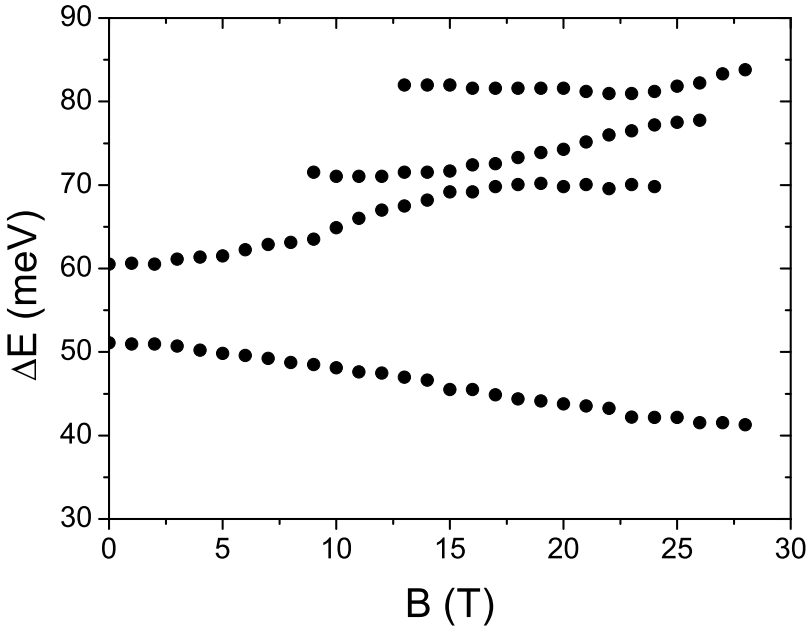

Figure 2.3: Magnetic field dispersion of the FIR resonances for sample N1.

2.2 Evidence of Electronic Polarons

In this section, the results of FIR magnetotransmission experiments measured on sample N1 and conducted in the conditions described in Section 1.5.1 will be presented. Sample N1 was doped in order to obtain, on average, one electron per dot. The single electron will initially be found in the ground state of the QD system, $|s,0\rangle$. The allowed intraband energy transitions are therefore to the $|p_+,0\rangle$ and $|p_-,0\rangle$ states, as demonstrated in Section 1.5.3.

2.2.1 High Magnetic Fields Experiments

The validity of the above polaron model has been demonstrated in the thesis of J.N. Isaia and S. Hameau. We will present here results reported in these thesis. Figure 2.3 displays the magnetic dispersion results measured for sample N1 up to $B = 28$ T in unpolarized light. Four branches are observed with three incidences of anti-crossings: at 70 meV for a a magnetic field of 16 T, at 80 meV for $B = 25$ T and the top branch of an anti-crossing at 40 meV. We therefore find the signature behavior of a strong coupling regime.

Let us now attempt to theoretically reproduce the experimentally observed anti-crossings. We start by finding all the uncoupled QD states in the energy region of the experimental results, i.e. 30 - 90 meV above the ground state energy E_s. Taking a dot with R=106 Å and h=23 Å, we find the five states shown in Fig. 2.4, whose

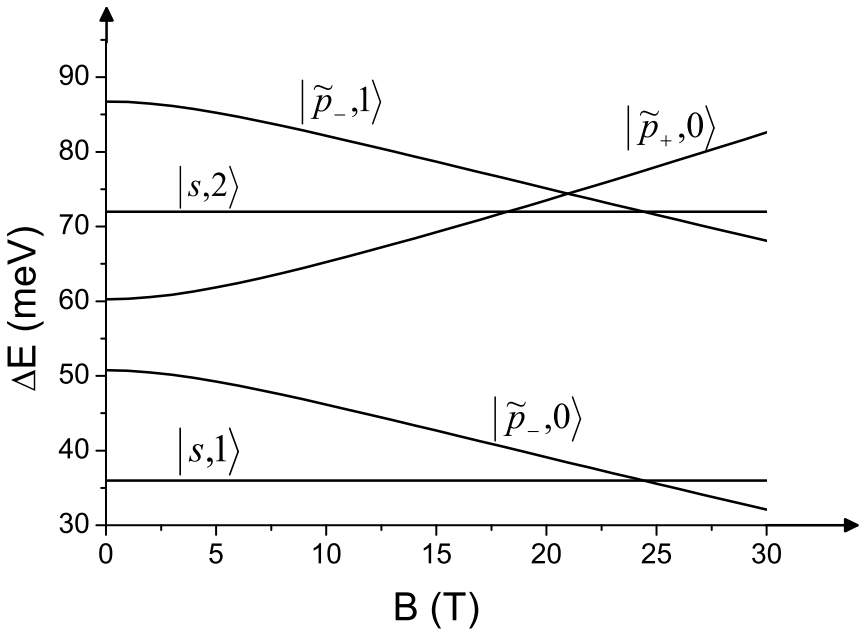

Figure 2.4: Energies versus B field of the electron-phonon states in the absence of the Fröhlich interaction. The energies were found using Eq. 1.16 with $m_e = 0.07m_o$, $2\delta_a = 11$ meV and $E_p(0) - E_s(0) = 55$ meV. The origin is taken at $E_s(B)$.

energies are plotted as a function of magnetic field. The other parameters used are listed in the figure caption. There are three occasions for a strong coupling interaction to occur in such a system:

- The crossing at 24 T between the discrete energy state $|p_-, 0\rangle$ and the one phonon continuum state $|s, 1_{\{\vec{\mathbf{q}}\}}\rangle$
- The crossing at 21 T between the discrete energy state $|p_+, 0\rangle$ and the one phonon continuum state $|p_-, 1_{\{\vec{\mathbf{q}}\}}\rangle$
- The crossing at 24 T between the one phonon continuum state $|p_-, 1_{\{\vec{\mathbf{q}}\}}\rangle$ and the two phonon continuum state $|s, 2_{\{\vec{\mathbf{q}}\},\{\vec{\mathbf{q}}'\}}\rangle$

The first crossing is exactly the situation treated in the previous section: one discrete state coupled to one continuum state. The coupling results in the appearance of two new polaron states that display an anti-crossing of magnitude $2V_{eff}(sp_-) \approx 9.2$ meV.

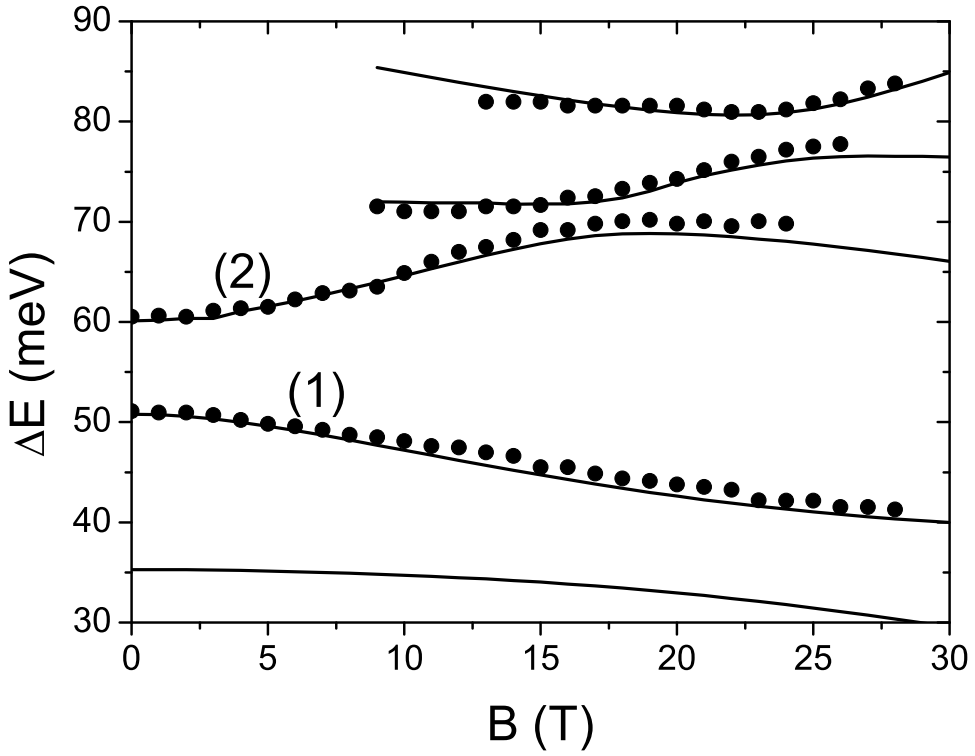

Figure 2.5: Experimental magnetic field dispersion in solid symbols compared with the calculated magnetic field dispersion in solid lines. A Fröhlich constant $\alpha_F = 0.075$ ($A_F = 0.00224$ meV·m^{-1}) was used. The rest of the parameters for the fit are given in Fig. 2.4 and the text.

The two final crossings present a more complicated situation. Using the effective potential method, we find that $|p_+, 0\rangle$ is coupled to one discrete state $|p_-, 1_\beta\rangle$ by a potential $V_{eff}(p_+p_-) \approx 3.6$ meV. In turn, $|p_-, 1_\beta\rangle$ is coupled to the discrete state $|s, 1_\beta, 1_\alpha\rangle$ by a coupling potential $V_{eff}(sp_-) \approx 4.6$ meV. We therefore find ourselves with a three level system that will result in 3 new polaron states.

This three level system is coupled to the two level system by the anisotropy term, which couples $|p_+, 0\rangle$ with $|p_-, 0\rangle$. To find the polaron states of the system, it is therefore necessary to solve a 5×5 matrix problem.

In Fig. 2.5, the results of the polaron calculation, in solid lines, are presented with the experimental results in symbols. A very good agreement is observed between theory and experiment. The lowest polaron branch is not observed because its energy coincides with that of the restrahlen band of the GaAs substrate. Between 31 and 37 meV, light penetrating the sample is completely absorbed by the transverse optical (TO) phonons of the substrate.

We can conclude that these experimental results provide evidence that an electron trapped in a QD is in a strong coupling regime with the LO phonons of the surrounding lattice. In addition, we find that the polaron model described in the previous section is able to successfully reproduce our experimental results.

2.2.2 Study of Electronic Polarons in Polarization

Above, we recalled previous experimental and theoretical works which showed the effectiveness of the polaron model in predicting the magnetic dispersion curves of our sample. We present here new experimental and theoretical studies of electronic polarons in polarization. We will focus on the intensity of the polaron absorptions which, we will observe, also vary greatly with an applied magnetic field. New magnetotransmission results performed in polarization are used for this study.

Figure 2.6 displays the magnetotransmission spectra for radiation polarized along the [110] direction of sample N1 and recorded at 2 K from $B = 0$ to 15 T every tesla. At 0 T, one strong absorption in observed at 60 meV. As the magnetic field increases, the absorption increases in energy all the while decreasing in intensity. At around 12 T, the beginning of an anti-crossing is observed and a small absorption starts to be detected at 72 meV, slightly above the main absorption. At lower energies, an absorption appears at a field of 3 T and at an energy of 51 meV. This absorption gets stronger with the magnetic field and decreases in energy. Finally, between 31 and 37 meV, we observe the restrahlen band alluded to above, where light is completely absorbed by the TO phonons of the GaAs substrate.

Let us now compare this behavior with the magnetotransmission spectra for radiation polarized along the $[1\bar{1}0]$ direction, as seen in Fig. 2.7. The main absorption at 0 T is now found at 50 meV. This absorption decreases in energy with the magnetic field, while its intensity decreases only slightly. At around 5 T, the high energy absorption appears. Its intensity stays weak in increasing magnetic field.

We saw before that the variation in energy of these absorptions as a function of magnetic field can be predicted with the polaron model. The low energy absorption, more prevalent in Fig. 2.7, corresponds to the polaron state that results mainly from the interaction between the states $|p_-, 0\rangle$ and $|s, 1_\alpha\rangle$, labeled (1) in Fig. 2.5.

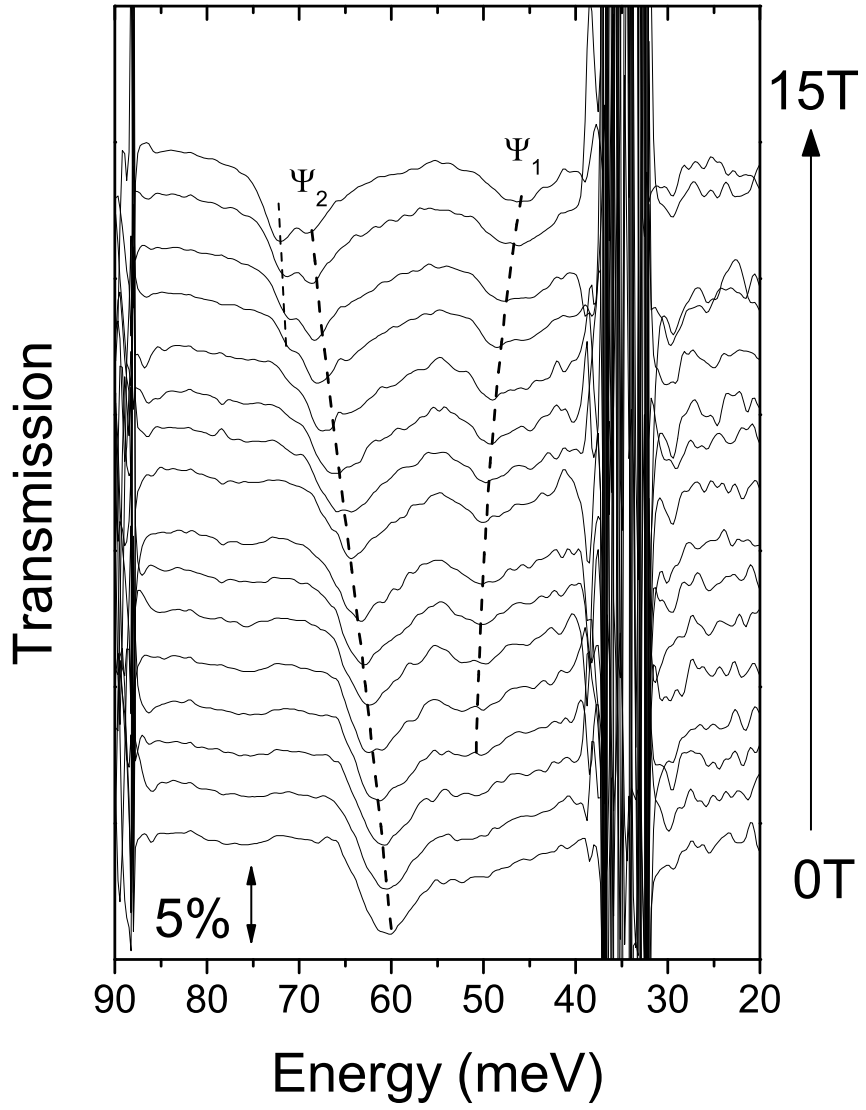

Figure 2.6: Magnetotransmission spectra measured in sample N1 for radiation linearly polarized along the [110] direction and recorded at 2 K from B = 0 to 15 T every tesla. Traces have been vertically offset for clarity.

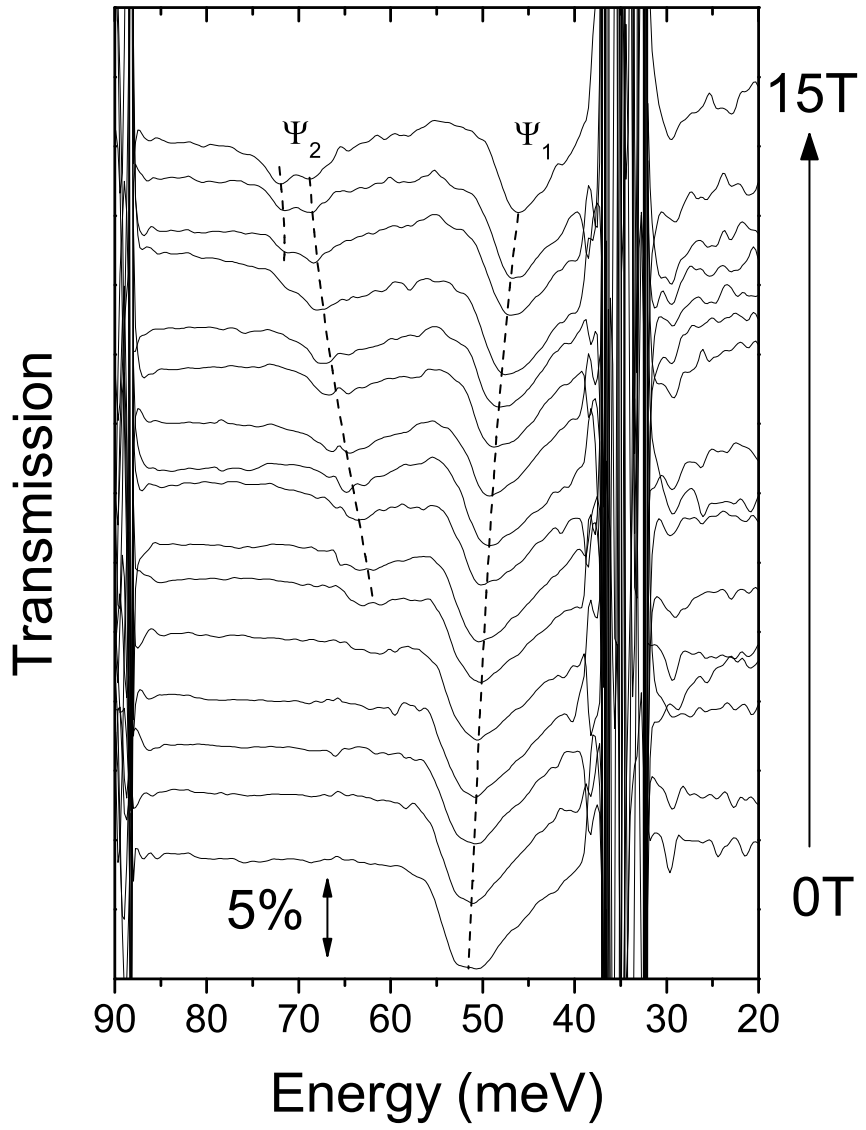

Figure 2.7: Magnetotransmission spectra measured in sample N1 for radiation linearly polarized along the $[1\bar{1}0]$ direction and recorded at 2 K from B = 0 to 15 T every tesla. Traces have been vertically offset for clarity.

On the other hand, the high energy absorption, more prevalent in Fig. 2.6, corresponds to the polaron state that results mainly from the interaction between the states $|p_+, 0\rangle$, $|p_-, 1_\beta\rangle$ and $|s, 1_\beta, 1_\alpha\rangle$, labeled (2) in Fig. 2.5. In order to explain the variation in intensity of the two main absorptions in these spectra, we will calculate their oscillator strength as a function of magnetic field.

Oscillator Strength Calculation

The optical transitions detected in our measurements involve the excitation of an electron in the QD from the ground state $|s, 0\rangle$ towards the set of five polaron states,Ψ_n. As seen in Section 1.5.3, the oscillator strength (OS) of these intraband transitions is proportional to the matrix element:

$$OS_{\Psi_n} \propto |\langle s, 0|\vec{\varepsilon}\cdot\vec{\mathbf{p}}|\Psi_n\rangle|^2 \tag{2.14}$$

The polaron wave function, in the basis presented in Fig. 2.4, is written

$$|\Psi_n\rangle = C^n_{p_+}|p_+, 0\rangle + C^n_{p_-}|p_-, 0\rangle + C^n_{s1}|s, 1_\alpha\rangle + C^n_{s2}|s, 1_\alpha, 1_\beta\rangle + C^n_{p_-1}|p_-, 1_\alpha\rangle \tag{2.15}$$

Taking into account the intraband selection rules established in Section 1.5.3 and the fact that the interaction term of Eq. 2.14 does not act on the phonon part of the wavefucntion, we find that the only allowed transitions are towards the states $|p_+, 0\rangle$ and $|p_-, 0\rangle$. The OS of a particular polaron state will therefore depend on the weight of these two optically active states, i.e. $C^n_{p_+}$ and $C^n_{p_-}$. More precisely, we find that for light polarized in the QD layer plane, Eq. 2.14 becomes

$$OS_{\Psi_n} \propto |(C^n_{p_+} + C^n_{p_-})\varepsilon_{[110]} + (C^n_{p_+} - C^n_{p_-})\varepsilon_{[1\bar{1}0]}|^2 \tag{2.16}$$

We are interested in the OS strengths of two out of the five polaron states, Ψ_1 and Ψ_2, visible in our experimental results (see Figures 2.6 and 2.7). Figure 2.8 presents the calculated OS of these two states as a function of magnetic field. The dashed curves represent the evolution of the oscillator strength of the lower energy branch (Ψ_1) whereas the solid curves represents the evolution of the higher energy branch (Ψ_2). In addition, the full circles correspond to light polarized along the [110] direction and the open circles to a polarization along the $[1\bar{1}0]$ direction.

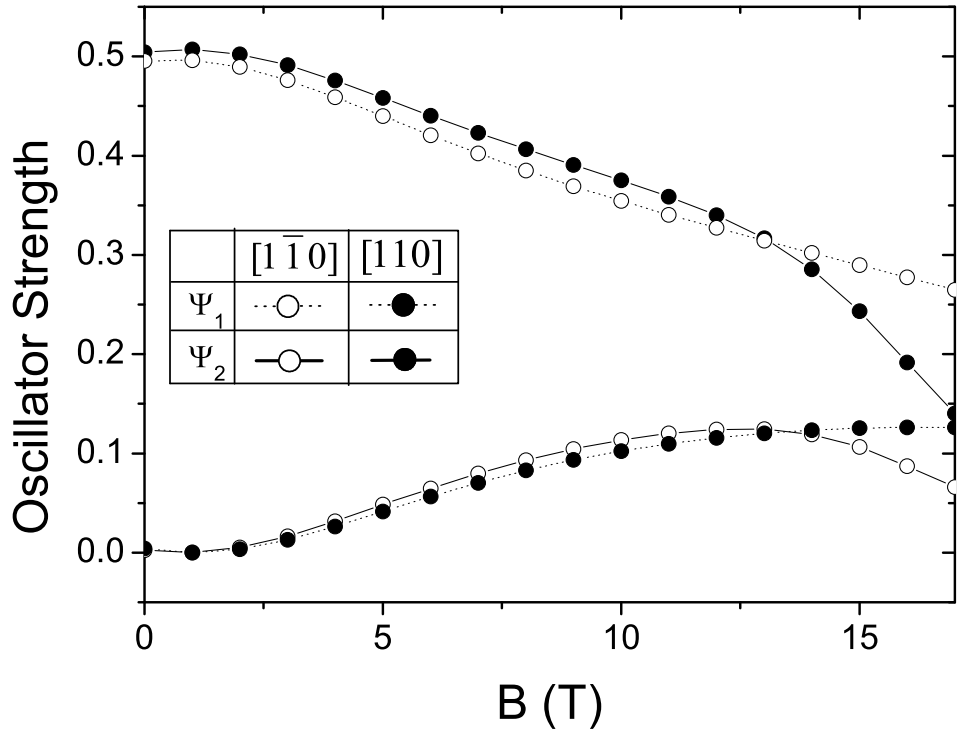

Figure 2.8: Calculated magnetic field dependence of the oscillator strength for the high energy polaron (solid lines) and the low energy polaron (dashed lines) for light polarized along the [110] (full circles) and [1$\bar{1}$0](open circles) directions.

Comparison with Experimental Results

Before comparing our results, we point out that we do not measure an OS in our experiments. More precisely, the area of the measured absorptions are equivalent to the absorption probability of the *s*-*p* resonances in the QDs, as seen in references [16], [17] and [4]. But as this probability is proportional to the OS, we will use our calculated OS to make an approximative comparison with our experimental results.

To best compare our polarization results with our calculations, we present the magnetotransmission spectra of each polarization with its corresponding OS calculation (Fig. 2.10 and Fig. 2.11). We take note that the main absorption at 0 T of both polarizations have an $\sim 7\%$ absorption, which we will associate with an OS of 0.5.¶

At low magnetic fields for both polarizations, we predict a symmetric change in the OS of the two branches: for the polarization [110] ([1$\bar{1}$0]), the OS of polaron 1 (2) increases to the detriment of the OS of polaron 2 (1). As seen in Chapter 1, the *p*-states are coupled by an anisotropy term. The exchange in OS is an effect of this coupling, which is strong for low magnetic fields (see Fig. 1.12). At high magnetic fields, the anisotropy term becomes negligible as compared to the effect of the magnetic field. Therefore, if solely the anisotropy term was taken into account (i.e. no polaron coupling), the OS of the two branches in both polarizations would eventually, with the increasing magnetic field, become equal. This is shown in Fig. 2.9, where the calculated OS of the two branches as a function of magnetic field, in absence of polaron coupling and for a polarization direction [1$\bar{1}$0], is displayed. We will show that the fact that we do not observe such a convergence in our experiments, provides further support for our polaron model.

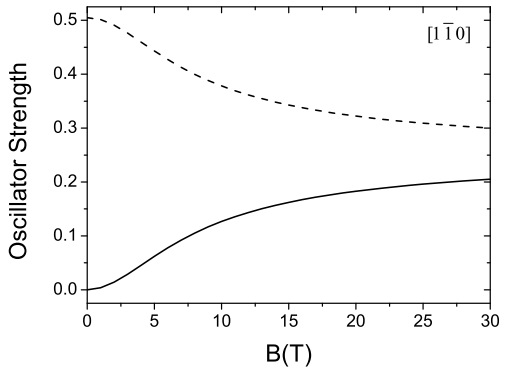

Figure 2.9: Calculated (in absence of polaron coupling) magnetic field dependence of the oscillator strength for the low energy state (dashed lines) and the high energy state (solid line) for light polarized along the [1$\bar{1}$0] direction.

¶As the FWHM of the absorptions does not significantly change with the magnetic field, we compare here the OS with the intensity and not the area of the absorptions.

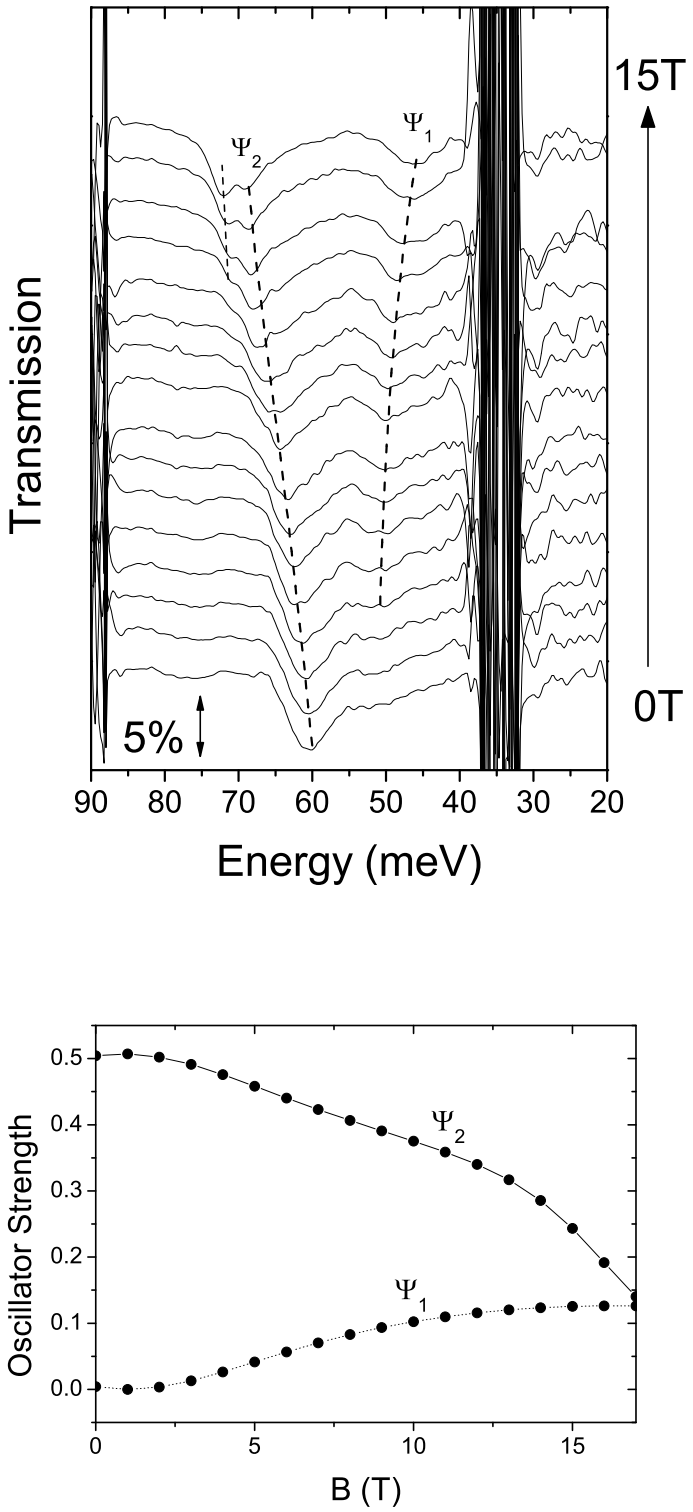

Figure 2.10: Comparison of the magnetotransmission spectra with the calculated OS for light polarized along the [110] direction.

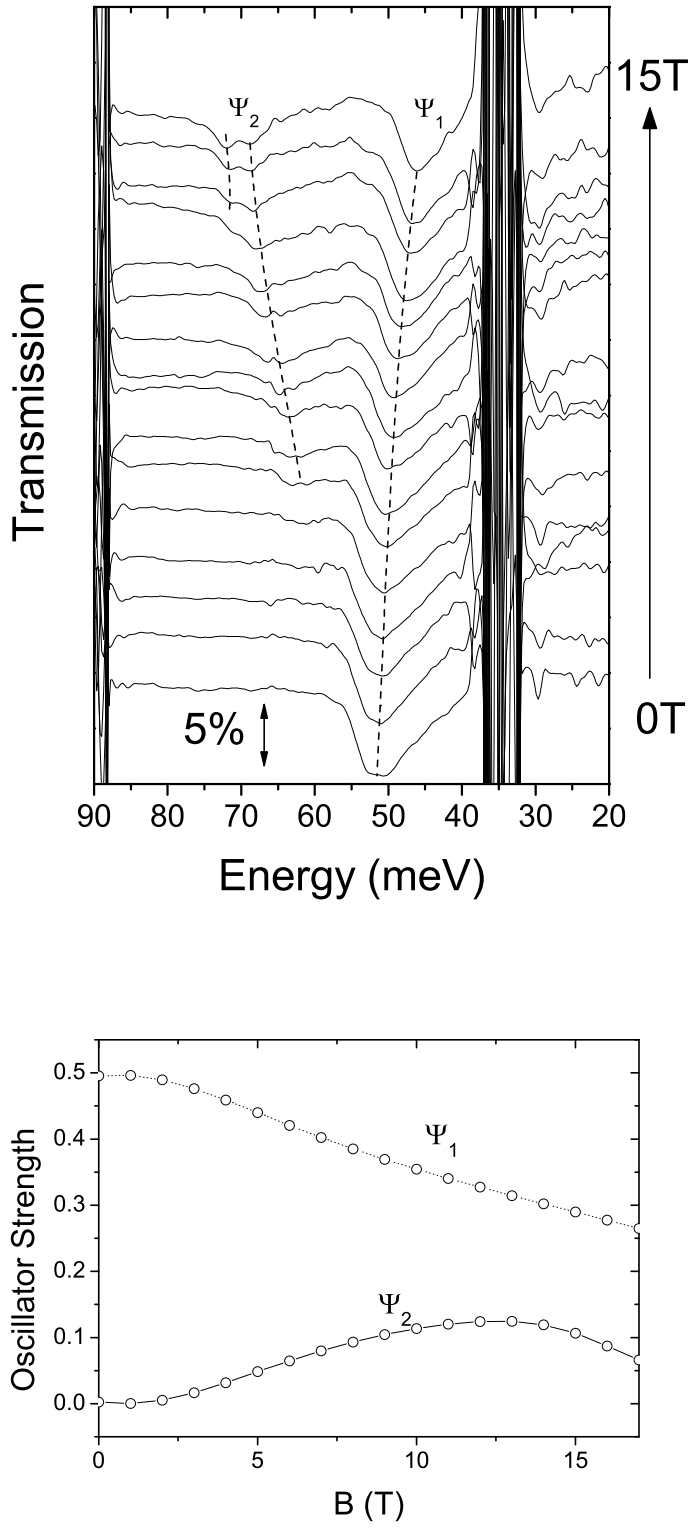

Figure 2.11: Comparison of the magnetotransmission spectra with the calculated OS for light polarized along the $[1\bar{1}0]$.

We will first comment on the OS of the high energy branch (Ψ_2). We notice in the experimental results for both polarization, that the OS of this branch is weak at 15 T; absorption $\sim 3\%$ for [110] and absorption $\sim 1.5\%$ for $[1\bar{1}0]$. In our calculations, we are able to predict this diminution in OS at high magnetic fields. For [110], the OS starts strong and quickly decreases in magnetic field. On the other hand, for $[1\bar{1}0]$, the OS increases slowly, only to peak at ~ 11 T before decreasing. The tendency of this absorption to decrease for both polarization at high magnetic fields, stems from the fact that an anti-crossing is taking place. This polaron state looses part of its OS to the advantage of a higher energy polaron state that can be detected at ~ 12 T.

This behavior is in contrast with that of the lower energy branch. At 15 T, the polaron state Ψ_1 has an absorption of $\sim 2.5\%$ for [110], whereas for the $[1\bar{1}0]$ polarization a strong absorption of $\sim 6\%$ is observed. As the anti-crossing for this branch does not take place until higher magnetic fields, we do not observe the same decrease in OS in high magnetic field as we did for the polaron state Ψ_2. The variation in the OS therefore originates, for the most part, from the anisotropy of the p-states.

We see that by using the calculated intraband OS, we are able to predict the general behavior of the variation as a function of magnetic field of the transmission absorption intensities. A deviation from a model taking into account only an anisotropy term is observed, most notable for the upper energy branch. This gives us additional evidence of the validity of our polaron model.

2.3 Conclusion

In this chapter, we began by demonstrating that a carrier confined in a QD is strongly coupled to the LO phonons of the semiconductor lattice. New states, called polaron states, form as a result of this interaction.

We then presented previously obtained results that compare the polaron model with FIR transmission experiments performed on n-doped samples in high magnetic fields. The good agreement between the model and the experimental results, evidenced the existence of these polaron states.

Finally, we presented magnetotransmission results in polarization and compared them to the calculated OS of the polaron states. The magnetic field dependent behavior of the absorption intensities was predicted with the polaron model. The effect of the anti-crossing of the polaron states was most notably observed in the high energy polaron state (2), where a weak absorption was observed in high magnetic fields for both polarizations.

The polarization experiments, along with providing complementary prove of the existence of electronic polarons, were important in testing the new magnetic polarization experimental set-up put in place during this thesis. We will see, in the next chapter, that the ability to simultaneously apply a magnetic field and polarize light in our experiments is crucial to the study of hole polarons.

Bibliography

[1] S. Hameau, J.N. Isaia, Y. Guldner, E. Deleporte, O. Verzelen, R. Ferreira, G. Bastard, J. Zeman, and J.M. Gérard, *Far-infrared magnetospectroscopy of polaron states in self-assembled InAs/GaAs quantum dots*, Phys. Rev. B **65**, 085316 (2002).

[2] D. Sarkar, H.P. van der Meulen, J.M. Calleja, J.M. Becker, R.J. Haug, and K. Pierz, *Phonons in InAs/AlAs single quantum dots observed by optical emission*, Phys. Rev. B **71**, 081302(R) (2005).

[3] P.A. Knipp, T.L. Reinecke, A. Lorke, M. Fricke, and P.M. Petroff, *Coupling between LO phonons and electronic excitations of quantum dots*, Phys. Rev. B **56**, 1516 (1997).

[4] S. Hameau, Y. Guldner, O. Verzelen, R. Ferreira, G. Bastard, J. Zeman, A. Lemaître, and J.M. Gérard, *Strong Electron-Phonon Coupling Regime in Quantum Dots: Evidence for Everlasting Resonant Polarons*, Phys. Rev. Lett. **83**, 4152 (1999).

[5] O. Verzelen, R. Ferreira, and G. Bastard, *Polaron lifetime and energy relaxation in semiconductor quantum dots*, Phys. Rev. B **62**, R4809 (2000).

[6] T. Inoshita and H. Sakaki, *Density of states and phonon-induced relaxation of electrons in semiconductor quantum dots* Phys. Rev. B **56**, R4355 (1997).

[7] X.Q. Li and Y. Arakawa, *Anharmonic decay of confined optical phonons in quantum dots* Phys. Rev. B **57**, 12285 (1998).

[8] J.N. Isaia, Ph.D. thesis, *Niveaux électronique et interaction électron-phonons dans les boîtes quantiques d'InAs/GaAs*, Université Paris VI (2002).

[9] S. Hameau, Ph.D. thesis, *Systèmes d'électrons dans les nanostructures semiconductrices à confinement quantique dans 2 ou 3 directions*, Université Paris VI (2000).

[10] O. Verzelen, Ph.D. thesis, *Interaction électron-phonon LO dans les boites quantiques d'InAs/GaAs*, Université Paris VI (2002).

[11] P. Yu, and M. Cardona, *Fundamentals of Semiconductors* Springer-Verlag, (1999).

[12] M. Levinshtien, S. Rumyantsev, and M. Shur, ed., *Semiconductor Parameters: Volume 1*, World Scientific (1996).

[13] C. Cohen-Tannoudji, B. Diu, and F. Laloë, *Mécanique Quantique* (Hermann, 1973).

[14] C. Cohen-Tannoudji, J. Dupont-Roc, and G. Grynberg, *Processus d'interaction entre photons et atomes*, (Editions du CNRS, 1996).

[15] D. Strauch and B. Dorner, *Phonon dispersion in GaAs*, J. Phys.: Condens. Matter **2**, 1457 (1990).

[16] A. Vasanelli, Ph.D. thesis, *Transitions optiques interbandes et intrabandes dans les boîtes quantiques simples et couplées verticalement*, Université Paris VI (2002).

[17] A. Vasanelli, M. De Giorgi, R. Ferreira, R. Cingolani, and G. Bastard, *Energy levels and far-infrared absorption of multi-stacked dots*, Physica E **11**, 41 (2001).

Chapter 3

Hole-LO Phonon Interaction

In this chapter, the hole excitations of p-doped self-assembled dots are studied. We will see that the experimental demonstration of a hole LO-phonon interaction presents certain challenges as compared to the electron LO-phonon interaction, seen in the previous chapter. Factors unique to p-doped samples, such as the confined energies of holes, which are found below the restrahlen band, the heavy mass of a hole, and the Be impurities levels, complicate the study. In the first section, the FIR magnetotransmission experiments of two p-doped samples are presented. The calculation of hole polaron states is then described. The comparison between these calculations and the experimental results is presented, where we will see the importance of the polarization parameter of our experiments. Finally, results from the High Magnetic Field Laboratory in Grenoble are presented to further support the evidence of the existence of hole polaron states.

3.1 Experimental Results

3.1.1 Study at 0 T

As mentioned in Chapter 1, intraband transitions in InAs/GaAs self-assembled QDs usually display anisotropic behavior when the FIR radiation is polarized along either the [110] or the [1$\bar{1}$0] direction [1, 2]. We have therefore performed magnetotransmission spectra for FIR radiation, linearly polarized along the [110] and [1$\bar{1}$0] directions of the sample. Figure 3.1 displays the FIR absorption spectra at zero magnetic field recorded for the two polarization directions in sample P1 [Fig. 3.1(a)] and sample P2 [Fig. 3.1(b)]. A main absorption is observed at an energy of $\sim$ 26 meV in both samples for the [110] polarization. For the [1$\bar{1}$0] polarization, the main absorption occurs at a slightly lower energy. The anisotropy related energy splitting is found to be $\sim$ 1.2 meV in sample P1 and $\sim$ 0.8 meV in sample P2. The sharpness of the lines [the full width at half maximum (FWHM) is $\sim$ 3 meV] is good evidence of the high quality of these samples. The main line intensity is $\sim$ 2% for sample P1 and $\sim$ 4% for sample P2. Such a difference in intensity can be explained by the different doping levels of the two samples, as described in the Appendix of reference [2].

Note, as well, that a smaller absorption is observed in both samples and for both polarizations at around 29 meV (indicated by the arrows in Fig. 3.1). We have verified

that this absorption is also measured in undoped samples grown in similar conditions, while the other absorptions associated with the doped dots are not observed. In addition, when a magnetic field is applied, we find that the absorption stays constant in energy. We thus associate this $\sim 1\%$ sharp absorption with the InAs phonon. This absorption is understandably smaller than the GaAs phonon associated absorption as a sample of self-assembled InAs/GaAs QDs contains much more GaAs (substrate plus spacers) than InAs (wetting layers plus dots).

Finally, we note the sharp features observed between 21 and 22.5 meV in both samples for both polarizations. We will see, with the application of a magnetic field, that these small absorptions can be associated with the Be impurity levels present in our p-doped samples.

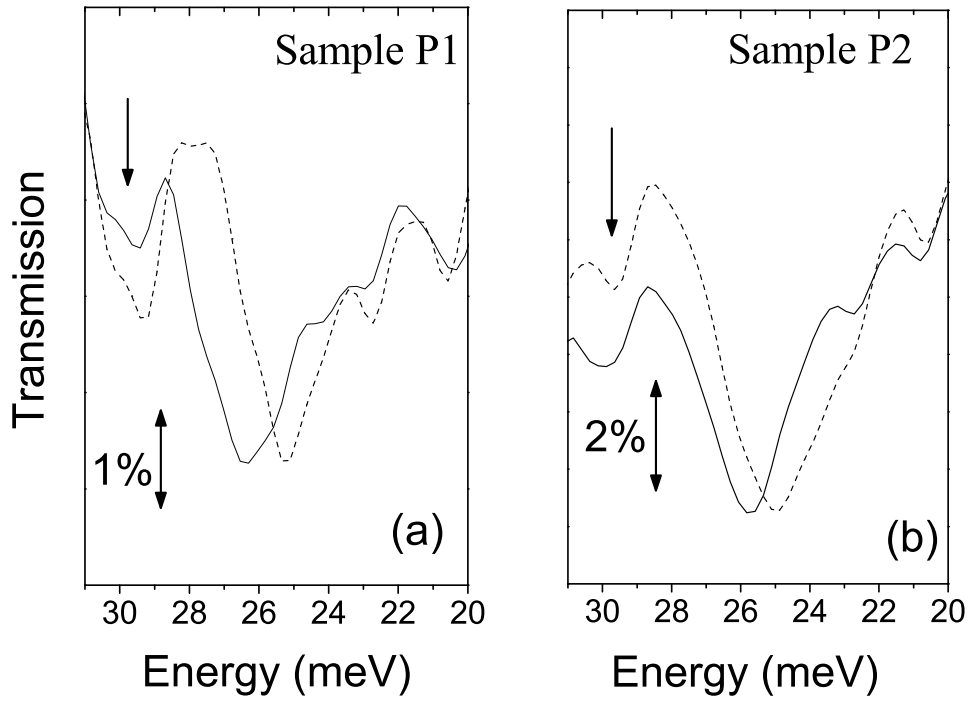

Figure 3.1: Transmission spectra at B = 0 T for radiation linearly polarized along the [110] (solid curve) and the $[1\bar{1}0]$ (dashed curve) directions for sample P1 (a) and sample P2 (b). The arrows indicate the absorption associated with the phonon of InAs.

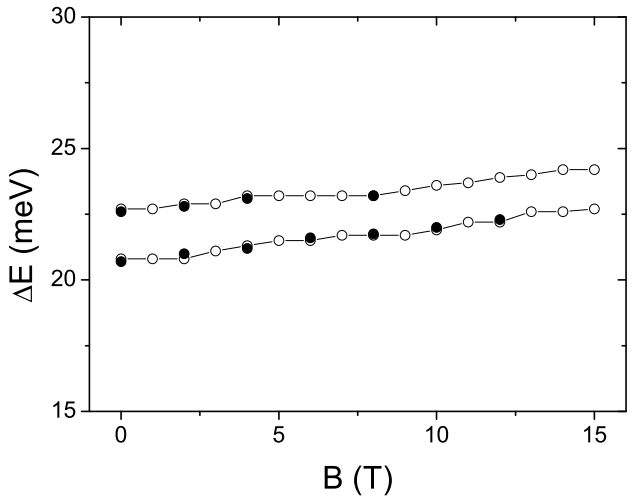

Figure 3.2: In open symbols, the sharp magnetic resonances measured in our two p-doped samples, P1 and P2. In solid symbols, FIR absorption measurements of the Be acceptor levels in bulk GaAs from reference [3].

3.1.2 Be Impurities

Proof that the low energy features in Fig. 3.1 are indeed Be impurities is important to the study of hole polarons states. As the energy transitions of Be impurity levels in GaAs are on the order of 20 meV, it is important to verify that the absorptions observed at 26 meV are indeed associated with QD levels and not impurities levels. In Fig. 3.2, the resonances of the two low energy absorptions observed in Fig. 3.1 are plotted as a function of magnetic field in open symbols. On the same figure, in solid symbols, we have plotted results found in reference [3], in which FIR absorption measurements of the Be acceptor levels in bulk GaAs were studied in a magnetic field. We find that the sharp absorptions observed in our measurements correspond exactly to the impurities levels measured in bulk GaAs. The impurities now accounted for, we can conclude that the strong absorptions observed at 26 meV in our samples are indeed absorptions related to holes trapped in the QDs of our sample.

We point out that we observe simultaneously absorptions associated with holes in QDs and with holes in Be impurity levels. This is an indicator that the transfer of holes, from the doping level 2 nm under the dot layer (see Fig. 1.4), to the QDs is not 100% efficient. We explain this by the fact that a perfect δ-doping is difficult to accomplish for light elements such as Be. On the contrary, the Be migrates throughout the GaAs spacer layer. A transfer of holes into the QDs is possible for Be found close to the dot layers, while for Be far from the layers a transfer is not possible. We therefore find bulk like impurity levels that correspond to these untransferred holes.

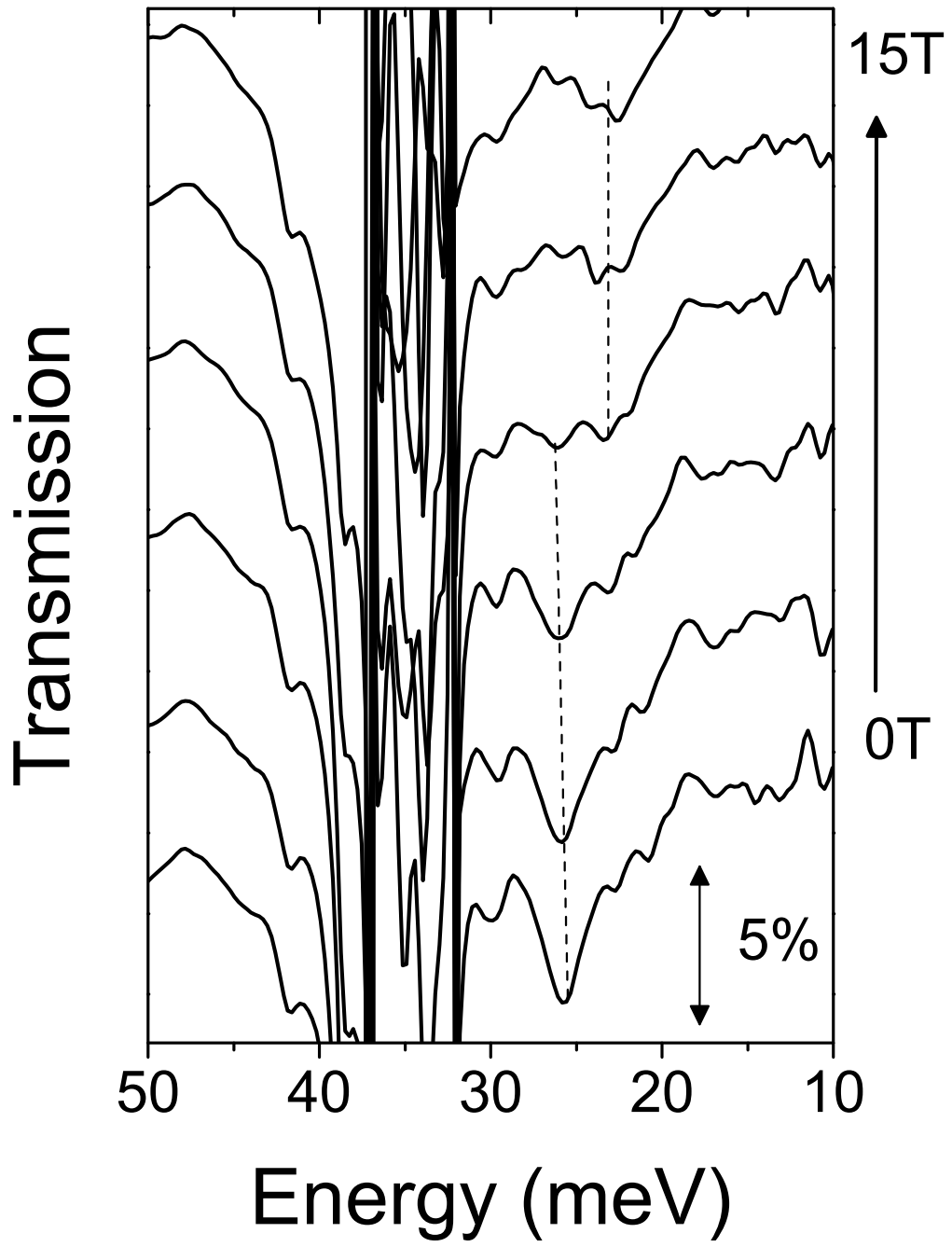

Figure 3.3: Magnetotransmission spectra measured in sample P2 for radiation linearly polarized along the [110] direction and recorded at 2 K from B = 0 to 15 T every 3 T. Traces have been vertically offset for clarity.

3.1.3 Magnetotransmission Spectra

Figure 3.3 displays the magnetotransmission spectra for radiation along the [110] direction of sample P2 and recorded at 2 K from B = 0 to 15 T every 3 T. As the magnetic field increases, the main absorption observed at zero magnetic field at ~ 26 meV stays nearly constant in energy all the while decreasing in intensity. At around 6 T, a second lower energy absorption appears at 23 meV. This second absorption decreases in energy as the magnetic field is increased. The zero transmission region from 31 to 37 meV corresponds to the restrahlen band of the GaAs substrate.

Let us now compare this behavior with the magnetotransmission spectra for radiation polarized along the $[1\bar{1}0]$ direction. Fig. 3.4 displays the magnetotransmission spectra for radiation polarized along the $[1\bar{1}0]$ direction with an applied magnetic field. The absorption minimum decreases in energy as the magnetic field increases while its intensity stays strong for all magnetic fields.

The different behavior between these two polarizations is clearly demonstrated in Fig. 3.5(a), where we have plotted the energy absorption minima of the two polarizations as a function of magnetic field. We see that one polarization contains one unique absorption that decreases in energy while the other polarization has two absorptions: a high energy branch observable at low magnetic field and low energy branch observable at high magnetic fields. We observe quite similar magnetotransmission results for sample P1, as seen in Fig. 3.5(b).

In the magnetotransmission results for p-doped samples, we remark that we do not observe the signature anti-crossings of a strong coupling situation, as we did for the n-doped samples. Nonetheless, it is clear that the transition energies observed experimentally cannot be accounted for by a simple Zeeman splitting effect that we would expect in a purely electronic, non-interacting model. Indeed, the lower and upper branches would be symmetric in that case with similar oscillator strengths. We will show that because of the respective energies of the phonon and confined hole states, no observable anti-crossings take place. In the case of holes trapped in QDs, it is therefore the oscillator strength of the transitions along with the asymmetry of the transition evolution in a B field that will provide the conclusive evidence of a hole LO-phonon interaction.

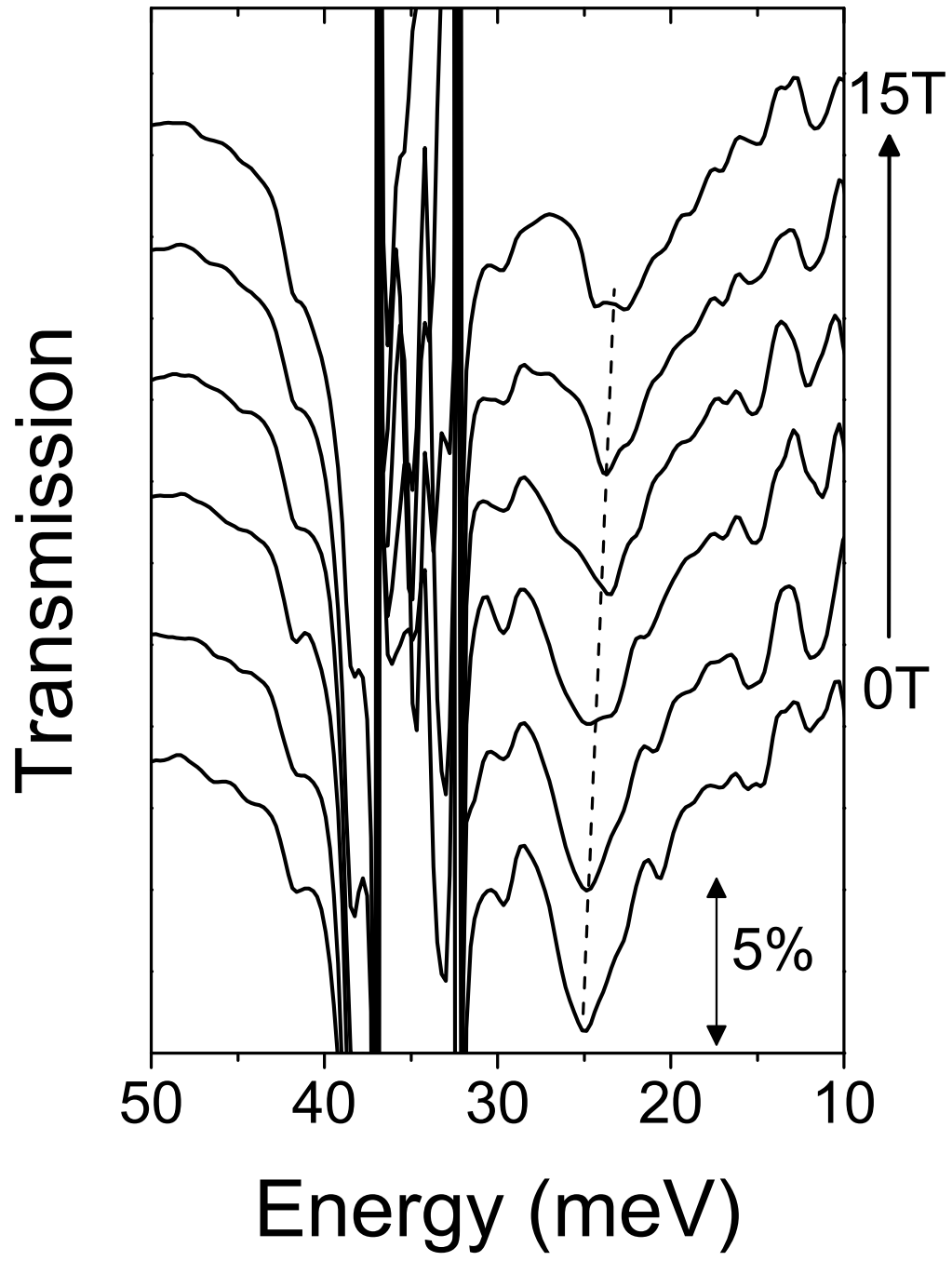

Figure 3.4: Magnetotransmission spectra measured in sample P2 for radiation linearly polarized along the $[1\bar{1}0]$ direction and recorded at 2 K from B = 0 to 15 T every 3 T.

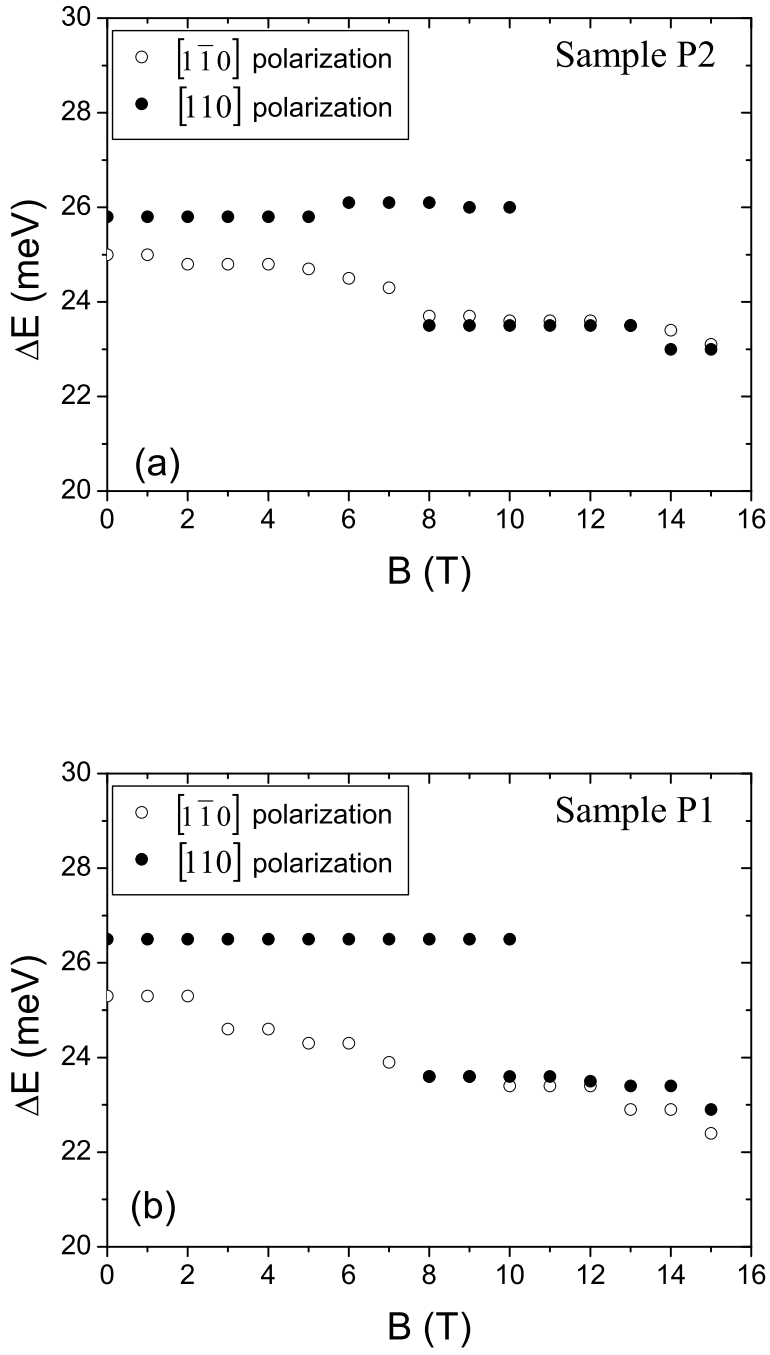

Figure 3.5: Magnetic field dispersion of the resonances in sample P2 (a) and P1 (b) for the two polarization directions; [110] in full circles and $[1\bar{1}0]$ in open circles.

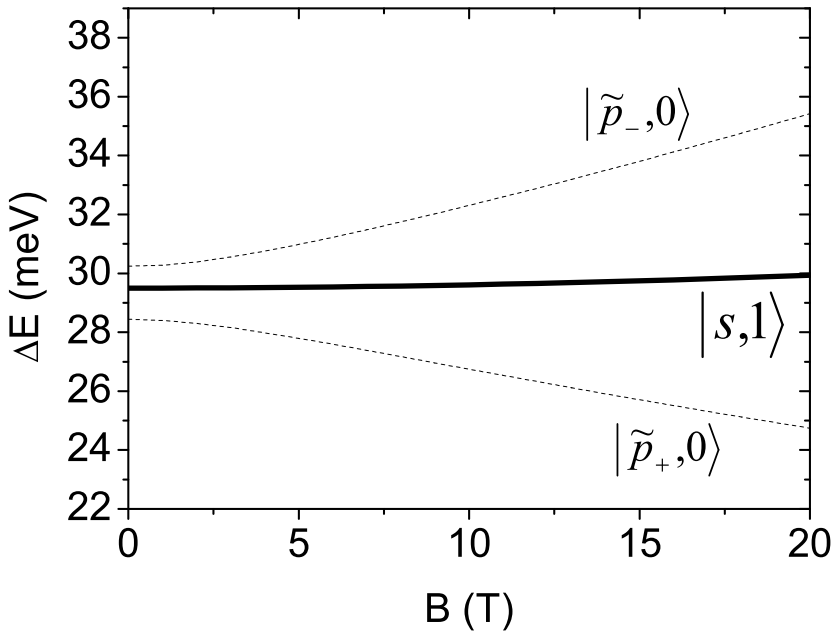

Figure 3.6: Energies versus B field of hole-phonon states in absence of the Fröhlich interaction. The energies were found using Eq. 1.16 with $m_h = 0.22m_o$, $2\delta_a = 1.8$ meV and $E_p(0) - E_s(0) = 29.3$ meV. The origin is taken at $E_s(B)$.

3.2 Hole Polaron Calculation

Analogous to the calculation of electronic polarons, we start the calculation of hole polarons by finding all the uncoupled QD states in the energy region of the experimental results, i.e. 20 - 30 meV above the ground state energy E_s. As mentioned above, a significant absorption, that is independent of the magnetic field, is observed around 29 meV in the FIR spectra of all our samples, that we attribute to the InAs phonon absorption. As confined hole states are energetically close to the InAs phonon, the contribution of the InAs phonon can not be neglected as in the case of electronic polarons. Taking this into account, we find the three states shown in Fig. 3.6, whose energies are plotted as a function of magnetic field. A dot with a height $h = 25.4$ Å and radius $R = 91$ Å was used. As shown in Section 1.5.4, because of its positive charge, the hole state $|p_h^+\rangle$ ($|p_h^-\rangle$) counterintuitively decreases (increases) in energy with an increasing magnetic field. Between these three states, we recognize two possible strong coupling situations:

- coupling between $|p_+, 0\rangle$ and $|s, 1_{\{\vec{\mathbf{q}}\}}\rangle$
- coupling between $|p_-, 0\rangle$ and $|s, 1_{\{\vec{\mathbf{q}}\}}\rangle$

In an approach similar to the one used in Chapter 2, we will divide the problem into two 2-level systems.

As demonstrated in Sections 2.1.4 and 2.2.1, the interaction between a discrete state with a dispersionless continuum of states can be simplified to the interaction between two discrete states coupled by an effective potential. In the present case, the discrete state $|p_+, 0\rangle$ is therefore coupled to the discrete state $|s, 1_\alpha\rangle$ with

$$|1_\alpha\rangle = \sum_{\vec{\mathbf{q}}} \frac{V_{sp_+}(\vec{\mathbf{q}})|1_{\vec{\mathbf{q}}}\rangle}{V_{eff}(sp_+)}. \tag{3.1}$$

Similarly, $|p_-, 0\rangle$ is coupled to the discrete state, $|s, 1_\beta\rangle$ with

$$|1_\beta\rangle = \sum_{\vec{\mathbf{q}}} \frac{V_{sp_-}(\vec{\mathbf{q}})|1_{\vec{\mathbf{q}}}\rangle}{V_{eff}(sp_-)}. \tag{3.2}$$

We notice that for each interaction, a particular phonon mode has been introduced. According to the effective potential method, the outcome of an interacting system of two discrete states ($m = 2$) and one continuum state ($M = 1$) is four [$m(M+1) = 4$] new polaron states. However, unlike the case of electrons, we do not expect to see any anti-crossings as the uncoupled states do not cross. Instead, we anticipate only a modification of the uncoupled states dispersion curves and oscillator strengths as a function of the magnetic field.

The situation is complicated by the introduction of the anisotropy term, which couples $|p_+, 0\rangle$ with $|p_-, 0\rangle$. Consequently, $|p_+, 0\rangle$ is indirectly coupled to the phonon state $|s, 1_\beta\rangle$, and at the same time $|p_-, 0\rangle$ becomes indirectly coupled to $|s, 1_\alpha\rangle$.

Finally, we will treat in perturbation the interaction between states not found in resonance with one another. We introduce the states $|p_\pm, 1\rangle$ and $|s, n\rangle$ (n = 0 or 2), that interact with the states $|p_\pm, 0\rangle$ and $|s, 1\rangle$, respectively.

Now that we have considered all the possible coupling situations (direct, indirect and in perturbation), we can proceed with the calculation of the polaron states. The polaron wave functions in our four space basis are written

$$|\Psi_n\rangle = C^n_\alpha|s, 1_\alpha\rangle + C^n_{p_+}|p_+, 0\rangle + C^n_\beta|s, 1_\beta\rangle + C^n_{p_-}|p_-, 0\rangle \tag{3.3}$$

The corresponding eigenvalue equations are

$$\begin{pmatrix} E_{s1_\alpha} - E_n & V_{eff}(sp_+) & 0 & 0 \\ V_{eff}(sp_+) & E_{p_+} - E_n & 0 & \delta_a \\ 0 & 0 & E_{s1_\beta} - E_n & V_{eff}(sp_-) \\ 0 & \delta_a & V_{eff}(sp_-) & E_{p_-} - E_n \end{pmatrix} \begin{pmatrix} C^n_\alpha \\ C^n_{p_+} \\ C^n_\beta \\ C^n_{p_-} \end{pmatrix} = 0 \tag{3.4}$$

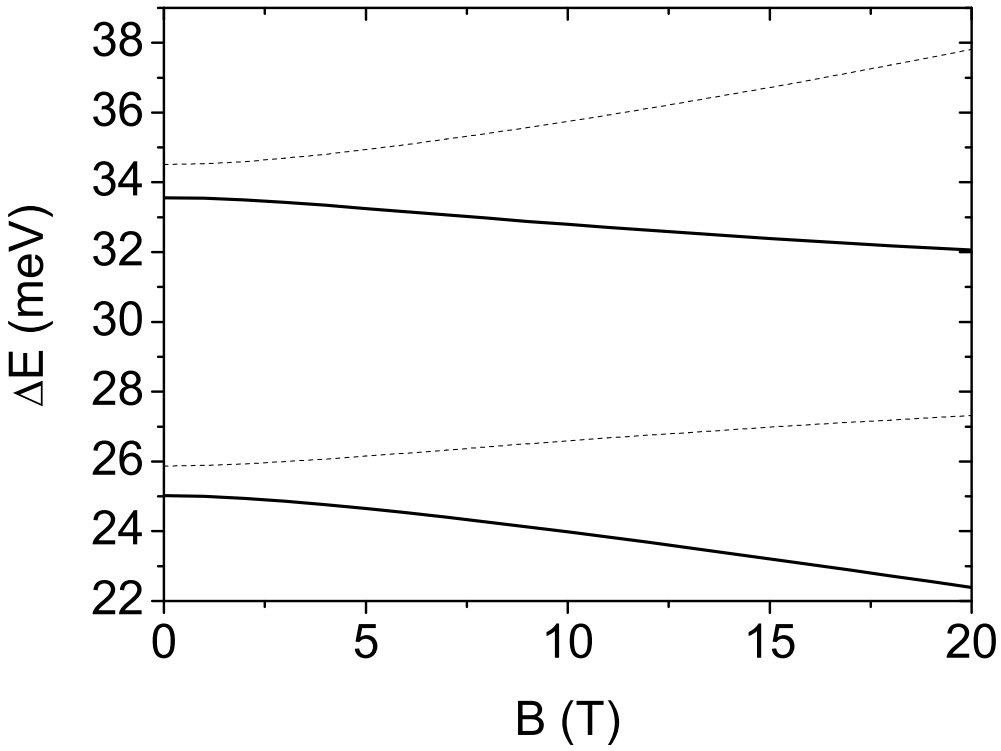

Figure 3.7: Energies versus B field of the polaron states calculated from the diagonalization of Eq. 3.4. The origin is taken at $E_s(B)$. The parameters are given in Section 3.3.

where δ_a is the anisotropy term and

$$E_{s1_{\alpha,\beta}} = E_s(B) + \hbar\omega_{LO} - \frac{\sum_{\vec{\mathbf{q}}} |V_{ss}(\vec{\mathbf{q}})|^2}{\hbar\omega_{LO}}, \tag{3.5}$$

$$E_{p_\pm 0} = E_{p_\pm 0}(B) - \frac{\sum_{\vec{\mathbf{q}}} |V_{pp}(\vec{\mathbf{q}})|^2}{\hbar\omega_{LO}}, \tag{3.6}$$

$$V_{eff}(sp_+) = V_{eff}(sp_-) = \sqrt{\sum_{\vec{\mathbf{q}}} |V_{sp_\pm}(\vec{\mathbf{q}})|^2}, \tag{3.7}$$

$E_j(B)$ is the B-dependent energy of the 0-phonon electronic level $|j\rangle$, which contains both the diamagnetic ($\sim B^2$) and Zeeman ($\sim B$) terms. The last term in E is the second order perturbation correction resulting from the interaction of $|s,0\rangle$ and $|s,2\rangle$ with $|s,1\rangle$ and $|p\pm,0\rangle$ with $|p\pm,1\rangle$. The two coupling terms, $V_{eff}(sp_+)$ and $V_{eff}(sp_-)$, were calculated and found to be 4.26 meV. The numerical diagonalization of Eq. 3.4 gives us the four polaron states presented in Fig. 3.7.

Note that a dot with cylindrical symmetry ($\delta_a = 0$) has two independent sets of polaron levels, whose field dispersions are obtained by solving

$$(E_{s1_\alpha} - E)(E_{p_+0} - E) = V_{eff}(sp_+)^2 \tag{3.8}$$

or

$$(E_{s1\beta} - E)(E_{p_-0} - E) = V_{eff}(sp_-)^2. \tag{3.9}$$

Also note that in the absence of Fröhlich coupling ($V_{eff} = 0$), Eq. 3.4 leads to two dispersion curves, $|\tilde{p}_\pm, 0\rangle$, solutions of

$$[E_{p_+0}(B) - E][E_{p_-0}(B) - E] = |\delta_a|^2 \tag{3.10}$$

which we see in Fig. 3.6 in dashed lines.

In the general case, the discrete states are at the same time coupled to each other and to the continuum states. However, since the anisotropy term is weak in our p-doped samples ($\delta_a \approx 0.9$ meV), the resulting polarons states are roughly described in terms of the coupling of $|s,1_\alpha\rangle$ with $|p_+,0\rangle$ (the two states represented in solid lines in Fig. 3.7) and $|p_-,0\rangle$ with $|s,1_\beta\rangle$ (the two states represented in dashed lines in Fig. 3.7). The parameters for this calculation are given in the next section, where we compare the experimental results with the above calculation.

3.3 Comparison Theory/Experiment

3.3.1 Comparison of Magnetic Dispersion Curves in Polarization

In Fig. 3.8, we compare our FIR magnetotransmission results, in two polarization directions and in a magnetic field up to 15 T, with our calculations. The size of the QD, the mass of the heavy hole and the Fröhlich constant of InAs were taken as adjustable parameters to best fit our data. A dot with a height $h = 25.4$ Å and radius $R = 91$ Å was used. The mass of the in-plane heavy hole in a QD was found to be $m_h = 0.22m_0$, which is similar to values found in recent theoretically and experimental studies [4, 5].

We find a Fröhlich constant $\alpha_F = 0.07$ ($A_F = 0.00186$ meV·m^{-1}), which is $\sim 30\%$ larger than that of bulk InAs.* An increase in the Fröhlich constant has been predicted theoretically for quantum dot systems [8], and observed for electronic polarons in QDs [2, 7, 9].

The energy positions versus field are very well described by our model. The two higher energy polarons branches, predicted in Fig. 3.8, are not observed experimentally in this field range because their energies coincide with that of the restrahlen band of the GaAs substrate, (grey area in Fig. 3.8).

As noted earlier, we do not observe an anti-crossing, which is the signature evidence of a strong coupling regime. Instead, the results in the two polarization directions permit the observation of the disappearance and appearance of certain absorptions. In order to explain the variation in intensity we observe experimentally, we have calculated the oscillator strengths of the optical transitions between polaron levels as a function of magnetic field.

*See Appendix B

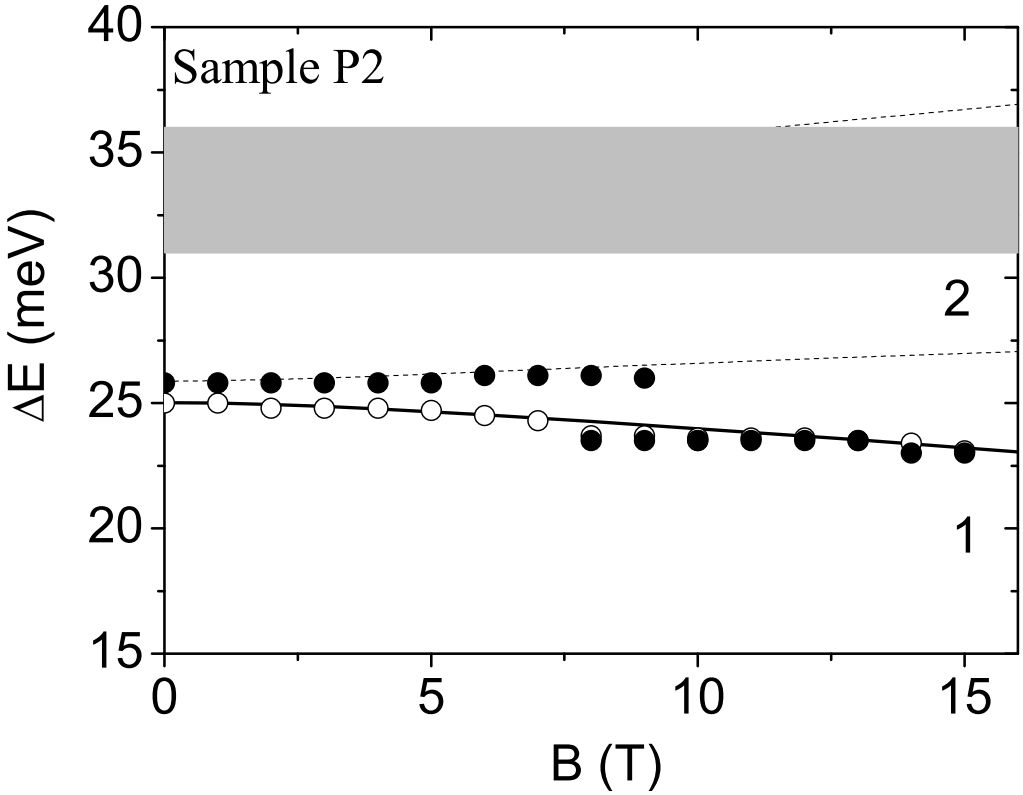

Figure 3.8: Magnetic field dispersion of the resonances observed for sample P2 for the two polarization directions; [110] in full circles and [1$\bar{1}$0] in open circles, with the calculated energy transitions in bold and dashed curves. The grey area between 31 and 36 meV represented the zero transmission region of the substrate.

3.3.2 Oscillator Strength

The optical absorptions detected in our measurements involve the excitation of the hole in the quantum dot from the ground state $|s,0\rangle$, towards the set of four polaron levels $|\Psi_n\rangle$ resulting from the diagonalization of the 4×4 matrix in Eq. 3.4. Similar to the OS formula for electronic polarons (Eq. 2.14), we find for a hole and for light polarized in the QD layer plane, an oscillator strength for each transition proportional to

$$OS_{\Psi_n} \propto |(C^n_{p_+} + C^n_{p_-})\epsilon_{[110]} + (C^n_{p_+} - C^n_{p_-})\epsilon_{[1\bar{1}0]}|^2, \tag{3.11}$$

where ϵ is the in-plane polarization direction of the electromagnetic wave. We show in Fig. 3.9 the field dependence of the oscillator strength for the two low-lying polaron levels for both [110] [Fig. 3.9(a)] and $[1\bar{1}0]$ [Fig. 3.9(b)] polarizations.

The solid curves represent the evolution of the oscillator strength of the lower energy branch [labeled (1) in Fig. 3.8], whereas the dashed curves represents the evolution of the higher energy branch [labeled (2) in Fig. 3.8]. Note that, at zero magnetic field, the $\sim 4\%$ absorption measured in sample P2 for light polarized along the $[1\bar{1}0]$ direction (Fig. 3.4), corresponds to an oscillator strength of ~ 0.6. This is corroborated by the $\sim 3\%$ absorption for light polarized along the [110] direction (Fig. 3.3), which corresponds to an oscillator strength of ~ 0.45. Taking into account the signal to noise ratio, which allows the detection of $\sim 1\%$ transmission variation, our experimental sensitivity corresponds roughly to an oscillator strength of ~ 0.15. At zero tesla, our model predicts the existence of the higher energy branch for the [110] polarization and the lower energy branch for the $[1\bar{1}0]$ polarization. As the magnetic field is increased, the oscillator strength of the high energy branch decreases towards the experimental limit 0.15, while the oscillator strength of the lower energy branch increases above the experimentally observable intensity at around 6 T.

For the other polarization $[1\bar{1}0]$, our model predicts one unique observable absorption with an oscillator strength that stays nearly constant with the changing magnetic field. This is a good description of the oscillator strength behavior we observe in the magnetotransmission spectra of our samples. In addition, we note that a purely electronic model cannot predict the variation in oscillator strength with the magnetic field that we observe experimentally. The good agreement obtained for the energy transitions as well as for the evolution of oscillator strengths demonstrates that the magneto-optical transitions occur between polaron states.

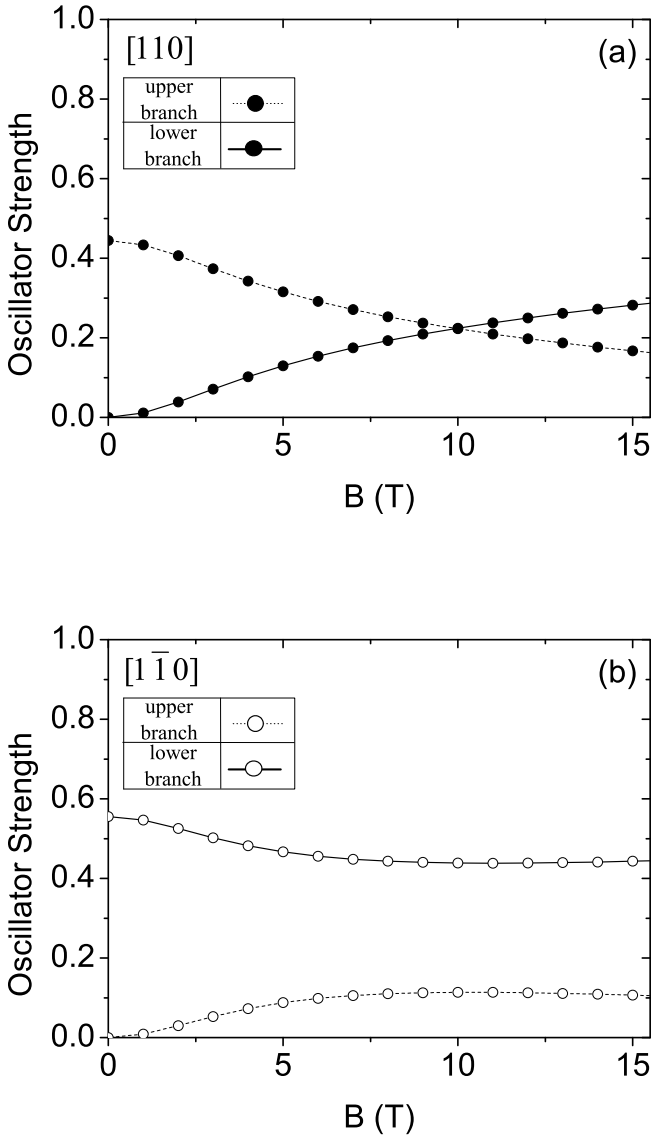

Figure 3.9: Calculated magnetic field dependence of the oscillator strength for the high energy polaron (dashed line) and the low energy polaron (solid line) for light polarized along the [110] (a) and [1$\bar{1}$0] (b) directions.

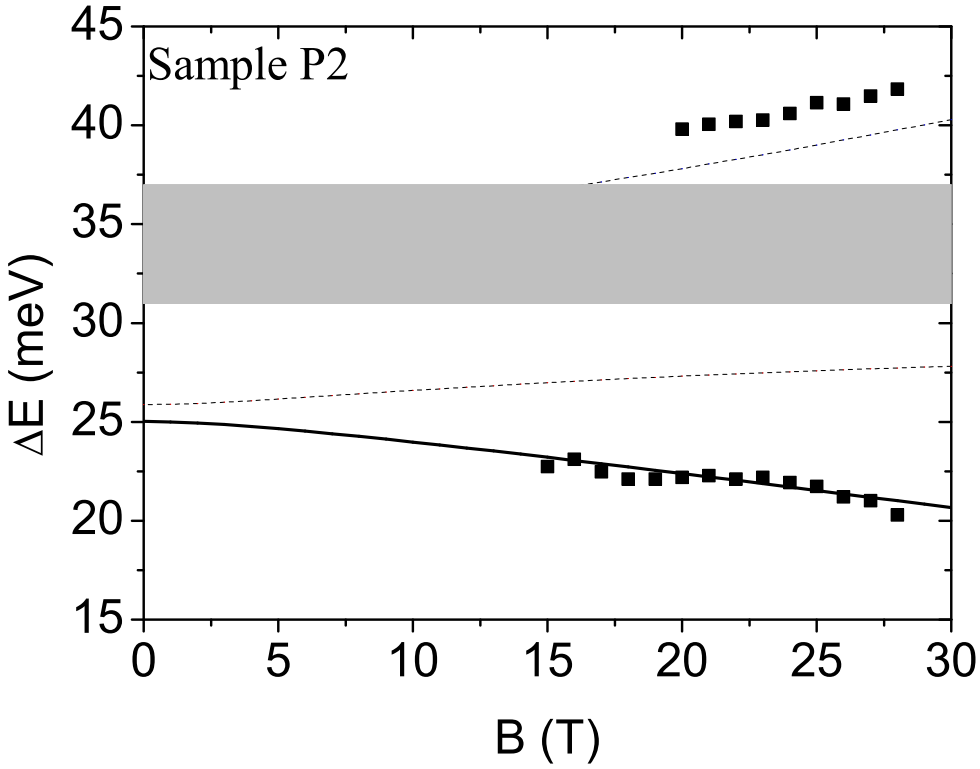

Figure 3.10: High magnetic field dispersion of the resonances (full squares) in unpolarized light for sample P2. The lines are the resonance dispersions calculated using the parameters listed in the text.

3.3.3 Comparison of Magnetic Dispersion Curves in High Fields

Finally, we present the results of magnetotransmission measurements done on sample P2 at the High Magnetic Field Laboratory in Grenoble. In Fig. 3.10, we display the magnetic field dispersion of resonances between 15 and 28 T for unpolarized radiation. The lines are the calculated dispersions using the same parameters as above, but now calculated up to B = 30 T. We observe only one branch below the restrahlen band, which is consistent with our OS strength calculation. Indeed, as branch (2) approaches the energy of the InAs phonon, its OS becomes weaker and weaker.

But the most important result from these additional high magnetic field experiments is that they have permitted us to experimentally observe the polaron transition at energies above the restrahlen band of the substrate. At 20 T, we start to see an absorption at ∼40 meV. This is a significant result because this energy transition cannot be predicted using a purely electronic model. In an uncoupled system the p branches of a hole move very little with the magnetic field (see Fig. 1.11 of Chapter 1). The $|p_-\rangle$ state will not increase enough in energy to reach our experimentally observed absorption if solely the Zeeman and diamagnetic effects are taken into account. In the polaron model, the upper branch is pushed up in energy due to the interaction with the InAs phonon. We therefore have additional experimental support that the energy transitions occur between polaron states.

Note that in Fig. 3.10 the calculated upper branch is found to be ~ 2 meV below the experimental points. Such a discrepancy could arise from an interaction involving the LO-phonon of GaAs (~ 36 meV) which is not included in our calculations, where only the InAs like LO-phonon is taken into account. It has been demonstrated that in certain mixed crystals, such as the alloy semiconductor $In_{1-x}Ga_xAs$, there are two distinct sets of optical phonons [10, 11]. As our dots are not made up of pure InAs, but are in fact a mixture GaAs and InAs, we should expect the same two phonon mode behavior.

Let's investigate the consequences of considering the two LO phonon modes: InAs and GaAs. We limit our study to a three level system involving the $|p_-, 0\rangle$ state, whose energy increases with increasing magnetic field. Due to its evolution with the magnetic field, this discrete state finds itself in proximity to the two continuum states, $|s, 1_{\{\vec{\mathbf{q}}\}}\rangle_{\mathrm{InAs}}$ and $|s, 1_{\{\vec{\mathbf{q}}\}}\rangle_{\mathrm{GaAs}}$, as seen in Fig. 3.11. We introduce two linear combination phonon states in interaction with $|p_-, 0\rangle$, where β will be used to denote the case of the InAs phonon interaction and γ the GaAs phonon interaction,

$$
\begin{aligned}
|1_\beta\rangle &= \sum_{\vec{\mathbf{q}}} \frac{V_\beta(\vec{\mathbf{q}})|1_{\vec{\mathbf{q}}}\rangle}{V_{eff}(\beta)}. \\
|1_\gamma\rangle &= \sum_{\vec{\mathbf{q}}} \frac{V_\gamma(\vec{\mathbf{q}})|1_{\vec{\mathbf{q}}}\rangle}{V_{eff}(\gamma)}.
\end{aligned}
\tag{3.12}
$$

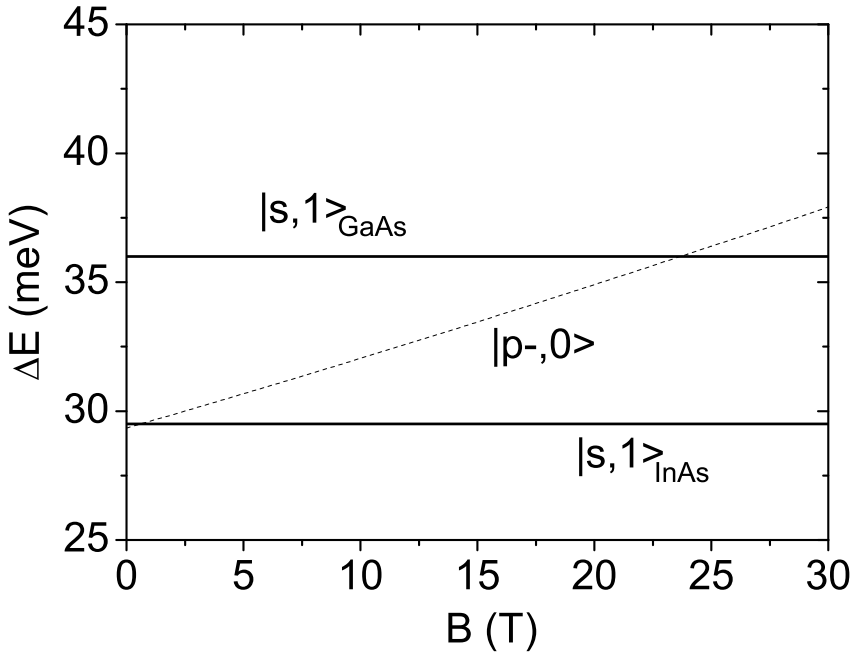

Figure 3.11: Energies versus B field of the non-interacting hole-phonon states including the GaAs LO phonon mode, for the parameters used in Fig. 3.6 and a GaAs phonon energy of 36 meV.

The Hamiltonian of this reduced system is written

$$H = \begin{pmatrix} E_s(B) + \hbar\omega_\beta & V_{eff}(\beta) & 0 \\ V_{eff}(\beta) & E_{p_-}(B) & V_{eff}(\gamma) \\ 0 & V_{eff}(\gamma) & E_s(B) + \hbar\omega_\gamma \end{pmatrix} \tag{3.13}$$

where the InAs and GaAs phonon energies are noted respectively by $\hbar\omega_\beta$ and $\hbar\omega_\gamma$. The same value for the InAs coupling term, $V_{eff}(\gamma) = 4.26$ meV, was employed and the value of $V_{eff}(\beta)$ was found to be 3.95 meV. After diagonalization of the Hamiltonian, we find three polaron states. The two high energy polaron states are displayed in Fig. 3.12, in solid lines. We compare them to the one high energy polaron branch, in dashed lines, found when taking into account solely the InAs phonon.

Firstly, we remark that the addition of the GaAs mode results in two high energy branches, where we once had one. However, one of these branches is found in the restrahlen band, and therefore cannot be observed experimentally. A second result of this calculation, is an upshift in energy of the highest energy polaron state. Therefore, by adding the GaAs phonon, with this simple three level model, we are able to demonstrate the tendency of the upper branch to be pushed higher in energy: behavior observed in our experimental results.

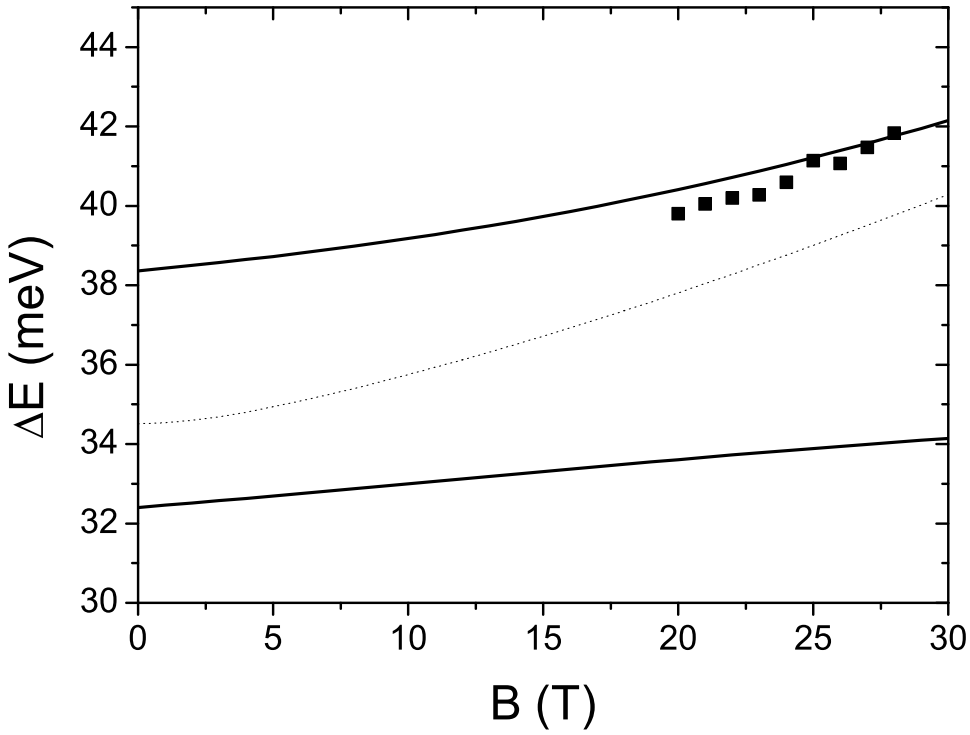

Figure 3.12: In solid lines, the two high energy polaron states resulting from a two phonon mode model (Eq. 3.13) and in dashed lines, the high energy polaron state resulting from the one phonon mode model (Eq. 3.4). The squares are the high magnetic field dispersion of the resonances in unpolarized light for sample P2.

3.4 Conclusion

In summary, we have investigated the valence intraband transitions in p-doped self-assembled InAs QDs by using FIR magneto-optical techniques with linearly polarized radiation. We have shown that a purely electronic model is unable to account for the experimental data, neither for the energy dispersion of the magneto absorption resonance, nor for the intensity dependence versus magnetic field.

As the transition energies are close to that of the LO-phonon in InAs, we have shown that a model taking into account the hole LO-phonon coupling is able to predict well the experimental data. We have calculated the coupling between the relevant mixed hole-lattice states and determined the polaron states as well the oscillator strength of the polaron transitions as a function of magnetic field.

The fact that our model successfully fits the experimental data constitutes the first evidence for the existence of hole polarons in InAs QDs and demonstrates that the intraband magneto-optical transitions occur between hole polaron states.

Bibliography

[1] V. Preisler, R. Ferreira, S. Hameau, L. A. de Vaulchier, Y. Guldner, M. L. Sadowski, and A. Lemaître, *Hole-LO phonon interaction in InAs/GaAs quantum dots*, Phys. Rev. B **72**, 115309 (2005).

[2] S. Hameau, J.N. Isaia, Y. Guldner, E. Deleporte, O. Verzelen, R. Ferreira, G. Bastard, J. Zeman, and J.M. Gérard, *Far-infrared magnetospectroscopy of polaron states in self-assembled InAs/GaAs quantum dots*, Phys. Rev. B **65**, 085316 (2002).

[3] R.A. Lewis, Y.-J. Wang, and M. Henini, *Magnetospectroscopy of Be in GaAs*, Phys. Rev. B **67**, 235204 (2003).

[4] R. J. Warburton, B. T. Miller, C. S. Dürr, C. Bödefeld, K. Karrai, J. P. Kotthaus, G. Medeiros-Ribeiro, P. M. Petroff, and S. Huant, *Coulomb interactions in small charge-tunable quantum dots: A simple model*, Phys. Rev. B **58**, 16221 (1998).

[5] D. Reuter, P. Kailuweit, A. D. Wieck, U. Zeitler, O. Wibbelhoff, C. Meier, A. Lorke, and J. C. Maan, *Coulomb-Interaction-Induced Incomplete Shell Filling in the Hole System of InAs Quantum Dots*, Phys. Rev. Lett.**94**, 026808 (2005).

[6] S. Hameau, Y. Guldner, O. Verzelen, R. Ferreira, G. Bastard, J. Zeman, A. Lemaître, and J.M. Gérard, *Strong Electron-Phonon Coupling Regime in Quantum Dots: Evidence for Everlasting Resonant Polarons*, Phys. Rev. Lett. **83**, 4152 (1999).

[7] J.N. Isaia, Ph.D. thesis, *Niveaux électronique et interaction électron-phonons dans les boîtes quantiques d'InAs/GaAs*, Université Paris VI (2002).

[8] X.Q. Li and Y. Arakawa, *Anharmonic decay of confined optical phonons in quantum dots* Phys. Rev. B **57**, 12285 (1998).

[9] R. Heitz, M. Veit, N. N. Ledentsov, A. Hoffmann, D. Bimberg, V. M. Ustinov, P. S. Kop'ev, and Zh. I. Alferov, *Energy relaxation by multiphonon processes in InAs/GaAs quantum dots* Phys. Rev. B 56, 10435 (1997).

[10] L. Swierkowski, W. Zawadski, Y. Guldner, and C. Rigaux, *Two-mode Resonant Polaron in the $Hg_{0.72}Cd_{0.28}Te$ Semiconductor*, Solid State Communications **27**, 1245 (1978).

[11] N.L. Rowell, G. Yu, D.J. Lockwood, and P.J. Poole, *Phonons in $In_{0.53}Ga_{0.47}As/InP(100)$ superlattices by infrared reflectance*, Phys. Rev. B **68**, 165320 (2003).

Chapter 4

Exciton-LO Phonon Interaction: PLE Experiments

In this chapter, the interaction between LO phonons and an electron-hole pair or exciton will be studied. The interband transitions in several ensembles of QDs are investigated by using photoluminescence excitation (PLE) under strong magnetic fields. The first section will be dedicated to the presentation of these experimental results. A study of the PLE spectra, first as a function of detection energy, then as a function of magnetic field will be presented. The second section will focus on the calculation of excitonic polaron states. Finally, it will be shown that the PLE results are in good agreement with the excitonic polaron model.

4.1 Experimental Results

4.1.1 PLE Spectroscopy

Interband transitions of a QD ensemble are inhomogeneously broadened because of fluctuations of the confining potential which arise from size and composition dispersion. In a non-resonant photoluminescence (NRPL) measurement (see Section 1.5.2), the excitation energy is fixed to be superior to the energy gap of GaAs such that all dots, regardless of their size, can be selected. The broad bell-like form of a PL peak is therefore a measure of size inhomogeneity. In Fig. 4.1, the NRPL peaks of three samples, U1, N2 and P3, are displayed. We observe, for the three different samples, a broad peak centered at ~ 1.2 eV with a FWHM of ~ 50 meV. The study of the interband transitions in QDs, therefore requires overcoming this inhomogeneous broadening of the optical spectra. This can be accomplished by using single QD spectroscopy, where the sharp spectral lines enable the study of, e.g., the fine structure of the system [1] and discrete-continuum state coupling [2]. For an ensemble of QDs, such as our samples, PLE spectroscopy serves as an important tool, as it allows for the circumvention of part of the inhomogeneous broadening.

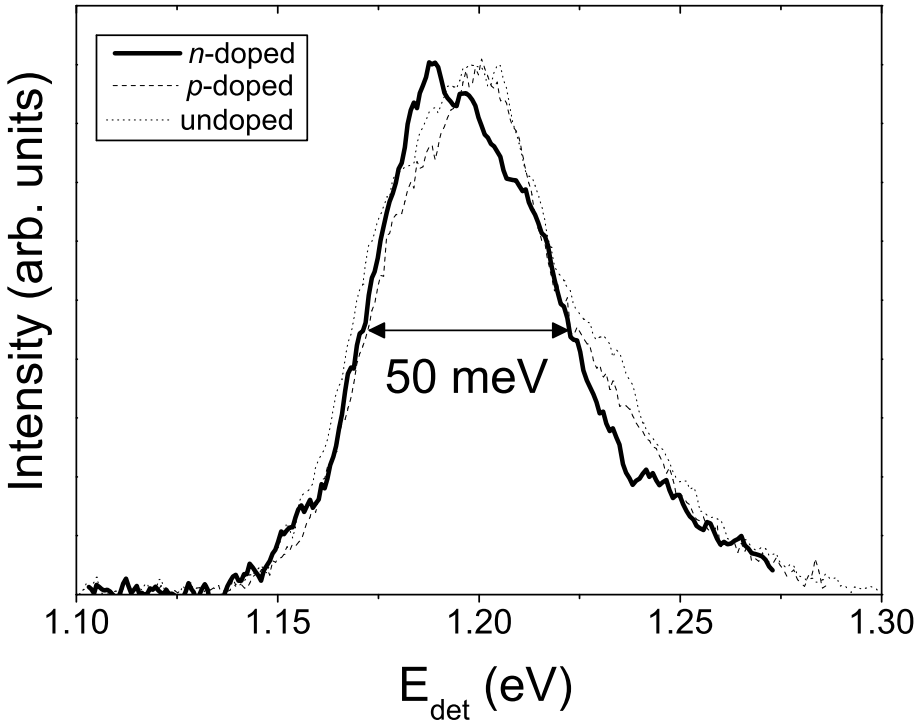

(a)

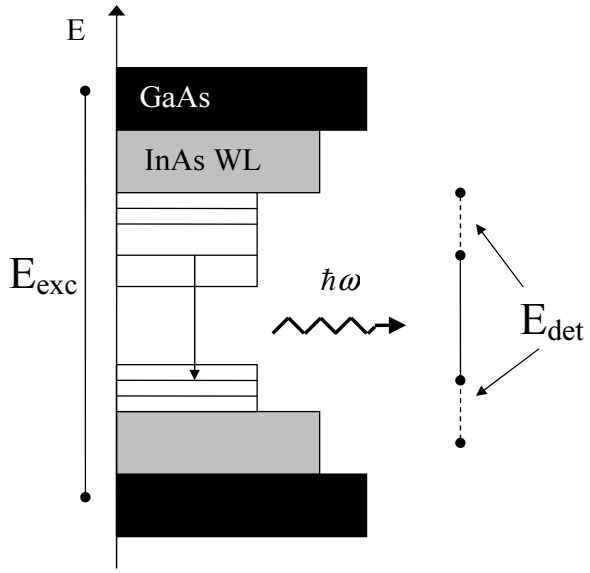

(b)

Figure 4.1: The normalized NRPL peaks for three differently doped samples excited by an Ar+ laser and recorded at 4 K (a). A schematic of the NRPL process in a QD system (b).

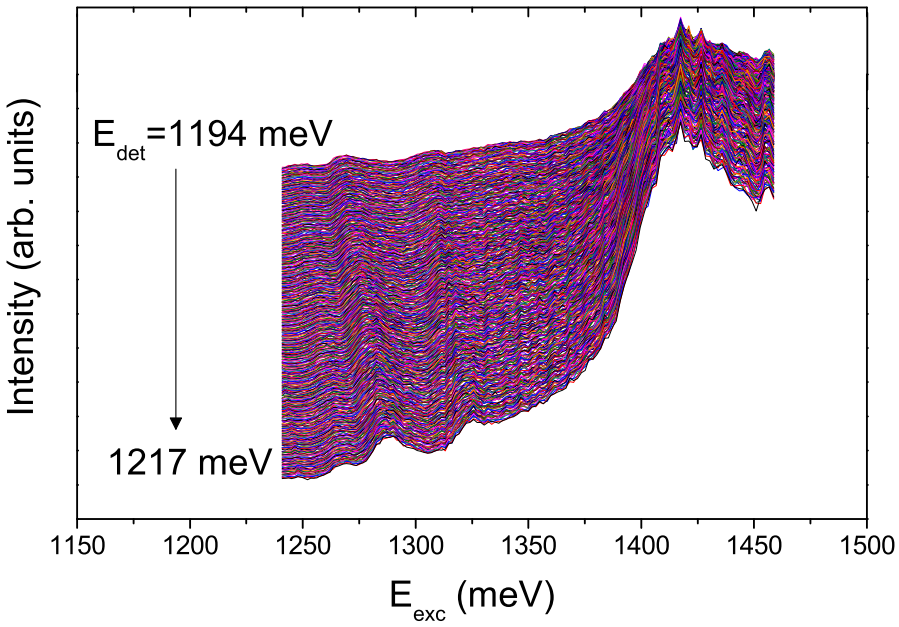

(a)

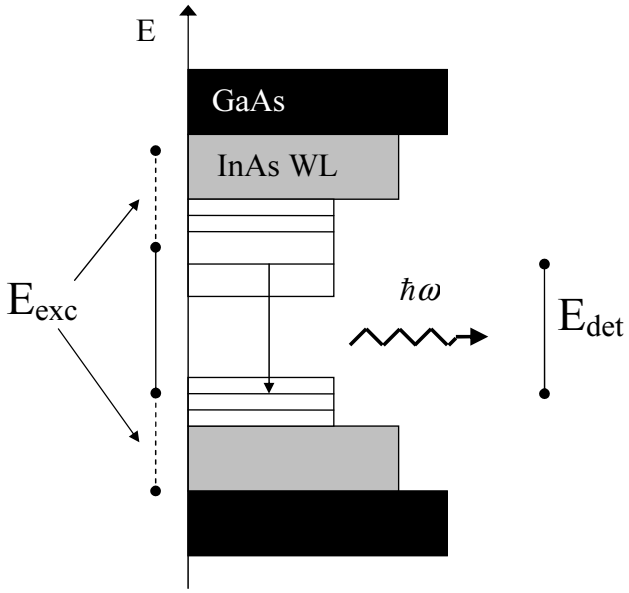

(b)

Figure 4.2: PLE spectra for different detection energies at 4 K for sample P3 (a). The spectra are vertically offset. A schematic of the PLE process in a QD system (b).

As seen in Section 1.5.2 of Chapter 1, in a PLE measurement, we fix a detection energy while the optical excitation energy is varied. For a dot to be detected, its ground state energy must be equal to the chosen detection energy [see Fig. 4.2(b)]. Only dots with the same ground state energy, and therefore similar size and composition, contribute to the PLE signal. PLE spectroscopy therefore enables the selection of a subensemble of similar sized dots, from a sample containing a range of dot sizes [3].

In Fig. 4.2, the PLE spectra for a range of detection energies is presented. The spectra were recorded at 4 K on sample P3. We take note that each spectrum corresponds to a different subensemble of QDs in our self-assembled sample. We expect to have a large population of dots with ground state energy near the peak energy of the NRPL spectra. The energy detection window, that was taken in the case of Fig. 4.2 from 1194 - 1217 meV, is therefore centered at $\sim$ 1200 meV. Using the experimental set-up described in Section 1.5.2, the acquisition time for the PLE spectra in Fig. 4.2 is approximately 350 seconds (1 second per spectrum). With this set-up, we are able to collect a wealth of data, for a reasonably short acquisition time.

Finally in Fig. 4.3, we display a zoom of the PLE spectrum for a detection energy, E_{det} = 1215 meV. We find a peak with a FWHM of $\sim$ 15 meV, which is about a third of what was found in Fig. 4.1. We conclude that although such spectra are still inhomogeneously broadened due to shape and composition variation, well-defined features are still observed, making low-temperature PLE spectroscopy an appropriate probe of the energy states of quantum dots in our study. However, for the study of the spin contribution to the QD levels, a 15 meV FWHM is still too broad, and single QD spectroscopy remains the appropriate method of investigation.*

*See Appendix A

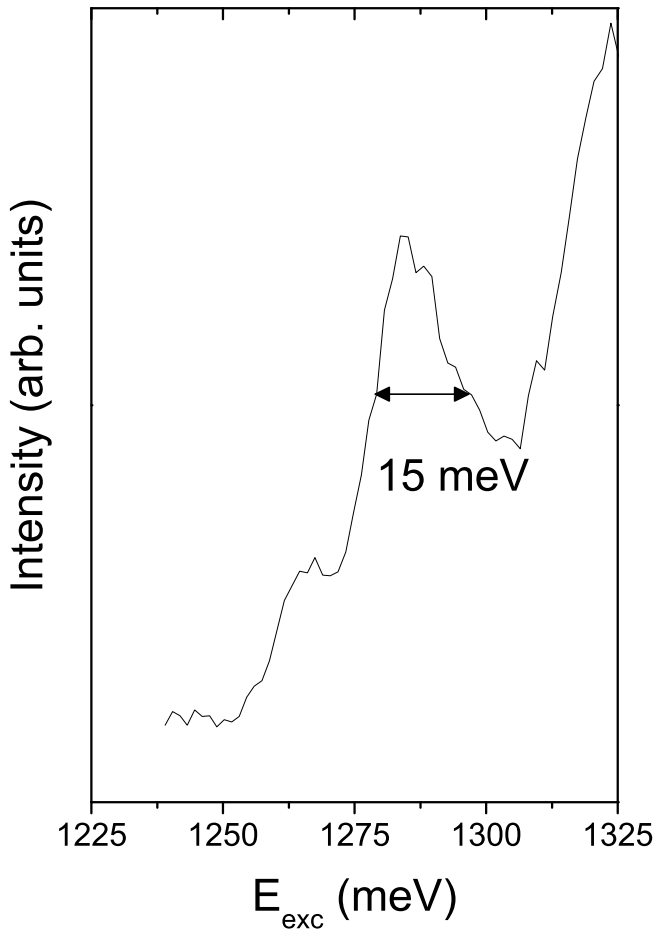

Figure 4.3: PLE spectra of sample P3 taken at 4 K for $E_{det} = 1215$ meV.

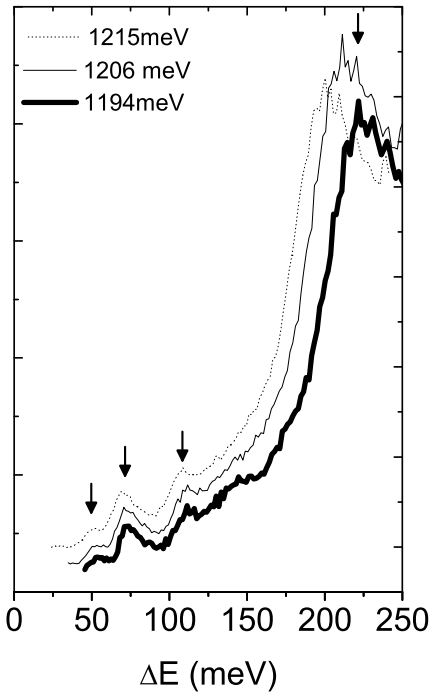

Figure 4.4: Normalized PLE spectra of sample P3 taken at 4 K for E_{det}=1194, 1206 and 1215 meV, where $\Delta E = E_{exc} - E_{det}$.

4.1.2 Study as a Function of Detection Energy

We will now take a closer look at the PLE spectra for three different detection energies. Figure 4.4 depicts the spectra of sample P3 for detection energies E_{det}=1194, 1206 and 1215 meV at 4 K. The x-axis shows the excess excitation energy $\Delta E = E_{exc} - E_{det}$. The same four features, indicated by arrows in Fig. 4.4, are observed for all three detection energies. A low-energy peak is observed at ∼50 meV, a second peak is found at ∼75 meV, a third peak is found at ∼110 meV and finally a strong peak is observed at ∼220 meV.

We attribute this last high-energy peak to the excitation resonance of the wetting layer (WL). The energy, ΔE, of this peak decreases as the detection energy is increased, however the transition energy, $\Delta E + E_{det}(=E_{exc})$, stays at the nearly constant energy of ∼1420 meV. Such an energy is typical given the growth conditions used for our samples and corresponds to few monolayer thick InAs WL [4].

The remaining three peaks, found at lower energies, are associated with transitions between bound levels in the QDs. As reported in Section 1.4.2, the ground and first excited state in both the conduction and valence band are s- and p-like respectively. In order to associate the excitation peaks with transitions in the QDs, a magnetic field B is applied along the sample's growth axis, as the effect of a magnetic field is different for s and p states (see Eq. 1.15).

4.1.3 Study as a Function of Magnetic Field

Figure 4.5 displays the magneto-PLE spectra of sample P3 recorded at 4 K from $B = 0$ to 28 T every 4 T and for a detection energy of 1215 meV. Similar results were observed for the undoped sample U1 and the n-doped sample N2, as shown in Fig. 4.6 where their magneto-PLE spectra are depicted on a magnified scale.

The energy of the PLE peaks as a function of magnetic field is plotted in Fig. 4.7 for sample P3. For all three samples, as the magnetic field increases, the peak that was initially at ∼75 meV splits into two separate peaks: one peak that increases in energy and a second peak that decreases in energy. These peaks can be associated with p-like transitions. This association is made because firstly the peaks move with the magnetic field, which is characteristic of p-states, and secondly the energy at 0 T of these peaks roughly corresponds to the addition of the experimentally obtained s-p energy transitions of holes and electrons. The remaining two peaks at ∼50 and ∼110 meV stay nearly constant with the the increasing magnetic field. We therefore associate these peaks with transitions involving states whose energies move very little with an applied magnetic field, for instance s-states or eventually p_h-states.[†] Finally, the peak at 220 meV increases in energy with the increasing magnetic field. This is the expected behavior for a WL transition in a magnetic field. Indeed, using a WL electron mass $m_e = 0.07 m_o$ and a heavy hole mass $m_h = 0.22 m_o$, a slope of

$$\frac{1}{2}\hbar e(m_e^{-1} + m_h^{-1}) = 1.1 \text{ meV T}^{-1} \tag{4.1}$$

is expected for the WL absorption, which approximately corresponds to the PLE spectra where we measure a slope of 0.8 meV T^{-1}. This reinforces our earlier assumption that this peak is associated with a WL conduction band-WL valence band transition.

Let us now take a closer look at the intensites of the lower energy peaks, as shown in Fig. 4.6. At 0 T, the intensity of the low-energy peak at 50 meV is about 20% of that of the 75 meV peak. As the magnetic field increases, an exchange of strength between these two peaks is observed. For samples U1 and P3, at 20 T the two peaks have the same intensity and by 24 T the strength of the low-energy peak has surpassed that of its neighbor. For sample N2, the energy difference between the two peaks at 0 T is smaller and therefore the anticrossing is observed at a lower magnetic field. Such a behavior can not be explained using a purely electronic model. It is necessary to use a model that takes into account the coupling between the optical phonons and the photo-created electron-hole pair in the QD. Such a model is presented in the next section.

[†] An explanation of the 110 meV peak is given in Chapter 5

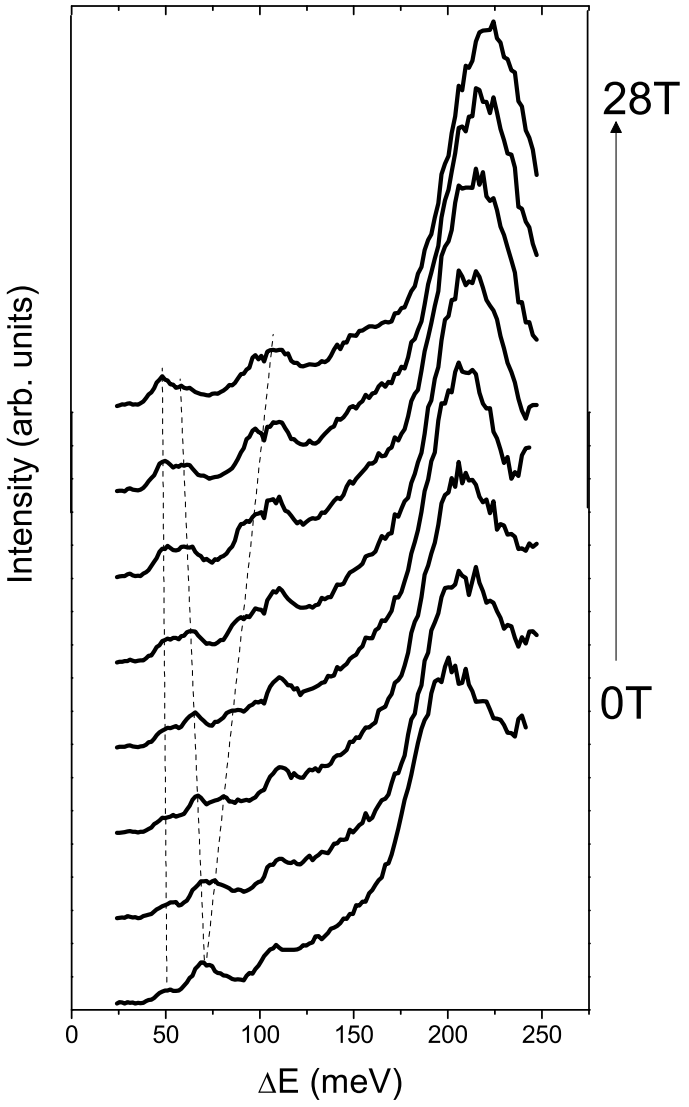

Figure 4.5: Magneto-PLE spectra of the P3 sample recorded at 4 K from B=0 to 28 T every 4 T and for E_{dect}=1215 meV. Traces have been vertically offset for clarity. The dashed lines are guides for the eyes ($\Delta E = E_{exc} - E_{det}$).

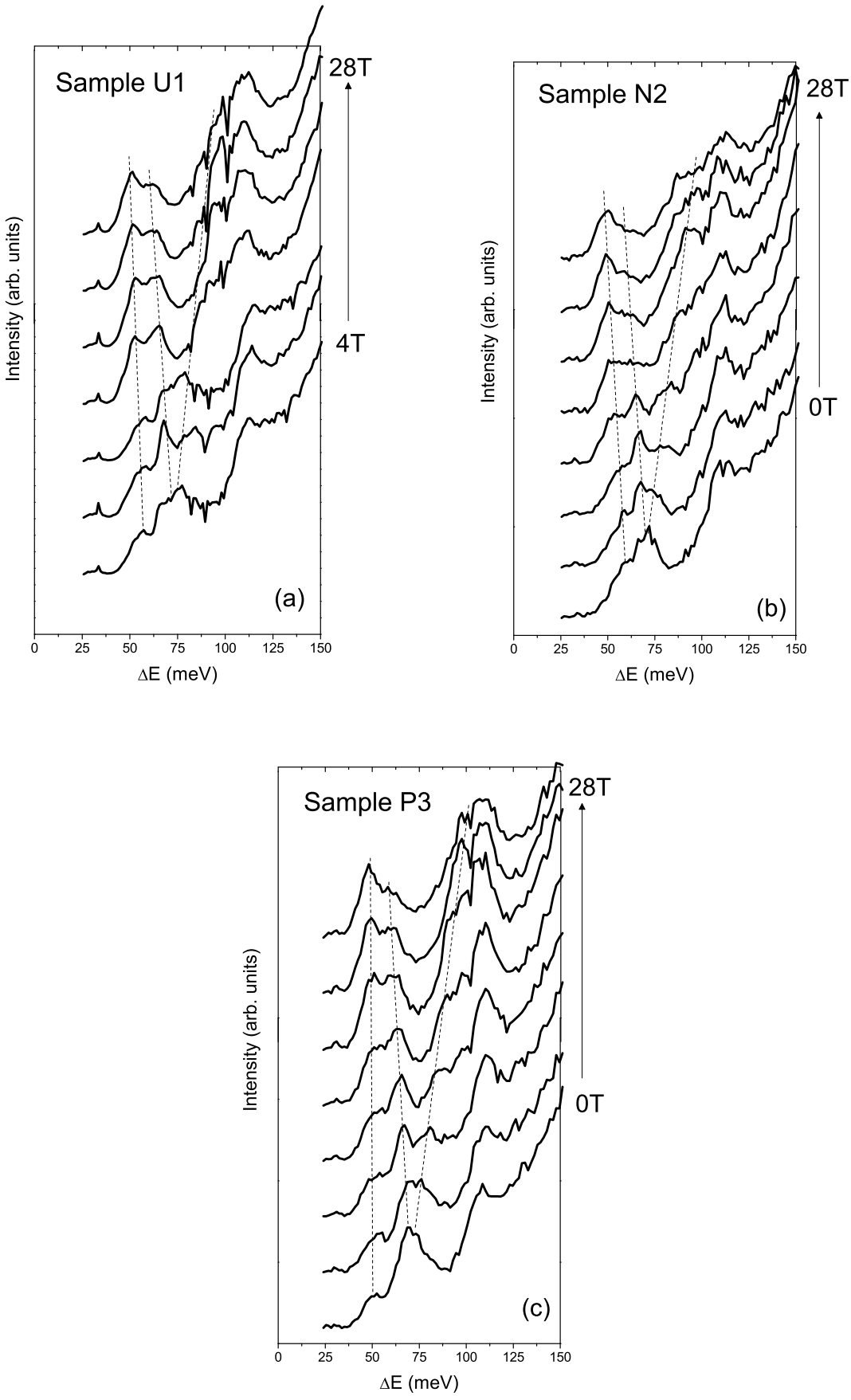

Figure 4.6: Magneto-PLE spectra of samples U1 (a), N2 (b) and P3 (c) at 4 K from B=0 to 28 T every 4 T and for a E_{det}=1215 meV. The dashed lines are guides for the eyes.

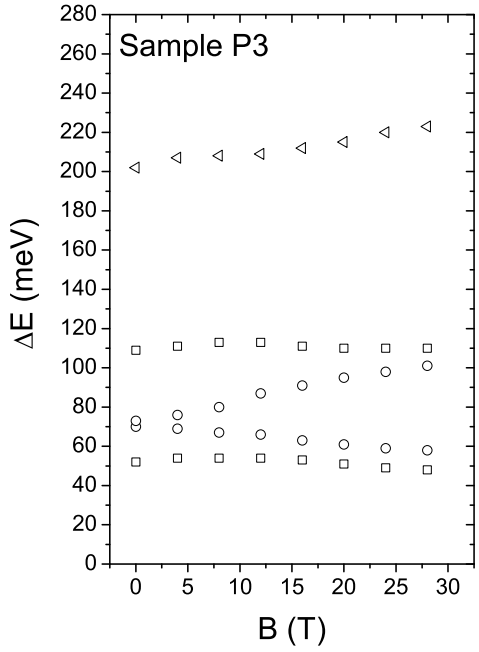

Figure 4.7: Magnetic field dispersion of measured PLE resonances in sample P3 for $E_{det} = 1215$ meV.

4.2 Calculation of Excitonic Polarons

In Chapters 2 (3), it was demonstrated that the interaction between an electron (hole) confined in a QD with the LO phonons of the crystal lattice leads to the formation of polaron states. In PL experiments, we create electron-hole pairs in our dots, which are electrically neutral. Since the coupling between carriers and optical phonons is basically electrical (Fröhlich interaction), one could expect a rather small coupling between LO phonons and excitons. However, recent theoretical works have shown that excitons in QDs strongly couple to LO phonons, in spite of their electrical neutrality [5, 6]. In this section, we will summarize the calculation of the excitonic polaron, as developed by T. Grange [7, 8].

4.2.1 Fröhlich Interaction

The non-interacting exciton-phonon states are labeled $|\upsilon_e, \upsilon_h, n_{\vec{\mathbf{q}}}\rangle$, where $|\upsilon_e\rangle$ is the electronic state, $|\upsilon_h\rangle$ the hole state, and as before, $|n_{\vec{\mathbf{q}}}\rangle$ denotes the number n of LO phonons with wavevector $\vec{\mathbf{q}}$. The Fröhlich Hamiltonian that describes the coupling between these states is simply the sum of the electron Fröhlich Hamiltonian and the hole Fröhlich Hamiltonian:[‡]

$$\begin{aligned}\mathbf{V}_F &= \mathbf{V}_F^e + \mathbf{V}_F^h \\ &= \frac{iA_F}{q\sqrt{V}} \sum_{\mathbf{q}} \Big[(e^{i\vec{\mathbf{q}}\cdot\vec{\mathbf{r}}_e} \mathbf{a}_{\vec{\mathbf{q}}}^+ - c.c.) + (-e^{i\vec{\mathbf{q}}\cdot\vec{\mathbf{r}}_h} \mathbf{a}_{\vec{\mathbf{q}}}^+ + c.c.) \Big] \\ &= \frac{iA_F}{q\sqrt{V}} \sum_{\mathbf{q}} \Big[(e^{i\vec{\mathbf{q}}\cdot\vec{\mathbf{r}}_e} - e^{i\vec{\mathbf{q}}\cdot\vec{\mathbf{r}}_h}) \mathbf{a}_{\vec{\mathbf{q}}}^+ - c.c. \Big]\end{aligned} \tag{4.2}$$

We find that this Hamiltonian has the same form as $\mathbf{V}_F^e$ and $\mathbf{V}_F^h$. We shall therefore proceed as we did in Section 2.1 (see Eq. 2.5), and calculate the matrix element of the exciton Fröhlich Hamiltonian between two exciton-phonon states.

$$\langle \upsilon_e', \upsilon_h', n_{\vec{\mathbf{q}}}' | \mathbf{V}_F | \upsilon_e, \upsilon_h, n_{\vec{\mathbf{q}}} \rangle \propto \delta_{n',n\pm1} [\delta_{\upsilon_h',\upsilon_h} \langle \upsilon_e' | e^{\pm i\vec{\mathbf{q}}\cdot\vec{\mathbf{r}}_e} | \upsilon_e \rangle - \delta_{\upsilon_e',\upsilon_e} \langle \upsilon_h' | e^{\pm i\vec{\mathbf{q}}\cdot\vec{\mathbf{r}}_h} | \upsilon_h \rangle] \tag{4.3}$$

Firstly, the delta function, $\delta_{n',n\pm1}$, tells us that the exciton Fröhlich term only couples states that differ by one phonon. This is analogous to the electron and hole coupling terms. However, unlike its electron and hole counterparts, the exciton-phonon states contain both an electron and a hole part. As a result, we find that Eq. 4.3 can be grouped into three categories (assuming that the phonon occupation numbers differ by one):

[‡]As $\mathbf{V}_F$ depends on the charge of the carrier, e, we have simply $\mathbf{V}_F^h = -\mathbf{V}_F^e$.

- the coupling between two exciton-phonon states who possess neither an electron nor a hole part in common ($\upsilon'_e \neq \upsilon_e$ and $\upsilon'_h \neq \upsilon_h$). It follows that $\delta_{\upsilon'_h,\upsilon_h} = \delta_{\upsilon'_e,\upsilon_e} = 0$. In this case, the term vanishes:

$$\langle \upsilon'_e, \upsilon'_h, 1_{\vec{\mathbf{q}}} | \mathbf{V}_F | \upsilon_e, \upsilon_h, 0 \rangle = 0 \tag{4.4}$$

- the coupling between two exciton-phonon states who possess both an electron and a hole part in common ($\upsilon'_e = \upsilon_e$ and $\upsilon'_h = \upsilon_h$). It follows that $\delta_{\upsilon'_e,\upsilon_e} = \delta_{\upsilon'_h,\upsilon_h} = 1$. In this case, Eq. 4.3 yields

$$\begin{aligned} \langle \upsilon_e, \upsilon_h, 1_{\vec{\mathbf{q}}} | \mathbf{V}_F | \upsilon_e, \upsilon_h, 0 \rangle &\propto \langle \upsilon_e | e^{i\vec{\mathbf{q}}\cdot\vec{\mathbf{r}}_e} | \upsilon_e \rangle - \langle \upsilon_h | e^{i\vec{\mathbf{q}}\cdot\vec{\mathbf{r}}_e} | \upsilon_e \rangle \\ &= V_{\upsilon_e\upsilon_e}(\vec{\mathbf{q}}) - V_{\upsilon_h\upsilon_h}(\vec{\mathbf{q}}) \end{aligned} \tag{4.5}$$

- the coupling between two exciton-phonon states who possess either an electron part or a hole part in common ($\upsilon'_e = \upsilon_e$ and $\upsilon'_h \neq \upsilon_h$ or $\upsilon'_e \neq \upsilon_e$ and $\upsilon'_h = \upsilon_h$). It follows that either $\delta_{\upsilon_e,\upsilon_e} = 1$ and $\delta_{\upsilon'_h,\upsilon_h} = 0$ or $\delta_{\upsilon'_e,\upsilon_e} = 0$ and $\delta_{\upsilon_h,\upsilon_h} = 1$. Taking the example where the two states have solely the hole part in common,[§] we find

$$\begin{aligned} \langle \upsilon'_e, \upsilon_h, 1_{\vec{\mathbf{q}}} | \mathbf{V}_F | \upsilon_e, \upsilon_h, 0 \rangle &\propto \langle \upsilon'_e | e^{i\vec{\mathbf{q}}\cdot\vec{\mathbf{r}}_e} | \upsilon_e \rangle \\ &= V_{\upsilon'_e\upsilon_e}(\vec{\mathbf{q}}) \end{aligned} \tag{4.6}$$

Eq. 4.5 gives us the coupling term between two identical exciton states. Due to the minus sign that differentiates the hole and electron Fröhlich Hamiltonians, we find that, if the wavefunctions of the two particles are similar, this term will be weak. This is in agreement with the initial intuition that an exciton, being a neutral entity, will be little affected by the the presence of an electric field.

However, according to Eq. 4.6, we find that a strong exciton LO-phonon interaction is possible if the coupling occurs between exciton states that differ by either an electron or hole part. Let's take the example used above, where only the electron part of the state changes. In this case, the hole remains a spectator and we find the same expression found for the coupling between electron states (see Eq. 2.5). This term is at the origin of the formation of excitonic polarons.

[§]Find similar result with the difference of a minus sign if we take the opposite case. But as it is only the square of this term that enters into our calculations the minus sign is not important.

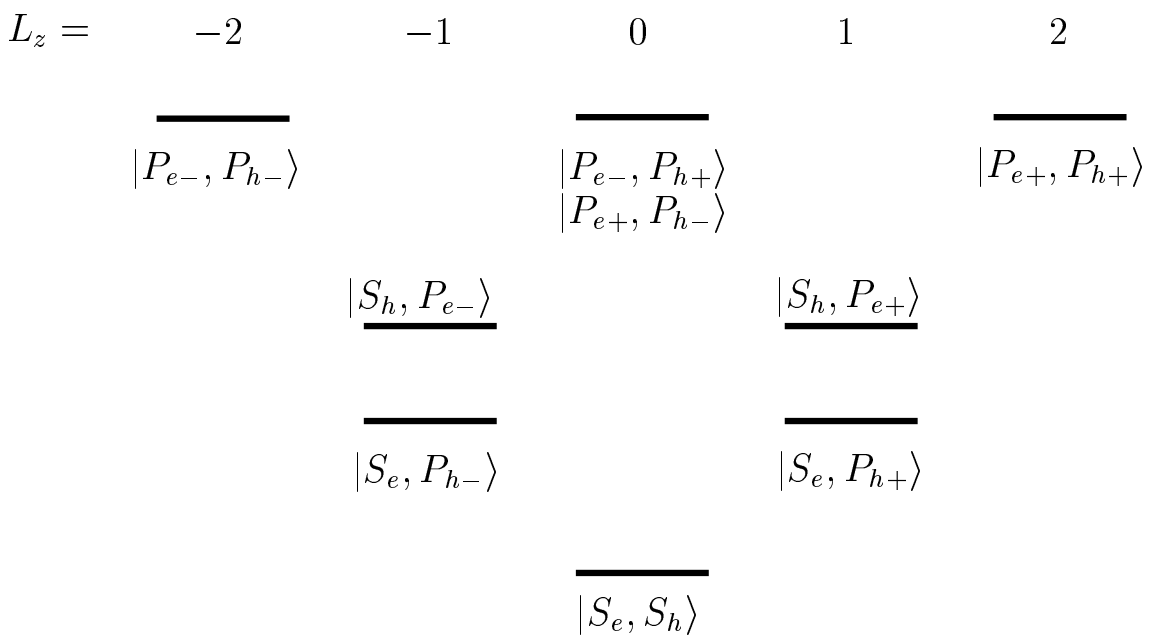

Figure 4.8: Different exciton states classified by their z-direction angular momentum, L_z.

4.2.2 Coulomb Interaction

The electron and hole created in the PL experiments are coupled to one another by the Coulomb Hamiltonian

$$\mathbf{H}_c = -\frac{e^2}{4\pi\epsilon_o\epsilon_r|\vec{\mathbf{r}}_e - \vec{\mathbf{r}}_h|} \tag{4.7}$$

As this Hamiltonian commutes with $\mathbf{L}_z$, it will only couple states that possess the same L_z.

We need only find the L_z of the exciton part of the exciton-phonon states, as the Hamiltonian does not act on the phonon parts. In Fig. 4.8, a schematic of the z-direction angular momentum of possible exciton states is given. As seen in Section 1.5.3, the dipole matrix element is non-zero for interband transitions when the initial and final states are equal. Therefore, only the states with $L_z = 0$ are optically active.

All identical exciton states will be coupled by $\mathbf{H}_c$. The matrix elements of these terms, using the wavefunctions for the carriers found in Chapter 1, is found to be ~ -20 meV [9]. The exciton levels undergo a down shift in energy due to the Coulomb interaction. In addition, we find

- three states with $L_z = 0$: $|s_e, s_h\rangle$, $|p_e^-, p_h^+\rangle$, $|p_e^+, p_h^-\rangle$
- two states with $L_z = +1$: $|s_e, p_h^+\rangle$, $|s_h, p_h^+\rangle$
- two states with $L_z = -1$: $|s_e, p_h^-\rangle$, $|s_h, p_h^-\rangle$

The matrix elements of the coupling between the states within the groups defined above is found to be on the order of ~ -5 meV [9]. It is only the states with $L_z = \pm 2$ that do not have coupling partners.

It is important to point out that the above discussion describes the Coulomb interaction in a neutrally charged dot (one electron and one hole), while our experimental results are from both neutrally charged dots (U1) and charged dots (N2 and P3). When dealing with negatively (positively) charged QDs, one has to consider trions, i.e. two electrons (holes) and one hole (electron). If we study the low-energy excitation spectrum of charged QDs neglecting spin-dependent effects, the additional charge remains a spectator and the excitation spectrum resembles that of neutral QDs [10]. This could explain why samples N2 and P3 display PLE spectra which are quite similar to those recorded in sample U1.

4.2.3 Calculation of Polaron States

Aside from the Coulomb interaction and difference in Fröhlich term treated above, the calculation of exciton polaron states is quite similar to that of electron and hole polarons. We start by finding the uncoupled states of the system in the experimental energy region (40 - 150 meV). Taking into account all possible electron-hole state combinations, 13 different uncoupled states can be found in the concerned energy region:

- 4 purely excitonic states $|p_e^{\pm}, p_h^{\pm}, 0\rangle$
- 8 excitonic state with one phonon continuum state $|s_e, p_h^{\pm}, 1_{\{\vec{\mathbf{q}}\}}\rangle$, $|p_e^{\pm}, s_h, 1_{\{\vec{\mathbf{q}}\}}\rangle$ and $|p_e^{\pm}, p_h^{\pm}, 1_{\{\vec{\mathbf{q}}\}}\rangle$
- the fundamental excitonic state with two phonon continuum states $|s_e, s_h, 2_{\{\vec{\mathbf{q}}\},\{\vec{\mathbf{q}}'\}}\rangle$

These states were determined using the LO phonon energy of GaAs. To simplify the calculation, we have limited ourselves to a one-phonon mode calculation. Taking into account solely the GaAs phonon mode is sufficient to our study, as the experimental observed anti-crossing (Fig. 4.6) that we are attempting to explain, takes place in an energy region where only states that include a GaAs phonon are found.

As the calculation involving all 13 states in quite cumbersome, we limit our presentation to the six uncoupled states that most affect the experimentally observed anti-crossing. A schematic of these states as a function of magnetic field is presented in Fig. 4.9.[¶]

Taking into account the information extracted earlier from Eq. 4.3, we find four separate occasions for a strong coupling interaction to occur.

- a coupling between the discrete state $|p_e^-, p_h^+, 0\rangle$ and the one phonon continuum $|s_e, p_h^+, 1_{\{\vec{\mathbf{q}}\}}\rangle$
- a coupling between the discrete state $|p_e^-, p_h^-, 0\rangle$ and the one phonon continuum $|s_e, p_h^-, 1_{\{\vec{\mathbf{q}}\}}\rangle$
- a coupling between the discrete state $|p_e^+, p_h^-, 0\rangle$ and the one phonon continuum $|s_e, p_h^-, 1_{\{\vec{\mathbf{q}}\}}\rangle$
- a coupling between the discrete state $|p_e^+, p_h^+, 0\rangle$ and the one phonon continuum $|s_e, p_h^+, 1_{\{\vec{\mathbf{q}}\}}\rangle$

[¶]This drawing is not to scale. In addition, we note that in the magnetic field range of our experiments, some of these states cross.

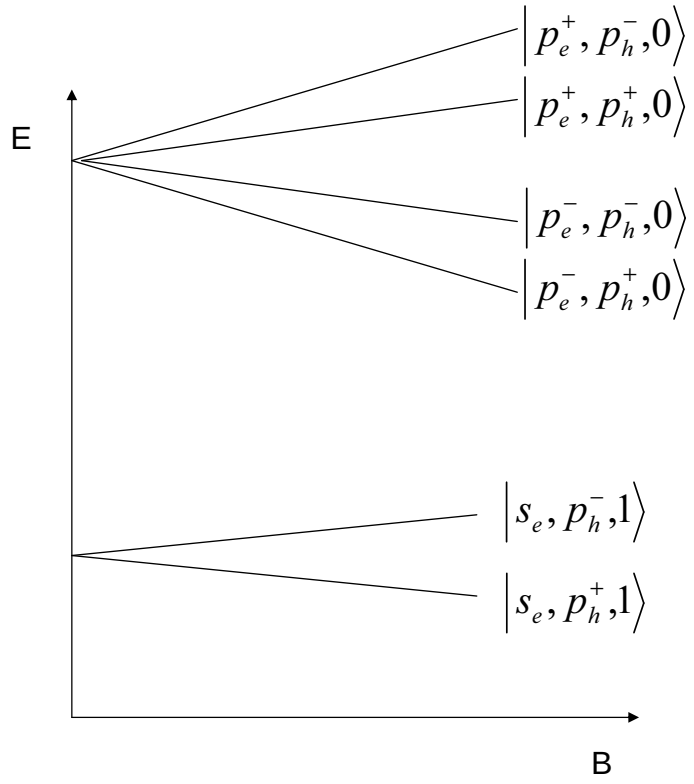

Figure 4.9: Schematic of the energy evolution in a magnetic field of the six non-interacting exciton-phonon states.

Using the effective potential method presented in Chapter 2, each of the above coupling situation can be reduced to a two-level system. We remark that, for all four occasions, it is the electron part of the exciton-phonon state that changes. It follows from Eq. 4.6, that the coupling term will depend solely on the electron part of the state while the hole remains a spectator. The first two situations involve a coupling between $|p_e^-\rangle$ and $|s_e\rangle$ while the last two situations involve a coupling between $|p_e^+\rangle$ and $|s_e\rangle$. For the calculation of the polaron states, it therefore suffices to introduce two linear combination phonon modes with two effective potentials.

$$\begin{aligned} |1_{\alpha(s_e p_e^-)}\rangle &= \sum_{\vec{\mathbf{q}}} \frac{V_{s_e p_e^-}(\vec{\mathbf{q}})|1_{\vec{\mathbf{q}}}\rangle}{V_{eff}(s_e p_e^-)} \\ |1_{\alpha(s_e p_e^+)}\rangle &= \sum_{\vec{\mathbf{q}}} \frac{V_{s_e p_e^+}(\vec{\mathbf{q}})|1_{\vec{\mathbf{q}}}\rangle}{V_{eff}(s_e p_e^+)} \end{aligned} \tag{4.8}$$

A Hamiltonian of the form

$$H = \begin{pmatrix} E_{p_e^\pm p_h^\pm}(B) & V_{eff} \\ V_{eff} & E_{s_e p_h^\pm}(B) + \hbar\omega_{LO} \end{pmatrix} \tag{4.9}$$

is found for each two-level system.[‖] By solving the Hamiltonian for each system, we find four independent pairs of polaron states.

Up until now, we have been concerned solely with the Fröhlich Hamiltonian. If we take into account other coupling terms, we find that these four systems are, in fact, not independent of one another.

Firstly, we must add the electron and hole anisotropy terms that couple respectively $|p_e^+\rangle$ with $|p_e^-\rangle$ and $|p_h^+\rangle$ with $|p_h^-\rangle$. These terms are the same as the ones used for the electron and hole polaron calculations in previous chapters. Secondly, the Coulomb Hamiltonian is added, whose effects were studied in the previous section. The addition of the Coulomb term will add diagonal elements on the order of -20 meV associated with the coupling between identical exciton states. In addition, we find two exciton states that possess the same L_z: $|p_e^-, p_h^+\rangle$ and $|p_e^+, p_h^-\rangle$. The Coulomb coupling between these states will produce a non-diagonal element of -3.6 meV. Fig. 4.10 gives a summary of the all the interactions that take place between the eight discrete states that make up our system.

The Hamiltonian of the system is now written

$$\mathbf{H} = \mathbf{H}_e(B) + \mathbf{H}_h(B) + \mathbf{V}_a^e + \mathbf{V}_a^h + \mathbf{V}_F + \mathbf{H}_c + \mathbf{H}_{ph} \tag{4.10}$$

[‖] As the states $|p_+\rangle$ and $|p_-\rangle$ are identical except for their dependence in θ, $V_{eff}(s_e p_e^+)$=$V_{eff}(s_e p_e^-)$, which we will note for short V_{eff}.

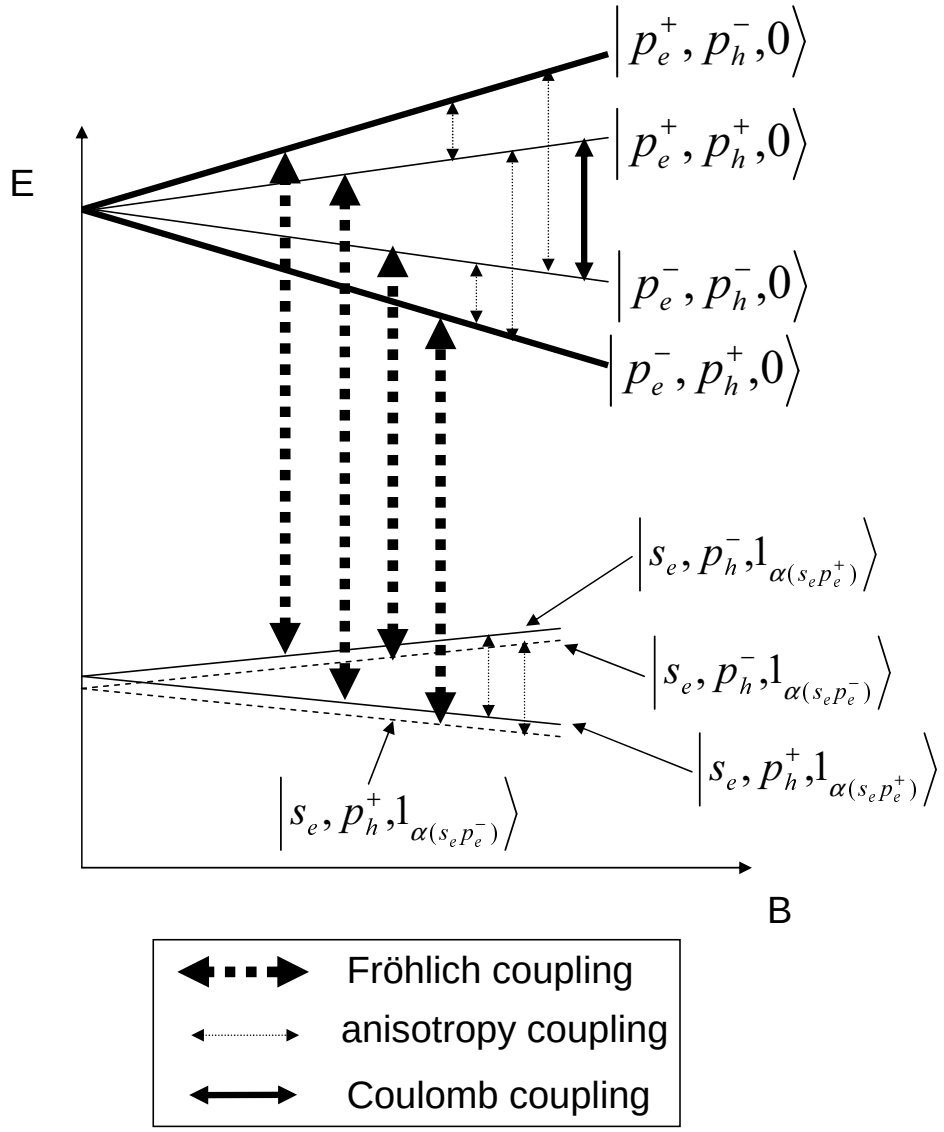

Figure 4.10: Diagram of the coupling interactions between the six exciton phonon states of our calculation.

In our eight state basis, Eq. 4.10 becomes

$$\begin{pmatrix}
\tilde{E}_{p_e^- p_h^+} & V_{eff} & \delta_a^h & 0 & V_{coul} & 0 & \delta_a^e & 0 \\
V_{eff} & \tilde{E}_{s_e p_h^+} + \hbar\omega_{LO} & 0 & \delta_a^h & 0 & 0 & 0 & 0 \\
\delta_a^h & 0 & \tilde{E}_{p_e^- p_h^-} & V_{eff} & \delta_a^e & 0 & 0 & 0 \\
0 & \delta_a^h & V_{eff} & \tilde{E}_{s_e p_h^-} + \hbar\omega_{LO} & 0 & 0 & 0 & 0 \\
V_{coul} & 0 & \delta_a^h & 0 & \tilde{E}_{p_e^+ p_h^-} & V_{eff} & \delta_a^h & 0 \\
0 & 0 & 0 & 0 & V_{eff} & \tilde{E}_{s_e p_h^-} + \hbar\omega_{LO} & 0 & \delta_a^h \\
\delta_a^e & 0 & 0 & 0 & \delta_a^h & 0 & \tilde{E}_{p_e^+ p_h^+} & V_{eff} \\
0 & 0 & 0 & 0 & 0 & \delta_a^h & V_{eff} & \tilde{E}_{s_e p_h^+} + \hbar\omega_{LO}
\end{pmatrix} \tag{4.11}$$

where δ_a^h and δ_a^e are respectively the hole and electron anisotropy terms, V_{coul} the non-diagonal Coulomb term, $\hbar\omega_{LO} = 36$ meV the GaAs LO phonon energy, and

$$E_{ij} = E_i(B) + E_j(B) + V_c^{ij} \tag{4.12}$$

$E_i(B)$ $[E_j(B)]$ is the B-dependent energy of the electronic (hole) level $|i\rangle$ ($|j\rangle$), which contains both the diamagnetic ($\sim B^2$) and Zeeman ($\sim B$) terms and V_c^{ij} is the diagonal Coulomb element.

We remark that Eq. 4.11 is the reduced Hamiltonian of the system. If we include all 13 original exciton-phonon states, we end up with a 21×21 matrix equation. The polaron states that result from the diagonalization of the full 21×21 Hamiltonian of the system are presented in Fig. 4.11. The area of the circles in the figure is proportional to the oscillator strength of the transitions, which will be calculated in Section 4.3.2. We predict several anti-crossings, the strongest observed at ~ 50 meV for a B field of ~ 20 T. This anti-crossing will be examined in detail in the next section where we will compare the calculated polaron states with the experimental PLE results. The parameters used in Fig. 4.11 will also be given in the next section.

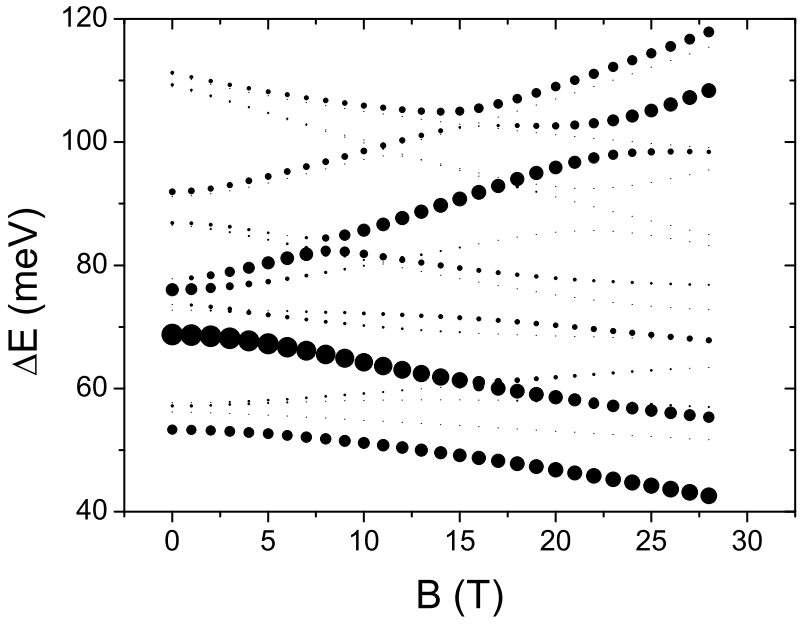

Figure 4.11: Calculated excitonic polaron energies and intensities as a function of the magnetic field. The area of the circles is proportional to the oscillator strength of the transitions. The parameters for this calculation are given in Section 4.3.

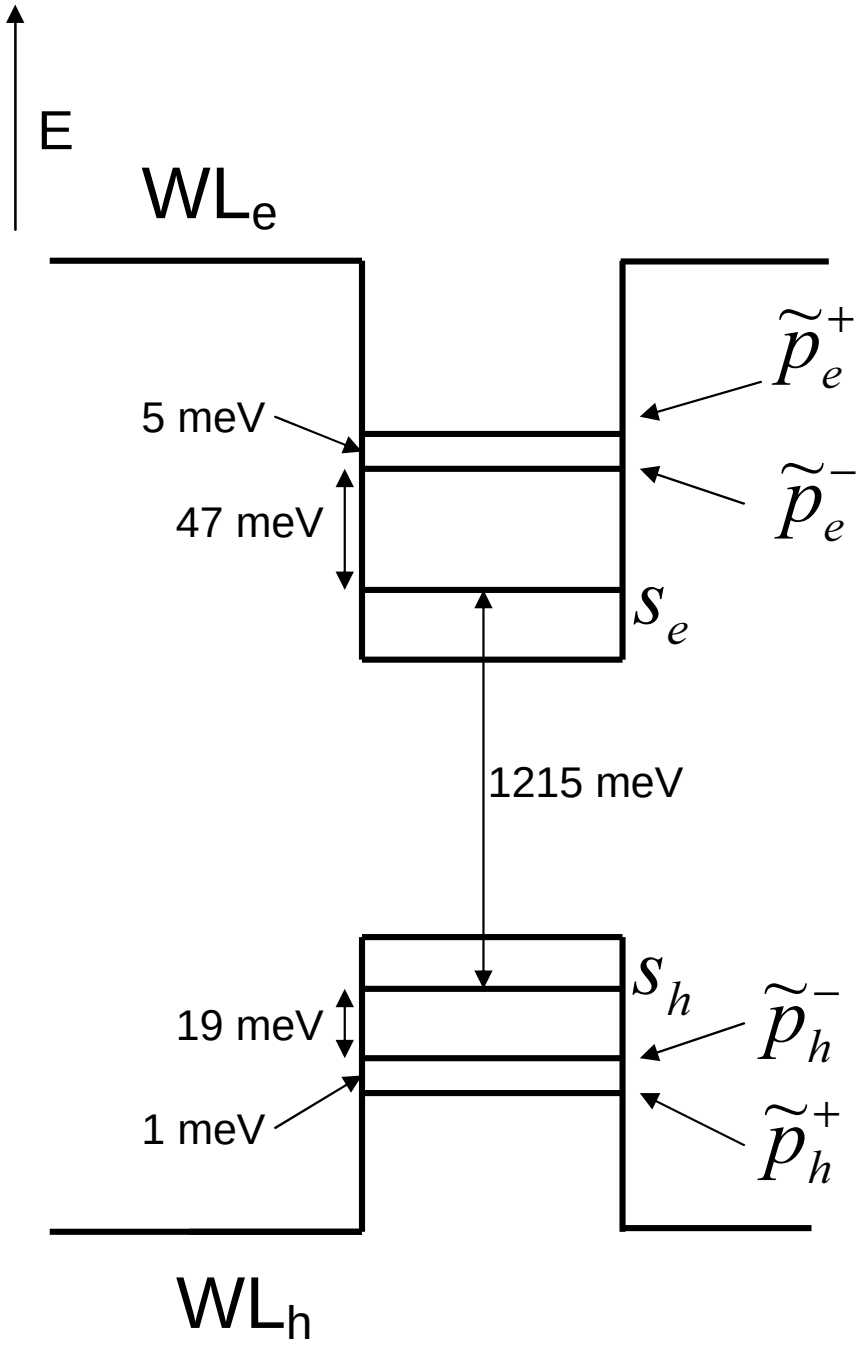

Figure 4.12: Schematic of energy levels at $B = 0$ T, with experimentally found values used in calculation.

4.3 Comparison Theory/Experiment

4.3.1 Comparison of Magnetic Dispersion Curves

In Fig. 4.13, we compare the magnetic field dispersion of the PLE resonances of sample P3 in symbols, with the calculated polaron states in solid lines. The energy positions as a function of magnetic field of the calculated levels are found to be in good agreement with our data. Many of the calculation parameters have been fixed to corroborate with our intraband magnetotransmission results (see Chapters 2 and 3). Figure 4.12 displays a schematic of the values of the different parameters used in our fit, i.e. $s_e - p_e$ and $s_h - p_h$ intraband energy transitions, the two anisotropy terms and the interband ground state energy. In addition, the values of the in-plane effective mass of the electron, $m_e = 0.07m_o$, and the hole, $m_h = 0.22m_o$, were imposed to agree with previous results (see respectively Section 2.2.1 and Section 3.3). The rest of the dot parameters, i.e. the size and the Fröhlich constant, were chosen to best fit the experimental results. The parameters resulting from the fit are the following: cone with a radius $R = 115$ Å, and height $h = 28$ Å, and conduction (valence) band offset of 290 meV (212meV). The dot size is consistent with direct size measurement[11] and the band offsets are compatible with an average gallium content of $x \simeq 0.5$ in the QDs ($In_{1-x}Ga_xAs$). The Fröhlich constant was found to be $\alpha_F = 0.105$ ($A_F = 0.00270$ meV·m^{-1}).**

In Fig. 4.14, we take a closer look at the two low-lying calculated polaron states, labeled (1) and (2). We present on the same graph, the uncoupled exciton-phonon states primarily responsible for the anti-crossing, $|p_e^-, p_h^+, 0\rangle$ and $|s_e, p_h^+, 1_{\alpha(s_e p_e^-)}\rangle$. The $|p_e^-, p_h^+, 0\rangle$ state displays a strong negative Zeeman slope with the magnetic field and crosses the one phonon state $|s_e, p_h^+, 1_{\alpha(s_e p_e^-)}\rangle$ for a magnetic field of around 20 T. These two states differ by one phonon and have different electronic wavefunctions. They are therefore directly coupled by the Fröhlich Hamiltonian. The coupling term between these two states, V_{eff}, was calculated and found to be 6 meV. A strong anti-crossing of $2V_{eff}$ is therefore predicted and observed in our experimental results. The next section will be dedicated to the study of the effects of this anti-crossing on the intensities of the PLE peaks as a function of magnetic field.

**See Appendix B

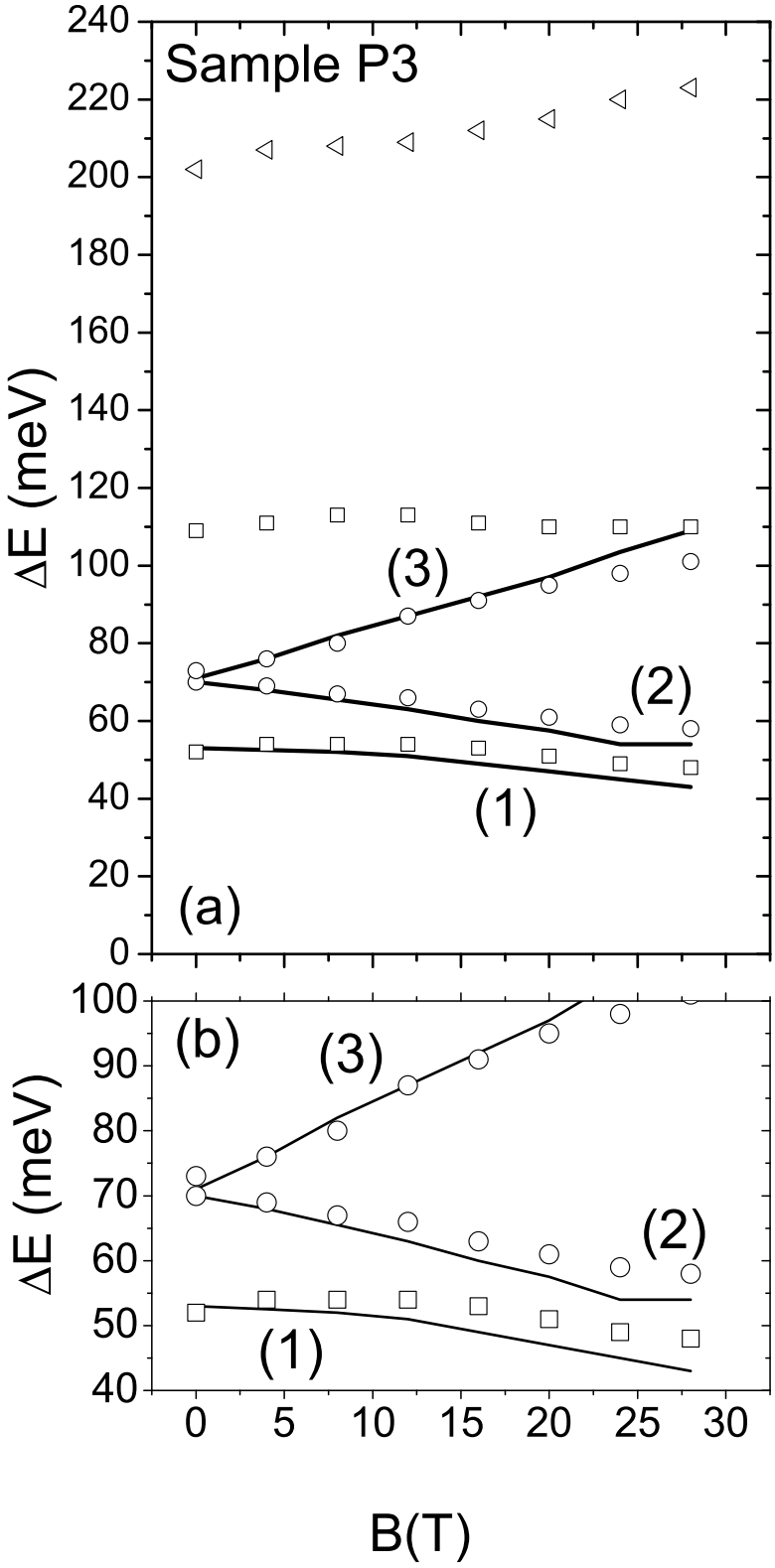

Figure 4.13: Magnetic field dispersion of PLE resonances in sample P3 in open figures with the calculated energy transitions in solid lines (a) and a zoom (b) of the polaron states (1), (2), and (3), as labeled in Fig. 4.14. Parameters used in this calculation are given in the text.

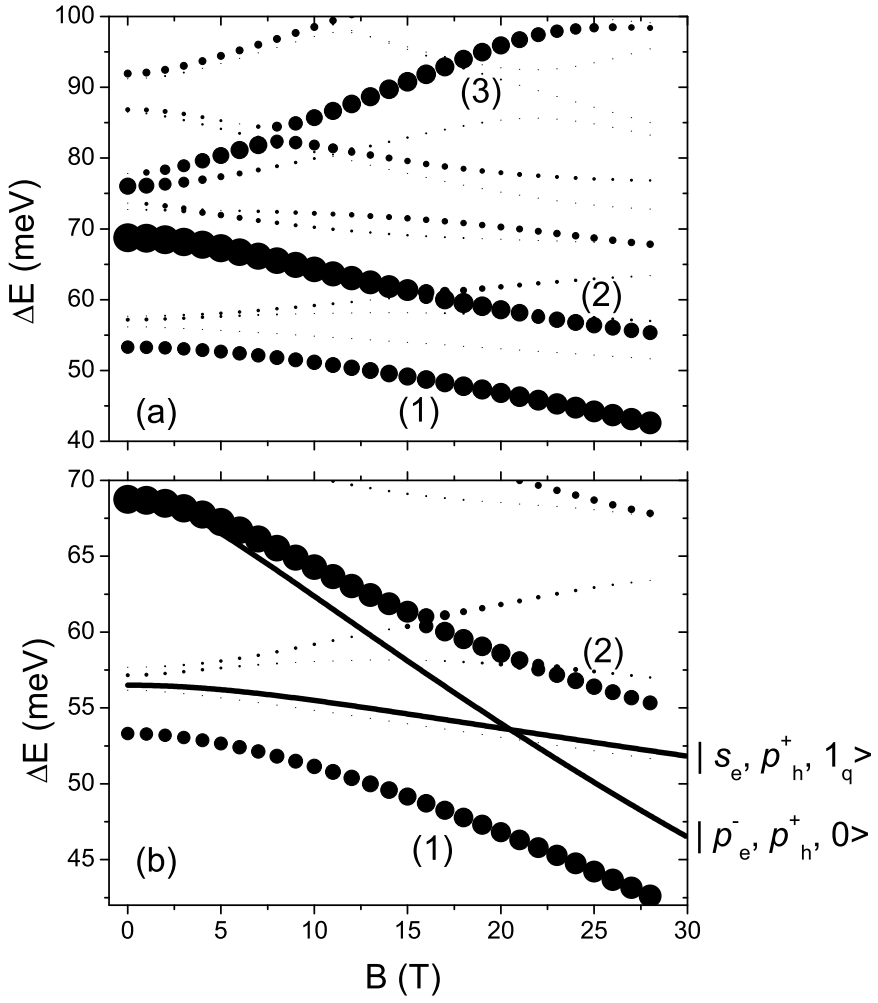

Figure 4.14: Calculated excitonic polaron energies and intensities as a function of the magnetic field (a) and a zoom (b) of the anticrossing between polaron states (1) and (2). The solid lines in (b) correspond to non-interacting exciton-phonon states. The area of the circles are proportional to the oscillator strengths.

4.3.2 Oscillator Strength

In Section 1.5.3, we found that the oscillator strength associated with interband transitions in our experiments was proportional to the square of the dot product of the hole envelope function with the electron envelope function (see Eq. 1.10). Written in terms of exciton-phonon states, Eq. 1.10 becomes:

$$OS_{i\to f} \propto |\langle\emptyset|\Psi\rangle|^2 \tag{4.13}$$

Initially, assuming we have neutrally charged dots, there are no carriers in the dots. The initial state is therefore composed of the empty set, $|\emptyset\rangle$. The final state is the polaron state which, in the 21 state basis, is written

$$|\Psi\rangle = \sum_{i=1}^{21} C_i|i\rangle \tag{4.14}$$

with

$$C_i = \langle i|\Psi\rangle \tag{4.15}$$

In the relevant energy spectra, the only optically active states are $|p_e^-, p_h^+, 0\rangle$ and $|p_e^+, p_h^-, 0\rangle$. We therefore have

$$OS_\Psi \propto |\langle p_e^-, p_h^+, 0|\Psi\rangle|^2 + |\langle p_e^+, p_h^-, 0|\Psi\rangle|^2 \tag{4.16}$$

For the anticrossing represented in Fig. 4.14, the oscillator strengths of polarons (1) and (2) are roughly proportional to their weight on the $|p_e^-, p_h^+\rangle$ state. Hence we observe an exchange of oscillator strength between the two polarons as the magnetic field is increased.

Using Eq. 4.16, we calculate the interband absorptions. The solid lines in Fig. 4.15 represent the calculated absorption spectra at different magnetic fields. Each discrete level is replaced by a Gaussian peak with a FWHM of 12 meV in order to account for inhomogeneous broadening. We compare our calculated interband absorption spectra with the PLE experimental data. The full squares are data points taken for sample P3 for $E_{det} = 1215$ meV. The evolution of the peak intensities with the magnetic field is very well described by our model. We are able to predict the exchange of oscillator strength observed in our results demonstrating the validity of our analysis and the existence of excitonic polarons. Similar agreement is found for results obtained for sample U1 and N2.

We point out that, in general, a PLE signal is not necessarily equivalent to an absorption spectrum. The very good agreement obtained here, between the two is due to the short polaron relaxation time compared to interband radiative decay time. Far-infrared pump-probe spectroscopy experiments have demonstrated that intraband polaron decay time in InAs/GaAs QDs varies between 20 and 70 ps depending on the polaron energy [12, 13]. Excitonic polaron relaxation times are expected to be on the same order of magnitude, the relaxation mechanism (due to phonon anharmonicity) being similar. Since interband radiative decay time is on the order of 1 ns, the relaxation process will always go through the ground exciton state. Hence the PLE is proportional to the absorption.

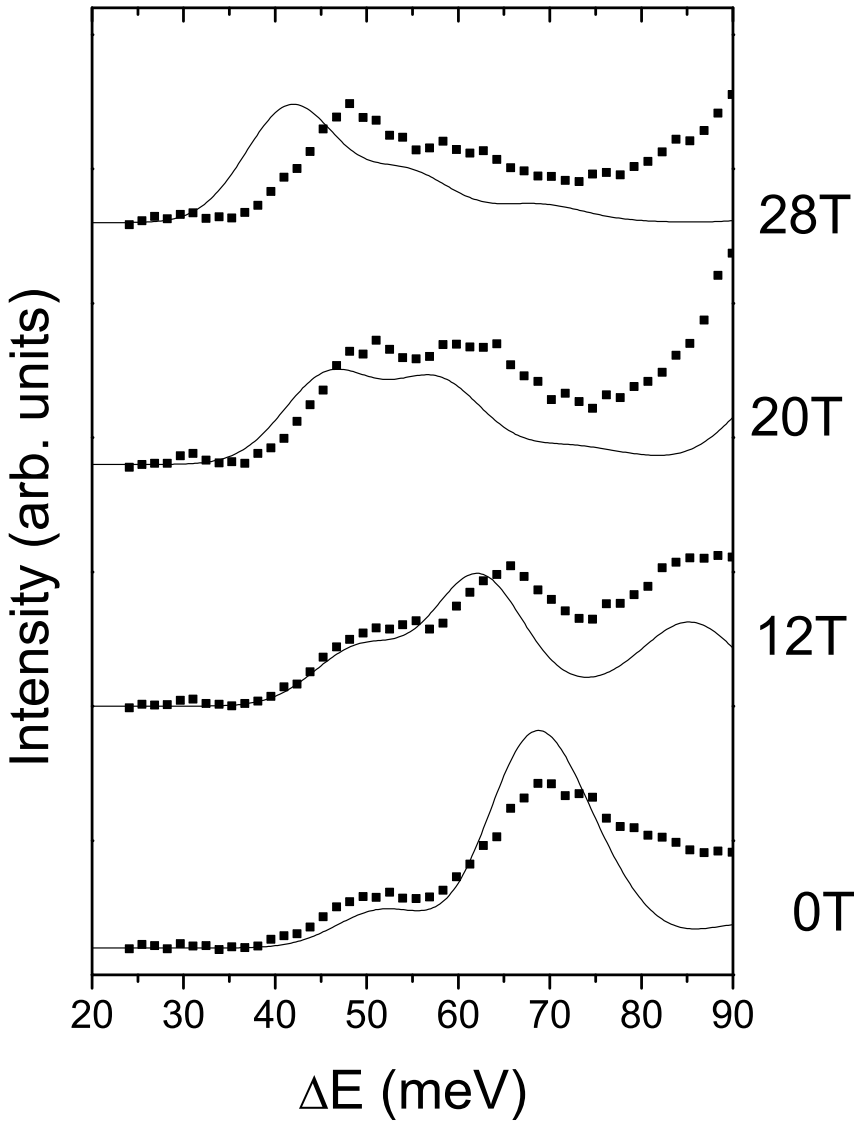

Figure 4.15: Experimental (full squares) and calculated (solid lines) spectra for different magnetic fields. The experimental data was taken for an E_{det}=1215 meV and for sample P3. The parameters used in the calculation are given in the text.

4.4 Conclusion

In summary, we have investigated the interband transitions in several ensembles of self-assembled InAs/GaAs QDs by using PLE spectroscopy under a strong magnetic field. The magnetic field dependence of the interband transitions allows for their unambiguous assignment, as the effect of a magnetic field is significantly different for s or p states.

We have calculated the coupling between the mixed exciton-LO phonon states using the Fröhlich Hamiltonian and we have determined the energies and oscillator strengths of the interband transitions. When two exciton-LO phonon states have close enough energies with phonon occupations which differ by one, a large anticrossing is theoretically predicted. Such a situation is experimentally induced in our samples by the applied magnetic field for the two interband transitions ($|p_e^-, p_h^+, 0\rangle, |s_e, p_h^+, 1_{\alpha(s_e p_e^-)}\rangle$) and a strong anticrossing is actually observed in all the investigated samples.

Our model accounts well for the experimental data, evidencing that the excitons and LO-phonons are in a strong coupling regime in QDs and that the interband transitions occur between excitonic polaron states. This conclusion will be supported in the next chapter, where we will present evidence of excitonic polarons through resonant photoluminescence (RPL) measurements.

Bibliography

[1] N. I. Cade, H. Gotoh, H. Kamada,H. Nakano, and H. Okamoto, *Fine structure and magneto-optics of exciton, trion, and charged biexciton states in single InAs quantum dots emitting at 1.3 μm*, Phys. Rev. B **73**, 115322 (2006).

[2] R. Oulton, J.J. Finley, A.I. Tartakovskii, D.J. Mowbray, M.S. Skolnick, M. Hopkinson, A. Vasanelli, R. Ferreira, and G. Bastard, *Continuum transitions and phonon coupling in single self-assembled Stranski-Krastanow quantum dots*, Phys. Rev. B **68**, 235301 (2003).

[3] R. Heitz, O. Stier, I. Mukhametzhanov, A. Madhukar, and D. Bimberg, *Quantum size effect in self-organized InAs/GaAs quantum dots*, Phys. Rev. B **62**, 11017 (2000).

[4] C. Kammerer, G. Cassabois, C. Voisin, C. Delalande, Ph. Roussignol, and J. M. Gérard, *Photoluminescence Up-Conversion in Single Self-Assembled InAs/GaAs Quantum Dots*, Phys. Rev. Lett. **87**, 207401 (2001).

[5] O. Verzelen, R. Ferreira, and G. Bastard, *Excitonic Polarons in Semiconductor Quantum Dots*, Phys. Rev. Lett. **88**, 146803 (2002).

[6] R. Heitz, I. Mukhametzhanov, O. Stier, A. Madhukar, and D. Bimberg, *Enhanced Polar Exciton-LO-Phonon Interaction in Quantum Dots*, Phys. Rev. Lett. **83**, 4654 (1999).

[7] V. Preisler, T. Grange, R. Ferreira, L. A. de Vaulchier, Y. Guldner, F. J. Teran, M. Potemski, and A. Lemaître, *Evidence for excitonic polarons in InAs/GaAs quantum dots*, Phys. Rev. B **73**, 075320 (2006).

[8] T. Grange, Ph.D. thesis, Université Paris VI, in progress.

[9] O. Verzelen, Ph.D. thesis, *Interaction électron-phonon LO dans les boîtes quantiques d'InAs/GaAs*, Université Paris VI (2002).

[10] M. E. Ware, E. A. Stinaff, D. Gammon, M. F. Doty, A. S. Bracker, D. Gershoni, V. L. Korenev, S. C. Badescu, Y. Lyanda-Geller, and T. L. Reinecke, *Polarized Fine Structure in the Photoluminescence Excitation Spectrum of a Negatively Charged Quantum Dot*, Phys. Rev. Lett. **95**, 177403 (2005).

[11] B. Grandidier, Y. M. Niquet, B. Legrand, J. P. Nys, C. Priester, D. Stiévenard, J. M. Gérard and V. Thierry-Mieg, *Imaging the Wave-Function Amplitudes in Cleaved Semiconductor Quantum Boxes*, Phys. Rev. Lett. **85** 1068 (2000).

[12] S. Sauvage, P. Boucaud, R.P.S.M. Lobo, F. Bras, G. Fishman, R. Prazeres, F. Glotin, J. M. Ortega, and J. M. Gérard, *Long Polaron Lifetime in InAs/GaAs Self-Assembled Quantum Dots*, Phys. Rev. Lett. **88**, 177402 (2002).

[13] E. A. Zibik, L. R. Wilson, R. P. Green, G. Bastard, R. Ferreira, P. J. Phillips, D. A. Carder, J-P. R. Wells, J. W. Cockburn, M. S. Skolnick, M. J. Steer, and M. Hopkinson, *Intraband relaxation via polaron decay in InAs self-assembled quantum dots*, Phys. Rev. B **70**, 161305 (2004).

Chapter 5

Exciton-LO Phonon Interaction: RPL Experiments

In this chapter, resonant photoluminescence (RPL) experimental results are investigated. First, RPL spectra as a function of magnetic field and excitation energy are studied. A qualitative explanation of how these results are affected by the size inhomogeneity of dots in a self-assembled sample will be given. Then, the magneto-RPL spectra will be compared to the excitonic polaron calculation of the previous chapter.

5.1 RPL Spectroscopy

In RPL spectroscopy, the fixed excitation energy is less than the GaAs gap and the InAs wetting layer, as seen in Fig. 5.1(a). Only subensembles of similar sized QDs are resonantly excited and contribute to the PL signal. Dots that possess an excited state in resonance with the fixed excitation energy, E_{exc}, are excited. The system relaxes to its ground state and gives off a photon of energy equal to its ground state energy. The detection energy, E_{det}, is varied such that several resonances are observed, each one corresponding to the signal of a subensemble of similar dots. Essentially, we are measuring the same quantities as in a PLE measurement. However, in a PLE measurement, one spectrum corresponds to one detection energy and therefore one subensemble of similarly sized dots in the sample. This is different from a RPL measurement, where one spectrum corresponds to a range of detection energies and therefore each peak in the spectrum corresponds to a different subensemble of similarly sized dots [see Figure 5.1(b)].

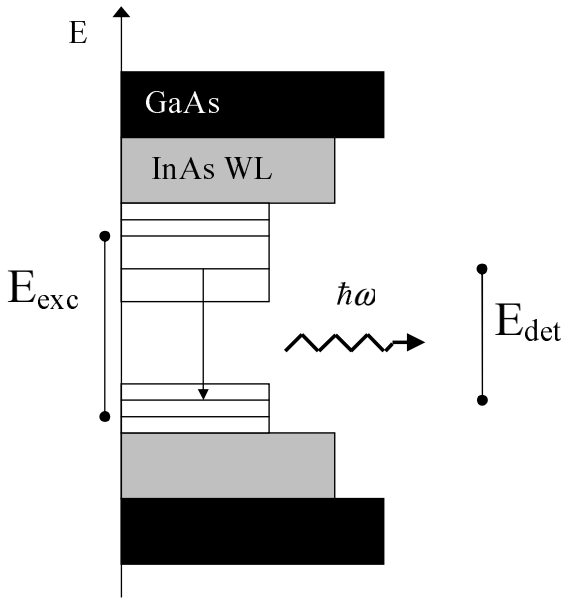

(a)

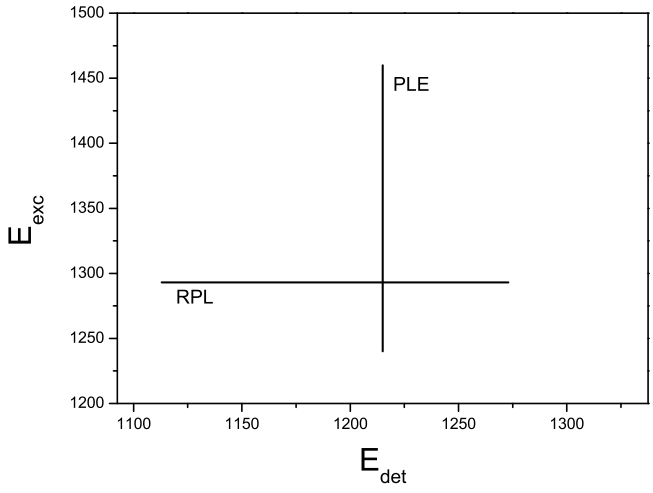

(b)

Figure 5.1: A schematic of the RPL process in a QD (a). Energy domains for a PLE measurement with a fixed detection energy, E_{det} = 1215 meV and for a RPL measurement with a fixed excitation energy, E_{exc} = 1293 meV (b).

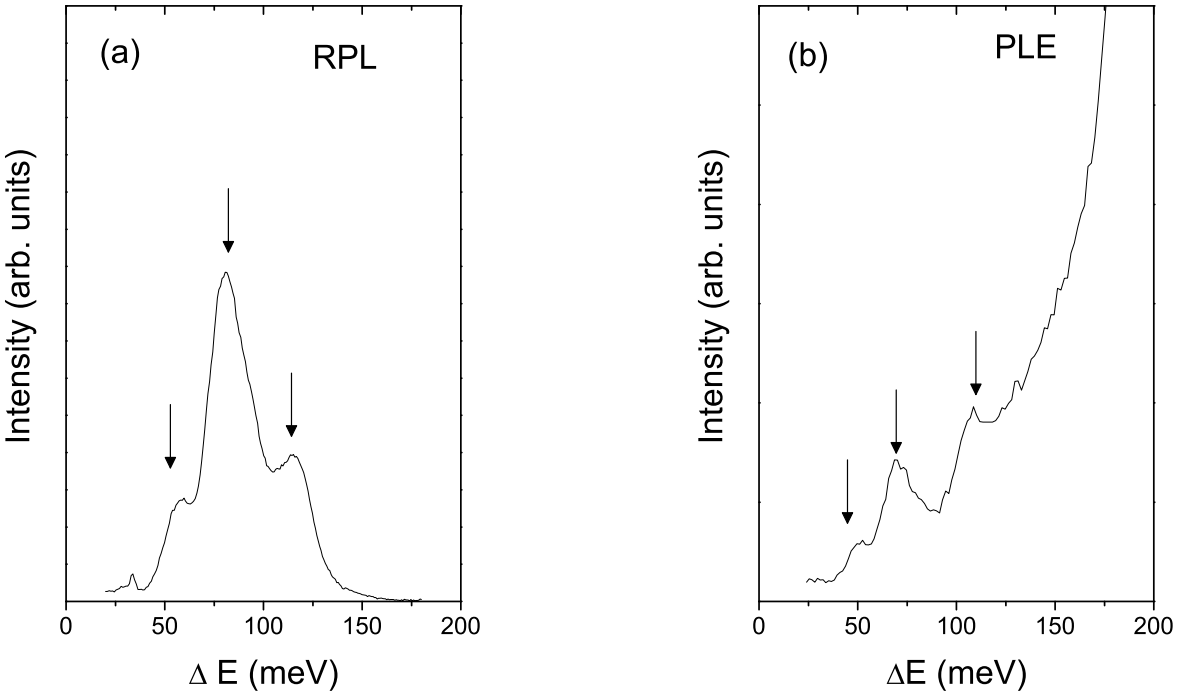

Figure 5.2: Zero field comparison of an RPL spectrum (a) taken for a fixed $E_{exc} = 1293$ meV and PLE spectrum (b) measured for a fixed $E_{det} = 1215$ meV. Both spectra were recorded on sample P3 at 4 K.

In addition, as the detector in RPL measurement is a photomultiplier, the quality of a RPL spectrum, in terms of signal versus noise, is superior to that of a PLE spectrum. This is demonstrated in Fig. 5.2, where a RPL and PLE spectra, taken for sample P3 at zero tesla, are displayed side by side. The x-axis for both graphs corresponds to the excess excitation energy $\Delta E = E_{exc} - E_{det}$. The RPL measurement was taken for a fixed excitation energy, $E_{exc} = 1293$ meV, while E_{det} was varied. For the PLE spectra, it was the excitation energy that was varied and the detection energy that was fixed at $E_{det} = 1215$ meV. We recognize the same three features, indicated by arrows in the figure, in both spectra. The peaks in the RPL spectra are well pronounced and more easily identifiable than those of the PLE measurement. In particular, the tail of the wetting layer (WL) peak perturbs the observation of the lower energy, weaker intensity peaks. This is most notable for the peak at ~ 110 meV. The increasing background slope observed in Fig. 5.2(b) due to the WL is a common phenomena in PLE measurements [1, 2]. As the excitation energy in RPL measurements is below the WL bandedge, this slope is not observed for such an experiment. We shall see that the quality of the RPL spectra will enable the clear observation of the anti-crossing between the low lying polaron levels calculated in the previous chapter.

5.2 Experimental Results

In this section, magneto-RPL measurements as well as zero field RPL spectra for different excitation energies will be presented. We will focus on the results obtained for sample P3, but similar results were acquired for our undoped (U1) and n-doped (N2) samples. Effects of the dot size distribution of our samples on these results will be discussed. We will then reexamine the magneto-RPL measurements of sample P3, this time comparing them with the excitonic polaron energy levels and oscillator strengths calculated in Chapter 4.

5.2.1 Magneto-RPL Measurements

Figure 5.3 depicts the RPL spectra for an excitation energy $E_{exc} = 1293$ meV recorded at 4 K on sample P3 from $B = 0$ to 28 T every 4 T. At 0 T, three distinct features are observed: a low energy peak at $\sim$ 59 meV, a high energy peak at $\sim$ 116 meV and a more pronounced peak at $\sim$ 80 meV. The low energy peak decreases slightly in energy and increases in intensity as the magnetic field is increased. The peak initially at 80 meV splits into two separate peaks: one peak that increases in energy with the magnetic field and one that decreases. In addition, we observe an exchange in intensity between this descending peak and the low energy one. The high energy peak is observed to stay nearly constant in energy with the magnetic field, until it disappears for magnetic fields greater than 16 T. Finally, we note the appearance of a small feature at 8 T between the two high energy peaks at $\sim$ 101 meV. This peak increases in energy until a magnetic field of 24 T, after which it disappears.

We compare this behavior with the same experiment conducted for an excitation at lower energy, $E_{exc} = 1260$ meV as seen in Fig. 5.4. At this excitation energy, only two features are observed at 0 T: a peak at $\sim$ 55 meV and a peak of higher energy at $\sim$ 75 meV. The two peaks undergo an obvious exchange in intensity as the magnetic field is increased. No features above an energy of 100 meV are observed.

The existence of a distribution of different sized dots in our samples is at the origin of the different results discussed above. As noted in Chapter 4, the broad bell-like peak of an NRPL spectrum is a good indication of the size inhomogeneity among the dots in a single sample. We can conclude, from the NRPL peak in Fig. 4.1, that our samples contain a large population of dots with interband ground state energy, $E(s_e s_h) = 1200$ meV. Progressively less dots are found the further the distance from 1200 meV. Finally no dots exist for an $E(s_e s_h)$ greater than (less than) $\sim$ 1280 meV ($\sim$ 1140 meV). Taking this into account, we will illustrate, with the help of Figures 5.5 and 5.6, the origin of the differences in the spectra obtained for $E_{exc} = 1293$ meV as compared to $E_{exc} = 1260$ meV.

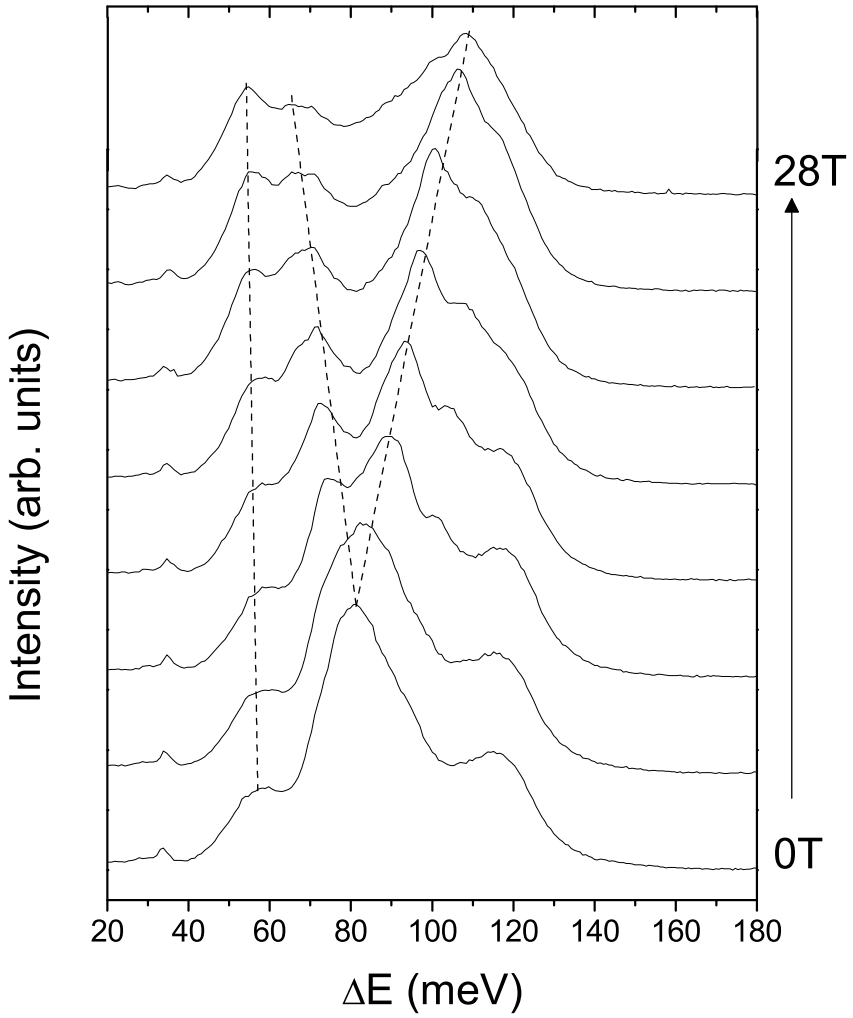

Figure 5.3: Magneto-RPL spectra recorded on sample P3 at 4 K from $B = 0$ to 28 T every 4 T and for $E_{exc} = 1293$ meV. Traces have been vertically offset for clarity. The dashed lines are guides for the eyes.

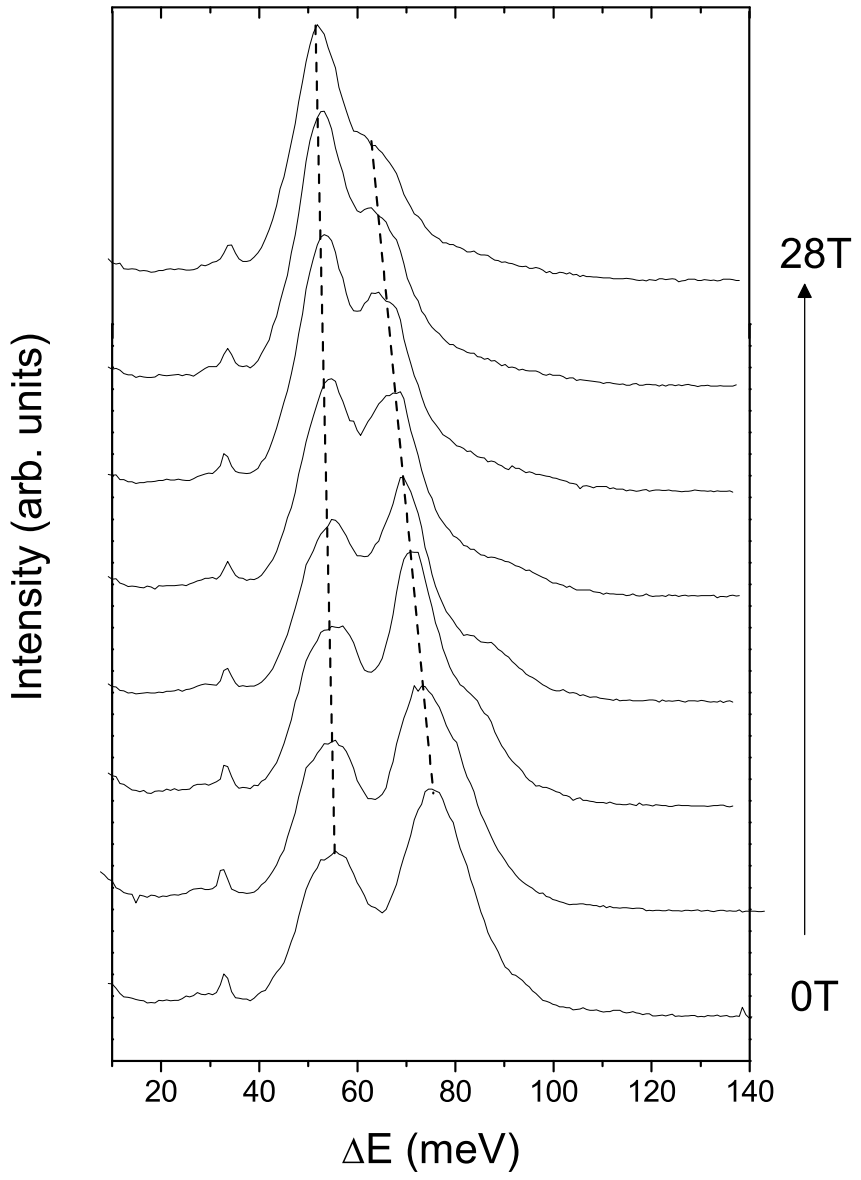

Figure 5.4: Magneto-RPL spectra recorded on sample P3 at 4 K from $B = 0$ to 28 T every 4 T and for $E_{exc} = 1260$ meV. Traces have been vertically offset for clarity. The dashed lines are guides for the eyes.

Figures 5.5 and 5.6 display a schematic of the evolution of 3 different electron-hole pair QD states (X_1, X_2 and X_3) as a function of the parameters of the dot, i.e. height, radius, interdiffusion, etc. We assume that the range of dots presented on the x-axis of the figures corresponds to the distribution of dot sizes in our sample. The state labeled X_1 corresponds to the low energy peaks observed in both Fig. 5.3 and Fig. 5.4. The two peaks observed in Fig. 5.3, that decrease and increase in energy, can be associated with the exciton states $|p_e^-, p_h^+\rangle$ and $|p_e^+, p_h^-\rangle$ and are noted X_2^- and X_2^+ respectively. At zero tesla, these two peaks merge into one peak which is labeled X_2^0. Finally, the high energy peak, observed in Fig. 5.3, that hardly moves with the magnetic field is noted X_3. The origin of X_1 and X_3 will be discussed later.

In Fig. 5.5(a), the situation of a RPL measurement at 0 T and for an excitation energy of 1293 meV is illustrated. This excitation energy coincides with the excited state energy of three different subensembles of similarly sized dots. It excites the X_1 level of a certain subensemble of dots, the X_2^0 level of another subensemble of dots and finally the X_3 level of a third subensemble of dots. The electron-hole pair excited in these levels relaxes to the ground state. The pair then recombines emitting a photon which we detect. We predict the detection of three peaks, which corresponds to the 0 T spectrum in Fig. 5.3. When a magnetic field is applied four peaks are detected, as illustrated in Fig. 5.5(b) and observed in Fig. 5.3 for a magnetic field of 12 T, for example.

We note that the subensemble of dots whose X_2^0 level coincides with $E_{exc} = 1293$ meV will be detected at zero field at

$$\begin{aligned} E_{det} &= E_{exc} - \Delta E \\ &= 1293 - 80 \text{ meV} \\ &= 1213 \text{ meV} \end{aligned} \tag{5.1}$$

We know, from NRPL measurements, that a large population of dots exists at this detection energy. There will also be a good population of dots for the X_1 energy level ($E_{det} = 1234$ meV) and X_3 energy level ($E_{det} = 1183$ meV).

This is not the case for $E_{exc} = 1260$ meV (Fig. 5.6). At this excitation energy, QD states with $\Delta E \geq 100$ meV will have detection energies $E_{det} \leq 1160$ meV. These energies are found in the tail of the NRPL peak. It follows that the population of QDs possessing such detection energies is very small or non-existent. The result of the above is illustrated in Fig. 5.6. In the case of $B = 0$ ($B > 0$), the excitation energy coincides with only two energy levels: X_1 and X_2^0 (X_2^-). There are no dots in our samples with a X_2^+ or X_3 energy level that coincide with $E_{exc} = 1260$ meV. This is observed in Fig. 5.4, where only two peaks are detected for a RPL experiment conducted for $E_{exc} = 1260$ meV.

We make the remark that the energy evolution of QD states as a function of the dot parameters are not necessarily the parallel lines represented in Figures 5.5 and 5.6. As discussed in Chapter 1, these functions, which can be calculated using several different methods, depend on the parameters taken into account in the calculation (shape, composition, strain effects...) [3, 4, 5]. In Fig. 1.7 of Chapter 1, the results of a calculation using the effective mass method were presented. The QD levels as a function of height and radius independently were displayed. We found that the evolution of states is not quite parallel, in particular, when there exists a variation

in the radius of the islands. The variation in height has less of an impact on the intraband energy transitions. We have chosen to schematically represent the energy levels evolving in parallel lines in order to facilitate the discussion.

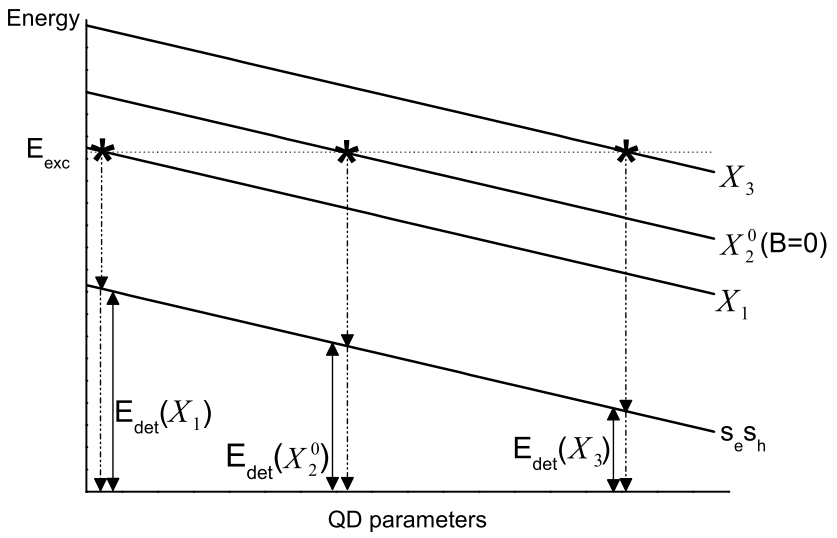

(a)

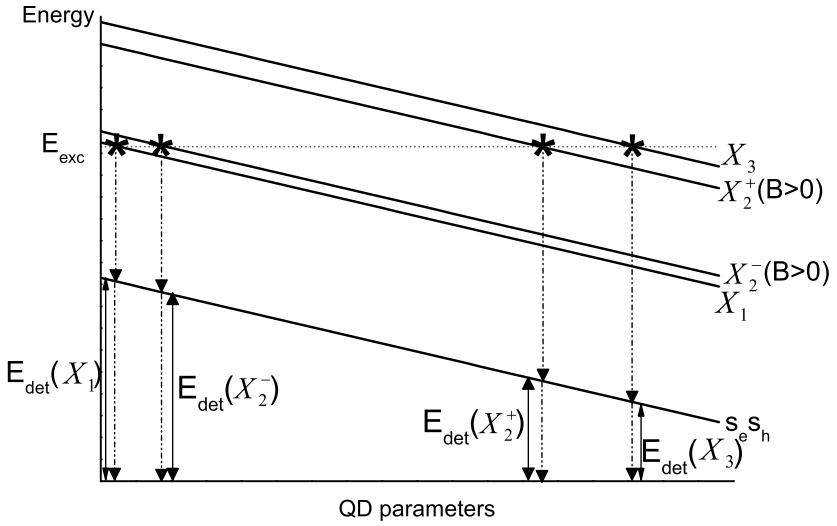

(b)

Figure 5.5: Schematic of the exciton energy levels displayed as a function of dot parameters. The dashed arrows represent the relaxation process during a RPL measurement with $E_{exc} = 1293$ meV at $B = 0$ T (a) and when a magnetic field is applied (b).

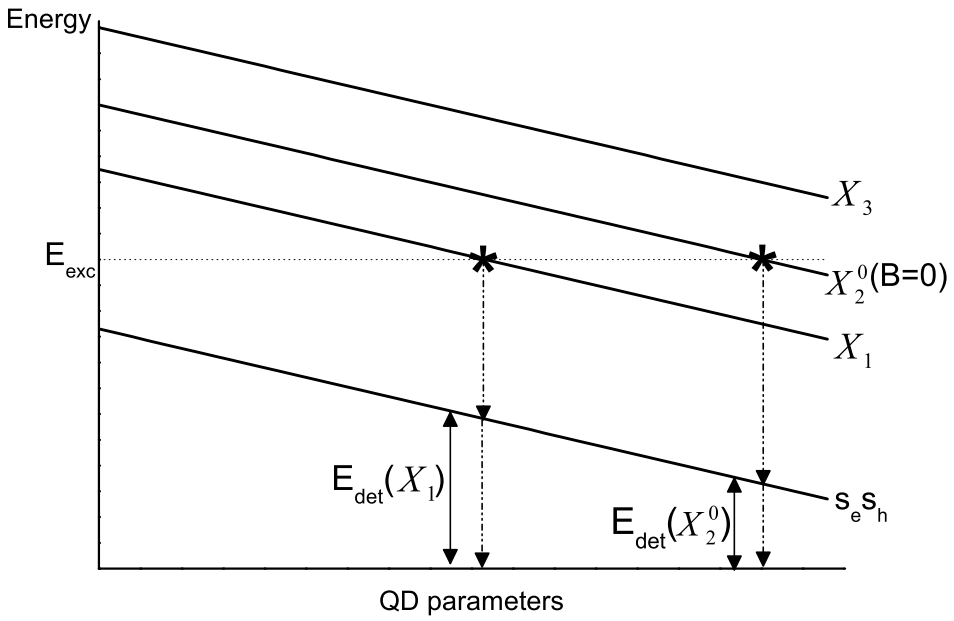

(a)

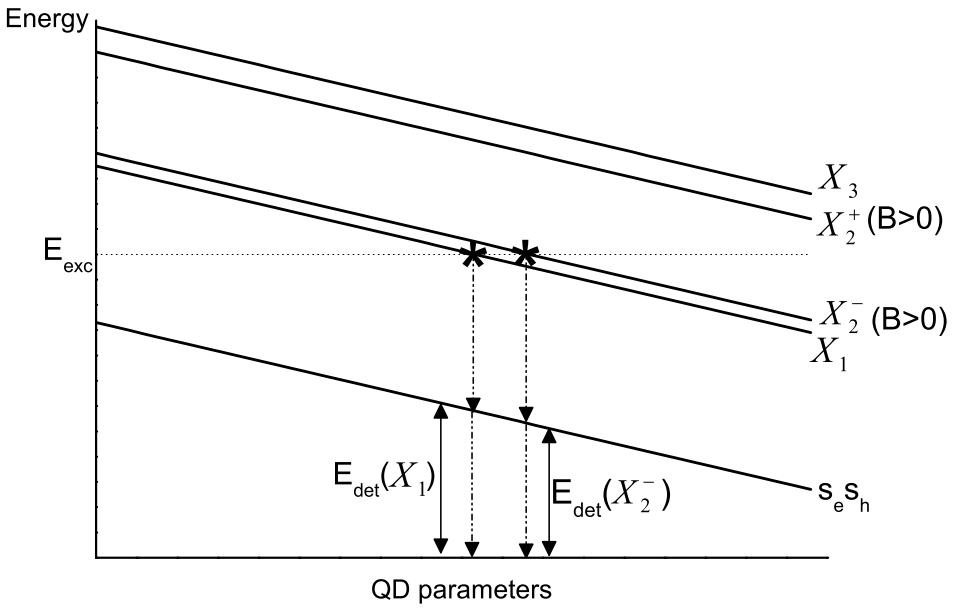

(b)

Figure 5.6: Schematic of the exciton energy levels displayed as a function of dot parameters. The dashed arrows represent the relaxation process during a RPL measurement with $E_{exc} = 1260$ meV at $B = 0$ T (a) and when a magnetic field is applied (b).

Finally, in Figures 5.7(a) and 5.7(b), we display several selected magneto-RPL spectra for our undoped sample and n-doped sample respectively. The spectra of the undoped sample were taken at the high excitation energy, $E_{exc} = 1281$ meV [Fig. 5.7(a)]. The results are therefore similar to those obtained in Fig. 5.3. We are able to observed the low energy peak (X_1) and the peak that splits into two separate peaks with the applied magnetic field (X_2). The high energy peak (X_3) is not detected at this excitation energy for this sample.

The selected RPL spectra of the n-doped sample was taken at a lower excitation energy, $E_{exc} = 1259$ meV [Fig. 5.7(b)]. These results are therefore comparable to those of Fig. 5.4 where only two peaks are observed: the low energy peak (X_1) and the lower branch (X_2^-) of the peak that splits into two with the magnetic field.

We observe the same excitation energy dependent behavior in the spectra of all of our differently doped samples.

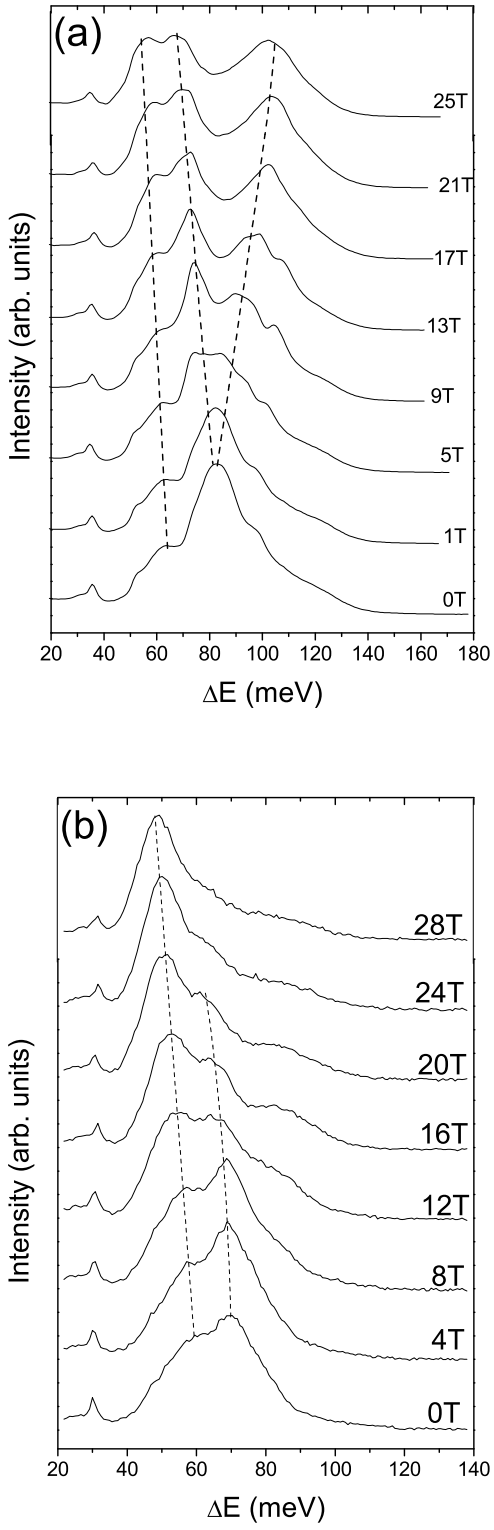

Figure 5.7: Magneto-RPL spectra recorded on sample U1 at 4 K from $B = 0$ to 25 T for $E_{exc} = 1281$ meV (a). Magneto-RPL spectra recorded on sample N2 at 4 K from $B = 0$ to 28 T for $E_{exc} = 1259$ meV (b). Traces have been vertically offset for clarity. The dashed lines are guides for the eyes.

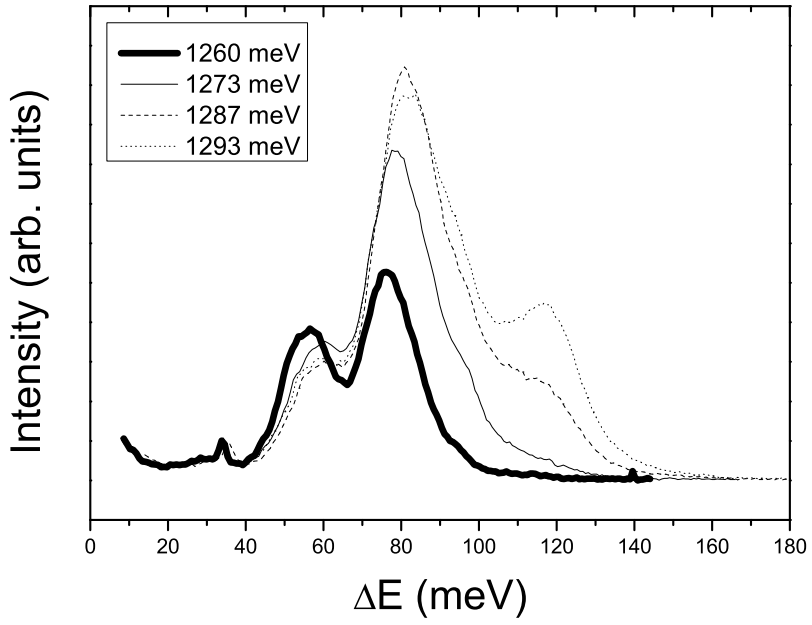

Figure 5.8: RPL spectra of sample P3 taken at 4 K for E_{exc} = 1260, 1273, 1287 and 1293 meV at 0T.

5.2.2 Study as a Function of Excitation Energy

To further support the above analysis, we present, in Fig. 5.8, the RPL spectra at 0 T for four different excitation energies: E_{exc} = 1293, 1287, 1273 and 1260 meV. The spectra for E_{exc} = 1293 meV and E_{exc} = 1260 meV, are the same 0 T results studied in the previous section. All four spectra were collected in identical experimental conditions, i.e. laser intensity and temperature. The peak observed for E_{exc} = 1293 meV at $\sim$ 116 meV decreases in intensity as the excitation energy is decreased. The peak is no longer detected for an excitation energy, E_{exc} = 1260 meV. After an initial slight increase in intensity between the 1293 meV spectrum and 1287 meV spectrum, the same tendency is observed for the peak at an energy of $\sim$ 80 meV. However, this peak does not completely disappear at the lowest excitation energy, E_{exc} = 1260 meV. In addition, we observe that the peak at $\sim$ 59 meV increases in intensity as the excitation energy is decreased. This behavior can be explained by the fact that as the excitation energy is decreased, the population of dots whose X_3 energy level (116 meV peak) coincide with E_{exc} decreases. We therefore observe the diminution of the high energy peak in Fig. 5.8. Conversely, the population of dots whose X_1 level (59 meV peak) coincide with E_{exc} increases with an increasing E_{exc}. This corresponds to the observed increase in intensity of the low energy peak. Finally, the situation of the $\sim$ 80 meV peak is a little more complicated. For this peak changing from an excitation energy of E_{exc} = 1293 meV to E_{exc} = 1287 meV corresponds to changing from a detection energy of E_{det} = 1213 meV to E_{det} = 1207 meV. Both these energies being close to 1200 meV, we do not initially observe a great change in the intensity of the $\sim$ 80 meV peak. For the two remaining lower excitation energies, the corresponding detection energies are found farther from the NRPL peak energy of 1200 meV, and a decrease in intensity is therefore observed.

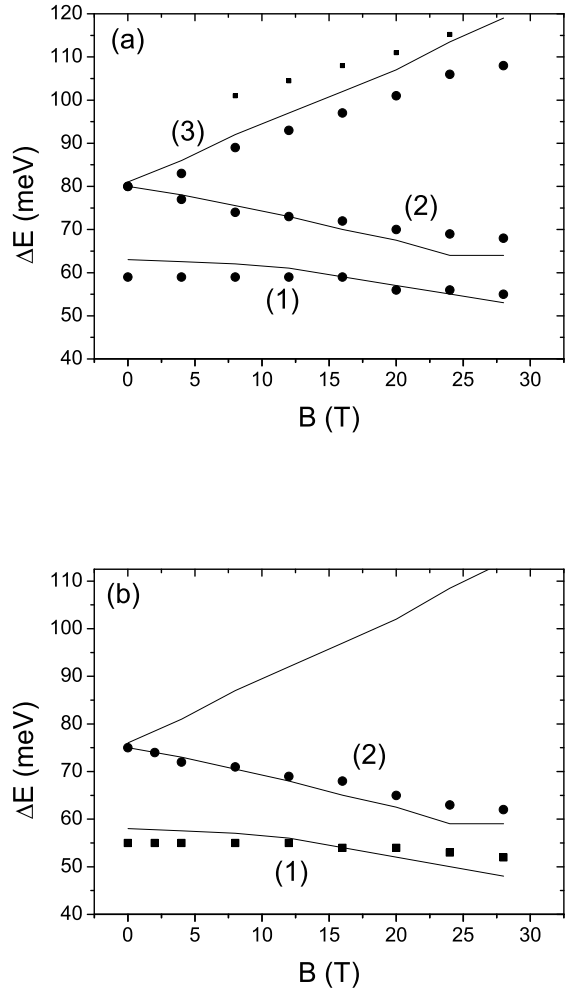

Figure 5.9: Magnetic field dispersion of RPL resonances for E_{exc} = 1293 meV (a) and E_{exc} = 1260 meV (b) of sample P3 in symbols. The solid lines are the polaron energy levels, calculated in Chapter 4, shifted to fit the RPL experimental results, as explained in the text.

5.3 Comparison with Polaron Model

5.3.1 Magnetic Field Dispersion Comparison

In Fig. 5.9(a), we compare the magnetic field dispersion of the RPL resonances of sample P3 in symbols, for an excitation energy E_{exc} = 1293 meV , with the calculated polaron states in solid lines. Figure 5.9(b) displays the equivalent graph for a RPL experiment measured at an excitation energy E_{exc} = 1260 meV. The energy positions as a function of magnetic field of the calculated levels are found to be in good agreement with our data.

As stated earlier, a RPL experiment essentially measures the same quantities as those measured in an PLE measurement. In addition, the same sample, P3, was used for both the RPL and PLE studies. The calculation and fitting parameters used for the PLE comparison, were therefore also used for the RPL fit. As before, an in-plane effective mass of the electron, $m_e = 0.07m_o$, and the hole, $m_h = 0.22m_o$, were imposed. A cone with a radius $R = 115$ Å, and height $h = 28$ Å, and conduction (valence) band offset of 290 meV (212meV) were chosen to best fit the data. The rest of the parameters can be found in Chapter 4, Figure 4.12.

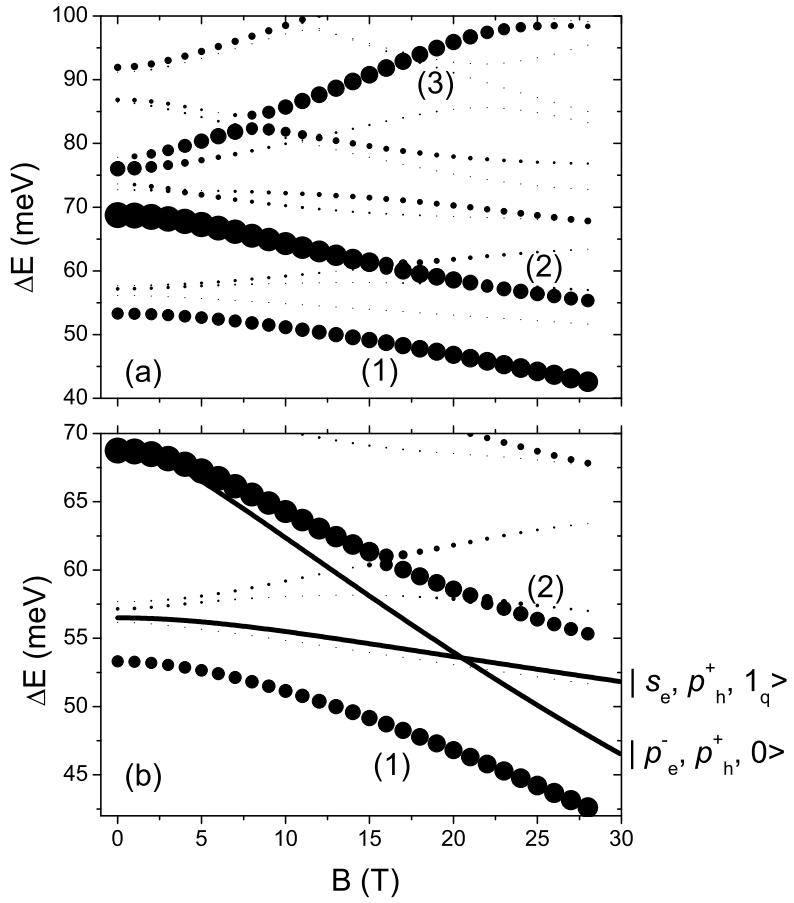

Figure 5.10: Calculated excitonic polaron energies and intensities as a function of the magnetic field. The area of the circles is proportional to the oscillator strength of the transitions. The parameters for this calculation are given in Section 4.3 of Chapter 4.

In Fig. 5.10, the three low-lying calculated polaron states are presented. We are reminded that the experimentally observed anti-crossing is primarily the result of the Fröhlich interaction between the two exciton-phonon states: $|p_e^-, p_h^+, 0\rangle$ and $|s_e, p_h^+, 1_{\alpha(s_e p_e^-)}\rangle$. The two polaron states, (1) and (2), are experimentally observed for both excitation energies. The third polaron level, (3), is only observed in Fig. 5.9(a). As discussed in the previous section, there are very few dots in our sample whose polaron (3) energy level (labeled X_2^+ in the last section) coincide with the excitation energy, E_{exc} = 1260 meV. Therefore, only two polaron states are detected in Fig. 5.9(b).

Finally, we note that we have performed a rigid upshift on the calculated polaron levels in order to fit the experimental results. The calculation was shifted up by 10 meV in Fig. 5.9(a)($E_{exc} = 1293$ meV) and by 5 meV in Fig. 5.9(b) ($E_{exc} = 1260$ meV). This shift was necessary because, as mentioned above, the dot dimensions used in the PLE fit were equally employed for the fits of Fig. 5.9. By using the same parameters, we assume that the same sized dots were selected for both experimental methods, which is not necessarily the case as we will demonstrate with the help of Fig. 5.11.

The x-axis of Fig. 5.11 corresponds to the detection energy of our experiments, which is equivalent to the interband ground state energy, $E(s_e s_h)$. The y-axis corresponds to the sum of the electron and hole intraband energy differences at 0 T,

$$E_p^e - E_s^e + E_p^h - E_s^h = \Delta E \tag{5.2}$$

which in turn roughly corresponds to the p-like energy peak of both RPL and PLE experimental results at 0 T (labeled X_2^0 in the previous section). The dashed and solid lines were extracted from the calculation presented in Chapter 1, Section 1.4.2. In dashed lines, we find the variation of the interband ground state energy and ΔE for a changing island height and fixed radius, R = 115 Å. In solid lines, we have the same evolution, but this time for a changing radius and fixed height, h = 28 Å. The open symbols are data taken from RPL experiments and the solid symbols from PLE measurements. The solid symbol that is found at the intersection between the two lines corresponds to the PLE measurement taken for a detection energy, E_{det} = 1215 meV. As this was the original measurement used for the fit, the detection energy and ΔE of this experiment correspond to a dot with a radius, R = 115 Å and height h = 28 Å. The fit for the same PLE measurement with a detection energy of either E_{det} = 1206 or 1194 meV (the two remaining solid symbols) would require a dot with a slightly larger radius and a larger height.* We also notice that the 10 meV shift performed in Fig. 5.9(a), is the equivalent of using a dot with a smaller radius and larger height (open circle). The 5 meV shift performed in Fig. 5.9(b), corresponds to using a dot with a smaller radius and greater height (open triangle) than the one used in the original fit. By performing the necessary shifts, we are able to use the same dot parameters for measurements that select different sized dots.

*The variation of the composition of the dot x, ($In_{1-x}Ga_xAs$), that we did not include in Fig. 5.11, is an additional parameter that contributes to the shifts.

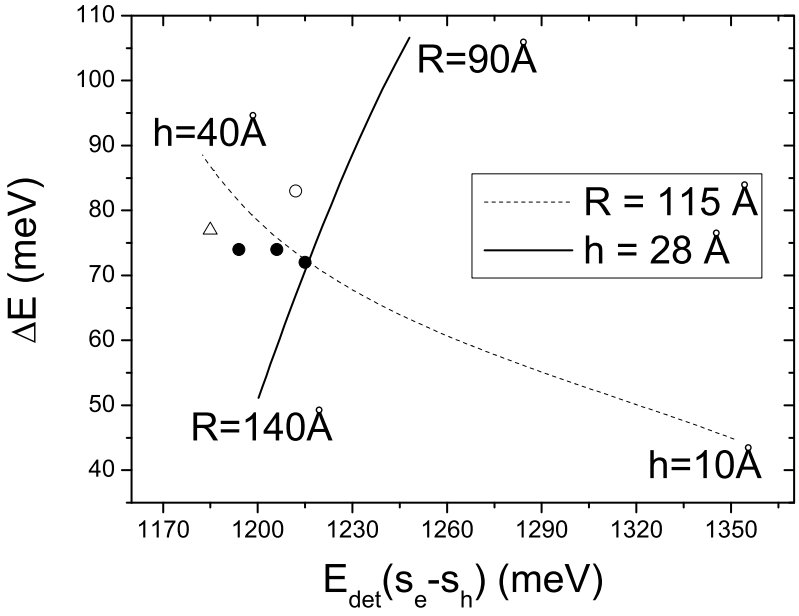

Figure 5.11: In dashed lines, the evolution of the detection energy and intraband energy transition for QDs of fixed radius $R = 115$ Å and varying height. In solid line, the same evolution for dots of fixed height $h = 28$ Å and varying radius. Symbols are the experimental results obtained from RPL and PLE experiments, as described in the text.

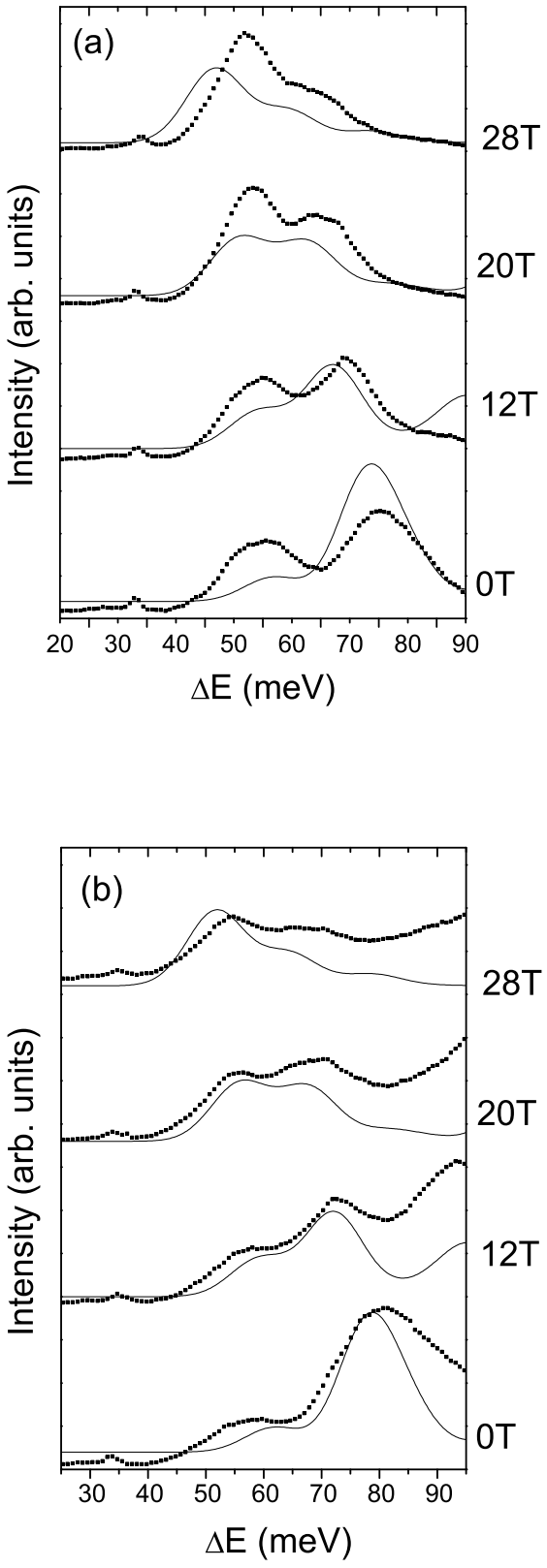

Figure 5.12: Experimental (full symbols) and calculated (solid lines) spectra for different magnetic fields. The experimental data was taken for E_{exc}=1260 meV (a) and E_{exc}=1293 meV (b), for sample P3. The parameters used in the calculation are given in the text.

5.3.2 Oscillator Strength

The exchange in oscillator strength between the two low-lying polaron states in clearly observed in the magneto-RPL spectra presented in Section 5.2.1. We shall now compare these spectra with the interband absorptions calculated in Section 4.3.2. In Fig. 5.12, we present the calculated absorptions in solid lines at different magnetic fields. The symbols are data points taken for sample P3 for $E_{exc} = 1260$ meV (a) and $E_{exc} = 1293$ meV (b). The calculated spectra have been shifted 5 meV (10 meV) to fit the data in Fig. 5.12(a) [Fig. 5.12(b)] (see previous discussion with respect to Fig. 5.11).

We remark slight differences in the experimental spectra of Fig. 5.12(a) as compared to the calculations. Firstly, at 0 T, we experimentally observe very similar intensities for the two peaks, whereas the calculated spectrum predicts a stronger OS for the high energy branch. In addition, at 20 T, where we predict equal OS's for both peaks, the experimental data displays a lower energy peak more intense than its high energy neighbor. The tendency for the high energy peak to be weaker than what is theoretically predicted can be explained using the reasoning presented in the previous section. Indeed, in Fig. 5.8, where the RPL spectra at different excitation energies at 0 T is presented, a diminution of the peak at ~ 80 meV is observed as the excitation energy is decreased. As explained in the previous section, this is due to the dot size inhomogeneity present in our samples. Our calculated spectra were found using one particular dot size and therefore do not take into account any size inhomogeneity. This could therefore be an explanation of the discrepancy observed between the experimental and theoretical results in Fig. 5.12(a).

On the other hand, the spectra of Fig. 5.12(b) was measured at an excitation energy, $E_{exc} = 1293$ meV. There exists a large population of dots with excited states equal to this excitation energy. The difference in intensity of the two observed peaks, can therefore be attributed fully to a polaron anti-crossing effect and not the dot population distribution. We find here, as we found in Chapter 4 for the PLE results, that the evolution of the peak intensities with the magnetic field is very well described by our model. We are able to predict the exchange of oscillator strength observed in both our RPL and PLE results, demonstrating the validity of our analysis. The unequivocal anti-crossing observed in the RPL spectra provide additional evidence of the existence of excitonic polaron states.

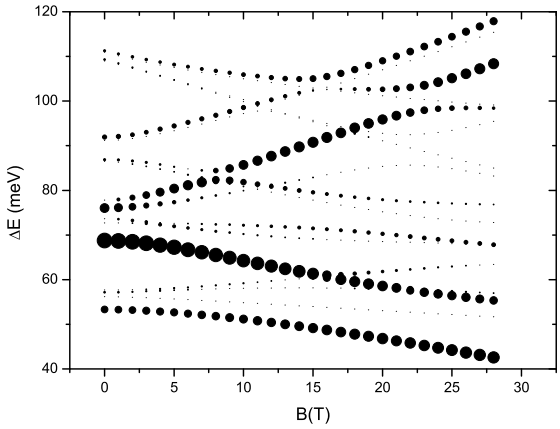

Figure 5.13: All calculated polaron energies and intensities as a function of magnetic field. No polaron level with significant OS is predicted in the vicinity of 110 meV.

5.3.3 High Energy Peak

Up until now, we have not attempted to explain the high energy peak at $\sim$ 110 meV, consistently observed in our experimental results. This high energy peak, that is detected in both PLE [Fig. 4.13(a)] and RPL [Fig. 5.3] experiments, stays at a nearly constant energy as the magnetic field is increased. As seen in Fig. 5.13, our excitonic polaron calculation does not predict such a peak with a strong oscillator strength in this energy range. The evolution of this peak in a magnetic field is reminiscent of the behavior of transitions that involve s-like states, whose energy moves very little (diamagnetic effect) with an applied B field.[†]

As noted in Chapter 1 and Appendix A, the QD energy level calculation used in this thesis does not include the light hole states. We assume, due to the strong strain in a self-assembled QD system, that these states are very close in energy to the GaAs valence band edge [4] and therefore will not be pertinent to the description of our experimental results.

[†]When calculated, the optically allowed transition $2s_e$-$2s_h$ is found to be $\sim$160 meV above the ground state excitonic level, and therefore too high to account for this peak [8].

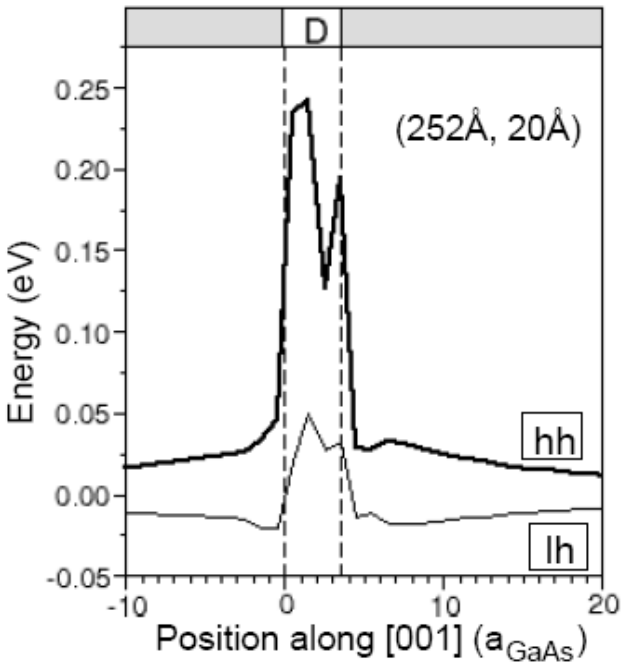

Figure 5.14: Strain-modified valence band offsets calculated along the z-direction [9]. Both heavy hole states and a light hole state are found. Figure taken from reference [9].

However, recent theoretical studies, in particular conducted by Gustavo Narvaez of the National Renewable Energy Laboratory in Colorado, have revealed the importance of the light hole states. Using an atomistic pseudopotential approach [7], the strain-modified valence band offset, shown in Fig. 5.14, of dots similar to those of our samples[‡] were calculated [9]. A confined light hole state is found below that of the heavy hole. In addition, the excitonic absorption spectra of the QDs were calculated where a significant peak approximatively 100 meV above the ground state energy, $E(s_e s_{hh})$, is predicted. The peak corresponds to an interband transition between the electronic state of s symmetry $|s_e\rangle$ and the light hole state of s symmetry $|s_{lh}\rangle$. This transition is a possible explanation for the high energy peak observed in our experimental results. In order to predict this peak with the effective mass method used in this thesis, the addition of the light hole band would be necessary.

[‡]lens-shaped $In_{0.6}Ga_{0.4}As$ dots with $R = 126$ Å and $h = 20$ Å.

5.4 Conclusion

In this chapter, the RPL spectra of a *p*-doped self-assembled InAs/GaAs QD sample have been investigated as a function of magnetic field and excitation energy .

The number of peaks as well as their intensities are observed to vary depending on the excitation energy used in the experiment. These differences were found to be a consequence of the dot size distribution, intrinsic to our self-assembled samples. By exploiting results obtained in NRPL, we were able to qualitatively explain the variation of peak intensity as a function of magnetic field and excitation energy.

We then compared the magneto-RPL results with the excitonic polaron energy levels and oscillator strengths originally calculated for the magneto-PLE measurements of Chapter 4. To account for the different sized dots probed during the two different PL techniques, an energy shift of the calculated polaron states was effectuated. With this shift, a good agreement was found between the calculations and the RPL experimental data, giving further evidence to the existence of excitonic polarons.

Bibliography

[1] C. Kammerer, G. Cassabois, C. Voisin, C. Delalande, Ph. Roussignol, and J. M. Gérard, *Photoluminescence Up-Conversion in Single Self-Assembled InAs/GaAs Quantum Dots*, Phys. Rev. Lett. **87**, 207401 (2001).

[2] R. Oulton, J.J. Finley, A.I. Tartakovskii, D.J. Mowbray, M.S. Skolnick, M. Hopkinson, A. Vasanelli, R. Ferreira, and G. Bastard, *Continuum transitions and phonon coupling in single self-assembled Stranski-Krastanow quantum dots*, Phys. Rev. B **68**, 235301 (2003).

[3] L.-W. Wang, J. Kim, and A. Zunger, *Electronic structures of [110]-faceted self-assembled pyramidal InAs/GaAs quantum dots*, Phys. Rev. B **59**, 5678 (1999).

[4] J.-Y. Marzin and G. Bastard, *Calculation of the Energy Levels in InAs/GaAs Quantum Dots*, Solid State Com. **92**, 437 (1994).

[5] O. Stier, M. Grundmann, and D. Bimberg, *Electronic and optical properties of strained quantum dots modeled by 8-band k·p theory*, Phys. Rev. B 59, 5688 (1999).

[6] J.N. Isaia, Ph.D. thesis, *Niveaux électronique et interaction électron-phonons dans les boîtes quantiques d'InAs/GaAs*, Université Paris VI (2002).

[7] A. J. Williamson, L. W. Wang, and A. Zunger, *Theoretical interpretation of the experimental electronic structure of lens-shaped self-assembled InAs/GaAs quantum dots*, Phys. Rev. B **62**, 12963 (2000).

[8] D.P. Nguyên, Ph.D. thesis, *Confinements non-usuels dans les boîtes quantiques semiconductrices*, Université Paris VI (2005).

[9] G.A. Narvaez and A. Zunger, *Enhancement of nominally-forbidden interband optical transitions in quantum dots*, Phys. Rev. **B** 74, 045316 (2006).

Conclusion

Semiconductor quantum dots have the potential to be the essential ingredient for quantum devices. In order to exploit the potential of quantum dot systems, a good understanding of their energy levels is needed. This thesis has explored the interaction of carriers and phonons in several differently doped quantum dot structures. This subject has attracted considerable attention recently, as the comprehension of such an interaction is essential for the understanding of the electronic properties of quantum dot systems, for instance, the carrier relaxation which is of particular interest.

In Chapter 2, it was shown that a charged carrier is in a strong coupling regime with the longitudinal optical phonons of the surrounding crystal lattice. A detailed calculation was given to show that this coupling results in the formation of polarons; a hybrid carrier phonon state, which are the true excitations of a charged dot. We then demonstrated, through far infrared magnetotransmission experiments performed on n-doped dots in polarization, the existence of such states. Indeed, the magnetic dispersions as well as the intensities of the absorption spectra obtained in our experimental results cannot be explained using a purely electronic model. The introduction of a Fröhlich coupling term into the calculations is necessary to reproduce the experimental observed anti-crossings. This study exposed the shortcomings of the simple "artificial atom" image, often used to describe a quantum dot system. One can no longer consider the transitions in quantum dots as being between purely electronic states. These transitions, instead, occur between hybrid electron phonon states, called polarons.

The existence of electronic polarons having been established, in Chapter 3, we set out to explore p-doped systems and the interaction between holes and longitudinal optical phonons. Depending on the far infrared polarization direction, two different hole transitions were excited, whose intensity and dispersion versus magnetic field showed strong deviation with respect to the predictions of a purely electronic picture. Once again using the Fröhlich Hamiltonian, the coupling between low lying confined hole states and the lattice modes were calculated and the energies and oscillator strengths of the intraband transitions were determined. We showed that our model fits the experimental data very well and thusly provides the first evidence of hole polaron states in InAs quantum dots and demonstrates that, analogous to electrons, the intraband magneto-optical transitions occur between hole polaron states.

In addition, in this chapter, the observation of an InAs-like phonon mode in the far infrared transmission spectra of our experimental results was exposed. As the confined hole states are found energetically close to this mode, it was this phonon mode, and not the GaAs mode, that was used in our calculations. However, the

GaAs phonon mode can no longer be neglected for experiments in intense magnetic field, where the hole state is pushed up in energy. In this case, the hole state is found in proximity to both the InAs and GaAs phonon modes and a two phonon model is necessary to predict our data. To better understand the nature of the two phonon modes in InAs/GaAs quantum dots, found in interaction with the hole state, additional experimental data needs to be obtained. It would be interesting, for example, to study annealed n-doped dots. The confined electron energy in such dots will be decreased, as a result of the annealing process, making the investigation of the interaction between electron states and the lower energy InAs-like phonon state possible. Such a study could, in particular, give valuable information concerning the composition of InAs and GaAs in the dots, as the composition is related to the Fröhlich coupling strength of the two respective phonon modes.

In Chapter 4, we moved on to the investigation of interband transitions of self-assembled quantum dots. Using photoluminescence excitation spectroscopy under strong magnetic fields up to 28 T, the energy levels of several ensembles of differently doped samples were probed. As only dots with ground state energy equal to the detection energy are detected, this technique allows one to circumvent part of the inhomogeneous broadening observed in the non-resonant photoluminescence spectra of self-assembled samples. Several well-defined resonances were observed in all samples. The magnetic field dependence of the resonance energies allowed for the unambiguous assignment of the interband transitions, which involve both discrete states of the quantum dots and wetting layer states. A strong anti-crossing between two transitions was observed in all samples, which cannot be accounted for in a purely electronic model. Similar to the case of electrons and holes confined in dots, the use of the Fröhlich Hamiltonian was necessary to explain our experimental results. We revealed that excitons, in spite of their electric neutrality, are found to be strongly coupled to the longitudinal optical phonons of the surrounding lattice. Excitonic polarons are predicted to give significant modifications of the energy levels and large anti-crossings when two exciton-phonon states have close enough energies with phonon occupations which differ by one. Such effects are experimentally observed in all of our samples, thusly evidencing the strong coupling that takes place between excitons and phonons as well as the fact that the interband transitions occur between excitonic polaron states. These excitonic polaron states present important consequences to the understanding of the behavior of an excited quantum dot. In particular, a reexamination of the energy relaxation paths of excited quantum dots and of the decoherence effects is needed.

Finally in Chapter 5, a complementary study of the interband transitions using resonant photoluminescence experiments in strong magnetic fields was presented. The study of these spectra, as a function of varying excitation energy, highlighted the consequences of the dot size dispersion, present in our samples. The variation of peak energy and intensity between spectra of different excitation energy was qualitatively explained in terms this size dispersion.

In addition, the resonant magneto-photoluminescence spectra were compared with the excitonic polaron calculations of Chapter 4. Once again, a very good agreement was found between theoretical and experimental results, when comparing both the magnetic dispersion curves and the absorption spectra. This comparison provides

further proof of the existence of excitonic polarons in quantum dots.

A discussion of the existence of a light hole state in quantum dots was also presented in this chapter. The consistent observation of a high energy peak in all our photoluminescence results calls for the reexamination of the supposition that quantum dots do not contain light hole states. A calculation including these states is most probably necessary for the explanation of the peak observed at ~ 110 meV, that stays constant with an increasing magnetic field.

In conclusion, the effects of the interaction between carriers confined in quantum dots and the longitudinal optical phonons were exposed. Far infrared and photoluminescence investigations of quantum dot systems containing electrons, holes and excitons all lead to the same conclusion; the existence of polaron states in quantum dot systems and the fact that transitions occur between these states and not purely electronic states.

Appendix A

Atomic Wavefunctions

In the parabolic effective mass approximation, the wavefunction of a carrier (electron or hole) in a quantum dot can be separated into (i) a Bloch part which oscillates with the periodicity of the crystal lattice and (ii) a slowly varying envelope function:

$$\phi(\vec{\mathbf{r}}) = u_{n\vec{\mathbf{k}}=0}(\vec{\mathbf{r}})\psi_l(\vec{\mathbf{r}}) \tag{A.1}$$

where n refers to the band under consideration. The envelope functions, $\psi_l(\vec{\mathbf{r}})$, are calculated in Chapter 1. The Bloch functions are comparable to those found in bulk GaAs and InAs. The band structure of a III-V crystal in the vicinity of the Brillouin zone center is schematically presented in Fig. A.1. The atomic states of the conduction band possess an orbital angular momentum $l = 0$ (s-like) and spin, $S = \frac{1}{2}$. The degeneracy of the conduction band states is therefore two-fold, with a total angular momentum $J = l + S = \frac{1}{2}$.

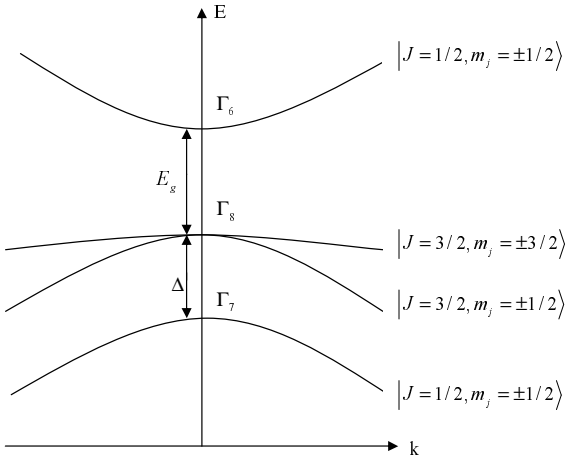

Figure A.1: Band structure of bulk InAs and GaAs near the BZ center, including the conduction band Γ_6 and valence bands Γ_7 and Γ_8.

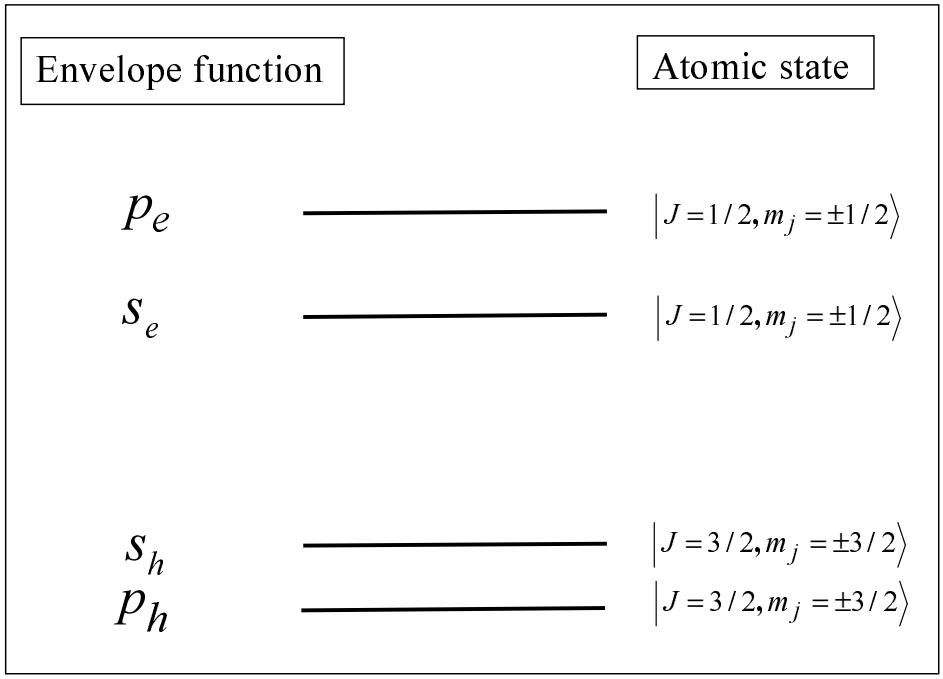

Figure A.2: Schematic of QD energy levels. Each level has a corresponding envelope function and atomic part.

The valence band states possess a p-like symmetry ($l = 1$). Adding the spin part, we find that the total angular momentum of the valence band states is either $J = \frac{3}{2}$ or $J = \frac{1}{2}$. Due to a spin-orbit coupling term, the $J = \frac{1}{2}$ states are energetically split from the $J = \frac{3}{2}$ states (energy separation noted Δ in Fig. A.1).

The quadruplet $J = \frac{3}{2}$ states are degenerate at the zone center. In a system under strong strain, this four-fold degeneracy is lifted [2]. In the case of a quantum dot system, the energy of the light holes ($m_J = \pm\frac{1}{2}$) is pushed down towards the GaAs valence band [3, 4, 5]. The light holes along with the $J = \frac{1}{2}$ states are therefore not included in our calculations. We are left with the two-fold degenerate heavy hole states, $|J = \frac{3}{2}, m_J = \pm\frac{3}{2}\rangle$ and the two-fold degenerate electron states, $|J = \frac{1}{2}, m_J = \pm\frac{1}{2}\rangle$.

A carrier confined in a QD can be associated with one of the above atomic states plus an envelope function, as represented in Fig. A.2. The aim of this Appendix is to show that the analysis of the experimental results of this thesis requires solely the consideration of the envelope part of Eq. A.1.

In the PLE and RPL results of Chapters 4 and 5, we find peaks with a FWHM $\sim$ 15 meV, for magnetic fields of up to 28 T. The Zeeman splitting of the atomic states in the presence of a magnetic field is written [3]

$$E = \pm\frac{1}{2} g\mu_B B = \pm E_z \tag{A.2}$$

where μ_B is the Bohr magneton. Experimentally obtained values of the g-factor for InAs QDs range from 2.6 [6] to 2.9 [3]. Ignoring the diamagnetic term, the interaction

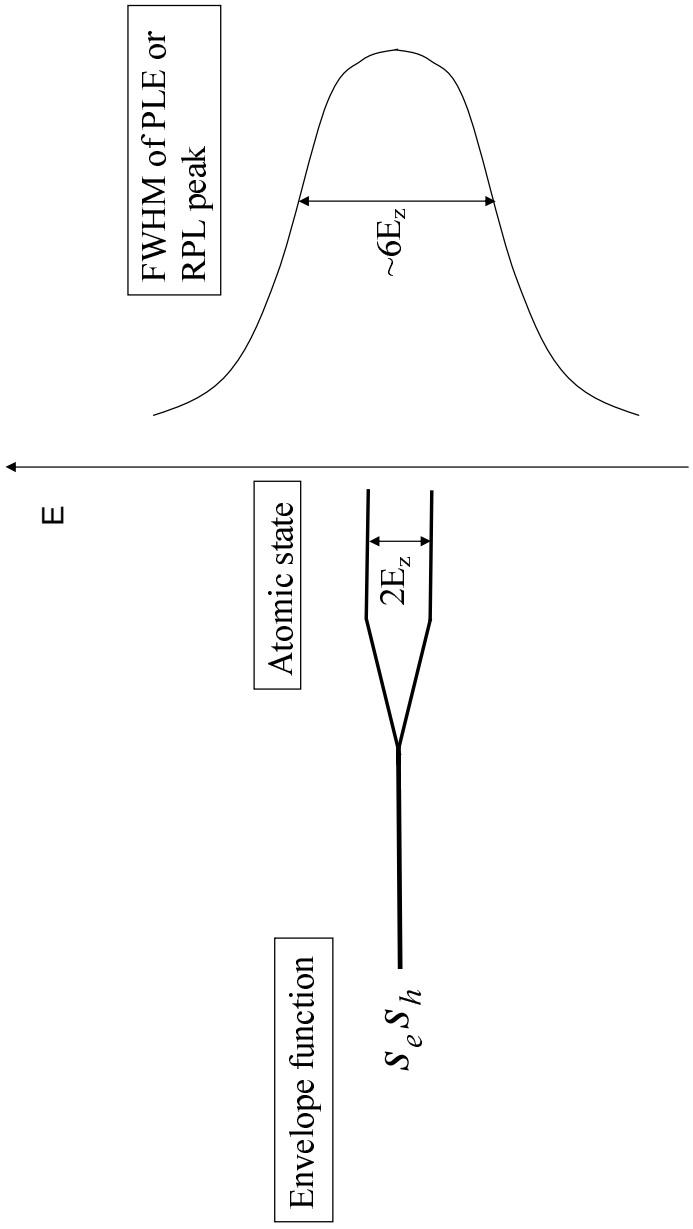

Figure A.3: Schematic comparison between the magnetic field induced spin splitting energy, assuming a magnetic field of 28 T, and the FWHM of a PL peak.

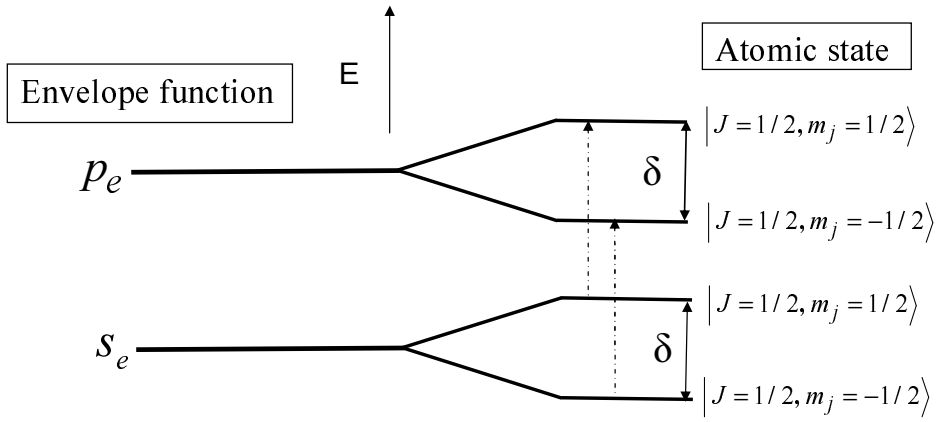

Figure A.4: Possible intraband transitions in dashed lines. The magnetic field induced spin splitting does not change the intraband energy transition $E_p - E_s$.

between the magnetic field and the spin of an electron-hole pair in a QD will therefore produce a splitting of approximatively 5 meV for a magnetic field of 28 T. Given the broadness of our PL peaks ($\sim$ 15 meV), such a splitting cannot be detected, as schematically shown in Fig. A.3. Thus, we find that PL measurements conducted on self-assembled samples, do not have the precision necessary to study the spin effects of a QD system.

The FIR magnetotransmission results of Chapter 2 and 3 permit the investigation of the intraband transitions of the QD system. As seen in Section 1.5.3 of Chapter 1, the polarization selection rules for such transitions involve solely the envelope function. The initial and final atomic states in intraband transitions are identical. As such, the spin splitting does not affect the intraband energies, as shown in Fig. A.4 where two possible intraband transitions are represented in dashed lines. Moreover, in thermal equilibrium (most probably the situation in weak absorption experiments at low temperature), only the lowest energy level is populated.

In conclusion, we find that for both our intraband and interband investigations the atomic part of the wavefunction does not come into play. The envelope function is the important element to consider in the analysis of our experimental results. This thesis therefore only contains discussions that include the envelope function.

Bibliography

[1] G. Bastard, *Wave mechanics applied to semiconductor heterostructures*, Les Editions de Physique (1996).

[2] O. Brandt, H. Lage, and K. Ploog, *Heavy- and light-hole character of optical transitions in InAs/GaAs single-monolayer quantum wells*, Phys. Rev. **B** 45, 4217 (1992).

[3] I. Favero, Ph.D. thesis, *Décoherence, symétries et relaxation de spin dans les boîtes quantiques de semiconducteurs*, Université Paris VI (2005).

[4] A. Vasanelli, Ph.D. thesis, *Transitions optiques interbandes et intrabandes dans les boîtes quantiques simples et couplées verticalement*, Université Paris VI (2002).

[5] J.-Y. Marzin and G. Bastard, *Calculation of the energy levels in InAs/GaAs Quantum Dots*, Solid State Commun. **92** 437, (1994).

[6] C. Schulhauser, D. Haft, R. J. Warburton, K. Karrai, A. O. Govorov, A. V. Kalameitsev, A. Chaplik, W. Schoenfeld, J. M. Garcia, and P. M. Petroff, *Magneto-optical properties of charged excitons in quantum dots*, Phys. Rev. **B** 66, 193303 (2002).

Appendix B

Fröhlich Constant

The definition of the Fröhlich constant in a bulk material is

$$\alpha_F = \frac{e^2}{\hbar}\sqrt{\frac{m^*}{2\hbar\omega_{LO}}}\left(\frac{1}{\kappa_\infty} - \frac{1}{\kappa_o}\right) \tag{B.1}$$

where $\hbar\omega_{LO}$ is the LO phonon energy of the crystal and m^* is the effective electron mass. The value of this dimensionless constant is related to the macroscopic polarization field induced by the ion displacements in a unit cell. As the value of this constant is well known for certain materials, it is commonly used in literature to describe the coupling strength between carriers and LO phonons. However, it is important to discuss exactly how the Fröhlich constant is related to this coupling strength, as misconceptions can easily follow from this conventional association.

The Fröhlich Hamiltonian used in our calculation is proportional to the constant A_F. In turn, A_F has the following relationship with the Fröhlich constant,

$$\alpha_F = \frac{\sqrt{2m^*}}{4\pi\hbar(\hbar\omega_{LO})^{3/2}}A_F^2 \tag{B.2}$$

We therefore find that the Fröhlich constant is related to the Fröhlich Hamiltonian by

$$\mathbf{V}_F \propto \frac{(\hbar\omega_{LO})^{3/4}}{2(m^*)^{1/4}}\sqrt{\alpha_F} \tag{B.3}$$

We first note that the effective electron mass, present in the definition of α_F, will cancel out of Eq. B.3. In other words, the Fröhlich constant depends on the mass of the carrier whereas the Fröhlich Hamiltonian does not. This is expected, as the Fröhlich Hamiltonian, which describes the interaction between dipole moments and a charged carrier, should not depend on the mass of the carrier.

Secondly, we remark that $\mathbf{V}_F$ is proportional to the square root of α_F. Therefore, a change in α_F is not directly proportional to a change in coupling strength. For example, three different values of α_F are used in this work: $\alpha_F = 0.075$ for electrons interacting with a GaAs phonon, $\alpha_F = 0.070$ for holes interacting with a InAs phonon, $\alpha_F = 0.105$ for excitons interacting with a GaAs phonon. This variation represents only an approximately 15% change in the constant A_F.

Indeed, the constant A_F, which is directly proportional to the Fröhlich Hamlitonian, and does not depend on the mass of the carrier, is a more appropriate measure of the carrier LO phonon coupling strength. We include the values of both A_F and α_F, for convention's sake, when discussing the fitting parameters of the calculations in this thesis.